Micromachined capacitive pressure sensor with signal conditioning electronics

Fragiacomo, Giulio

Publication date:
2012

Document Version
Publisher's PDF, also known as Version of record

PhD Dissertation

Micromachined capacitive pressure sensor with signal conditioning electronics

Giulio Fragiacomo

Department of Micro- and Nanotechnology
Technical University of Denmark

November 2011

Micromachined capacitive pressure sensor with signal conditioning electronics

Giulio Fragiacomo

Published by:
Department of Micro- and Nanotechnology
Technical University of Denmark
Ørsteds Plads, Building 345 East
DK-2800 Kgs. Lyngby
Denmark

Typeset with LaTeX 2ε

Innovation distinguishes between a leader and a follower.
Steve Jobs

Abstract

Micromachined capacitive pressure sensors for harsh environment together with interfacing electronic circuits have been studied in this project. Micro-electromechanical systems (MEMS) have been proposed as substitutes for macro scale sensor's systems in many different fields and are the only possible solution in many cases where, for example, the dimensions of the sensing element is the limiting factor. Furthermore, MEMS can significantly reduce costs and power consumption being the best candidate for consumer electronics such as mobile phones and cameras, or for the automotive industry where a great deal of sensors are used. Pressure sensors are among the most successful MEMS and are used in a huge variety of applications. In this project an absolute capacitive pressure sensor has been developed with the aim to integrate it in pump control systems to improve the efficiency of the pump.

The developed MEMS consist of hermetically sealed vacuum cavities surrounded by two heavily doped silicon layers which constitute the plates of a capacitor. The top plate is also the sensing element being a thin diaphragm that deflects when pressure is applied, thus increasing the capacitance (i.e. the output signal) of the device. Fusion bonding of two wafers has been used in order to obtain the cavities, this is also the only non-standard cleanroom process involved in the fabrication of the transducers. The device developed can measure absolute pressures from 0 to 10 bar with sensitivity up to 80 pF/bar.

As a part of the project a suitable interfacing circuit has been developed. Different solutions have been studied in order to optimize size, costs, sensitivity and stability. A comparative analysis between them has been carried out and suggestion for the final product has been proposed.

Both the electronic conditioning circuits and the MEMS have been fully described with mathematical models and simulated with electrical networks software for the circuit part and finite element for the sensor part. A good matching between analytical models and simulations results has been achieved. Furthermore, the experimental results are in good agreement with the models proposed.

Finally a demonstrator has been fabricated under the constraints of a previously designed case in order to contain costs; modification or re-design of the packaging is in fact one of the major costs for the MEMS industry. This demonstrator has been characterized and presented at Grundfos Direct Sensors A/S and constitute the preliminary work for a new product which is intended target the low power or wireless pressure sensor for harsh environment market.

Resumé (in Danish)

Dette projekt vedrører kapacitive mikrotryksensorer til barske omgivelser og dertil relaterede elektroniske grænseflader. Mikroeletromekaniske systemer (MEMS) er ofte benyttede, frem for makroskopiske sensorsystmer, inden for flere forskellige felter og er i mange tilfælde den eneste løsningsmodel, f.eks. i de tilfælde hvor størrelsen af sensorelementet er en begrænsende faktor. Derudover kan brugen af MEMS reducere omkostninger og energiforbrug væsentligt, hvorfor MEMS ofte anvendes til forbrugerelektronik som f.eks. mobiltelefoner og kameraer eller i bilindustrien hvor der benyttes mange sensorer. Tryksensorer hører til blandt de mest succesrige MEMS komponenter og anvendes indenfor en lang række forskellige applikationer. I dette projekt er en absolut kapacitiv tryksensor til anvendelse i pumpekontrolsystemer blevet udviklet med det formål at forbedre effektiviteten af pumpen.

Den pågældende MEMS komponent består af en hermetisk lukket vakuum kavitet, omgivet af to højt doteret siliciumlag der udgør kapacitorpladerne. Det øvre siliciumlag i kapacitoren er udformet som en tynd membran der udbøjer ved trykpåvirkninger, hvorved kapacitansen (dvs. udgangssignalet) øges, og siliciumlaget fungerer dermed som sensorelement. For at skabe den nødvendige kavitet sammenføjes de to siliciumlag vha. fusionbindingsteknologi (engelsk: fusion bonding), som er den eneste ikke standardiserede rentrumproces benyttet i forbindelse med fabrikationen af sensorerne. Den fremstillede sensor kan måle absolutte tryk fra 0 til 10 bar med en følsomhed på op til 80 pF/bar.

Som en del af projektet er en passende elektronisk grænseflade til sensoren blevet udviklet. Forskellige løsninger er blevet undersøgt for at optimere størrelse, pris, følsomhed og stabilitet. En sammenlignende analyse af de forskellige løsningsmodeller er blevet udført, og et forslag til det endelige produkt er blevet fremlagt.

Både de elektroniske konditioneringskredsløb og MEMS komponenterne er beskrevet i detaljer vha. matematiske modeller, og simulerede med hhv. elektrisk netværk og finite element software. Der er opnået god overensstemmelse mellem de eksperimentelle resultater og de teoretiske modeller.

Endelig er en demonstrationsmodel blevet fabrikeret. Demonstrationsmodellen er kompatibel med tidligere designs for dermed at reducere omkostninger; modificering eller re-design af indpakning er nemlig en af de største omkostninger i MEMS industrien. Demonstrationsmodellen er blevet karakteriseret og præsenteret ved Grundfos Direct Sensors A/S og udgør det indledende arbejde til et nyt produkt rettet mod markedet for lavt effekt forbrug eller trådløse tryksensorer til barske omgivelser.

Preface

This PhD dissertation is submitted in partial fulfillment of the requirements for obtaining the PhD degree from the Technical University of Denmark (DTU). It describes the work carried out at the Department of Micro- and Nanotechnology (DTU Nanotech) of this university from December 2008 to November 2011. The project has been supervised by Professor Erik V. Thomsen and co-supervised by Associate Professor Claus Kjærgaard, Associate Professor Ole Hansen and Development Engineer Carsten Christensen. It has been financially supported from DTU and Grundfos A/S in a successful effort of involving a private company in the research carried out in the public institutions.

Furthermore, the project has promoted the collaboration between two DTU's departments, namely DTU Nanotech and DTU Electrical Engineering, the first involved in the development of the semiconductor sensor and the second in the interfacing circuit. This collaborative effort of many different expertises has been the key of the success obtained in realizing a full system where MEMS technology, analogue electronics and packaging are integrated together based on proper mathematical modeling and software simulation results.

A special thanks goes therefore to my supervisor Erik V. Thomsen who has been inspiring when dealing with the sensor modeling and fabrication but most of all a great project leader involving students, professors, engineers and cleanroom technicians in this project and promoting it in the numerous meetings with Grundfos A/S. Secondly I must thank my co-supervisors, Associate Professor Claus Kjærgaard, Associate Professor Ole Hansen and Development Engineer Carsten Christensen, to whom I owe the results obtained in such a multidisciplinary field which covers mathematics, physics and electronics.

Of course I must thank the bachelor students participating in this project, Tore Bjørnson, Peter G. Bing, Mette F. la Cour and Søren Fisher, who contributed in the actual design and fabrication of both the conditioning circuits and the MEMS. Grundfos A/S and Danchip have to be thanked for their industrial support to the project and in particular Henrik Gamel who helped in the development of the demonstrator printed circuit board and Majken Becker who helped in the many capacitive pressure sensor batches fabricated. The capacitive sensor design started in 2006 with the work of my colleague Thomas Pedersen who I must thank for the incommensurable amount of cleanroom knowledge he shared with me and for designing the first prototype of this MEMS which is has been only slightly modified. I would also like to thank my good friend and colleague Thor Ansbæk who contributed in the development of the mathematical model for the sensor and has been a great mate both during my master and my Ph.D. project. First during my master project and then during my Ph.D. I have been working in the MEMS applied sensor group which I must give a special acknowledgment for all the good hints and tips given and for helping me in integrating in the danish society being very patience with my almost incomprehensible danish.

I am also grateful to my friends Stefano Ambrosini, Marco Vanin, Evarist Palushani, Luigi

Sasso, Andrea Cardellino, Martin Laursen, Sara Favalli, Marco Zamarin, Karina El-Sayed, Giovanni Rizzi, Alberto Cagliani and Filippo Bosco for making this three years unforgettable. Lastly, and most importantly, I have to thank my family for the continuous support and for being the best example for both my private and professional life.

Kongens Lyngby, November 30th, 2011

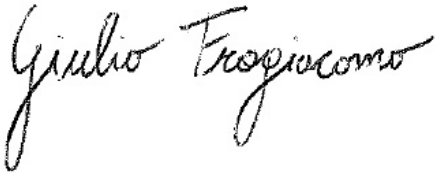

Giulio Fragiacomo

Contents

List of Figures

List of Tables

Chapter 1

Introduction

The focus of this project is to present a different solution to the actual piezoresistive pressure sensor commercialized by Grundfos A/S. The primary aim is to achieve an increase in sensitivity and a decrease in power consumption compared to the existing transducer in order to target a different market with also the future possibility to implement wireless sensing. Keeping the sensor surface planar therefore suitable for protective coating has also been one of the requirements.

In this chapter background and motivations for developing a micro-electromechanical system (MEMS) capacitive pressure sensor system are introduced. After a brief review on pressure measuring techniques the topic is shifted to micromachined devices and a comparison between different MEMS pressure sensors is depicted. The actual state of the art for MEMS pressure transducers is presented and the motivations for this project are stated. Then, the main results achieved, are summarized. Finally the outline of this dissertation conclude this chapter.

1.1 Pressure measurements methods

Pressure is a derived quantity defined from force and area, also derived quantities since based on mass, length and time, therefore pressure "standards" depend ultimately from the fundamental standards. None the less highly accurate instrument are available in the form of manometers and dead-weight piston gages for pressure values above 0.1 mmHg (roughly 0.133 mbar) and Bayard-Alpert ion gage for values below that limit [12]. Dead-weight gages and manometers are used to calibrate less accurate instruments which are in any case based either on comparison with known dead-weights on known areas or on the deflection of elastic elements subject to the unknown pressure. Fig. 1.1 shows a schematic of a calibration gage where a known load is connected through support, a piston, a cylinder and a system of pumps to the device under test. A number of corrections are made if a highly accurate measurement is required from this kind of standard since the gage pressure is evaluated from the following formula [12]:

$$P_g = \frac{Mg_1\left(1-\rho_{air}/\rho_{mass}\right)+\pi DT}{A_{(20,0)}\left[1+\left(\alpha_p+\alpha_c\right)\left(\theta-20\right)\right]\left(1+\lambda P\right)} - \left(\rho_{fluid}-\rho_{air}\right)g_1 h, \tag{1.1}$$

where, M is the total mass load, g_1 is the total acceleration of gravity, ρ is the density, D is the piston diameter, $A_{(20,0)}$ is piston effective area at 20 °C and 0 gage pressure, T is the gage fluid surface tension, α_p and α_c are the thermal expansion coefficients of piston and cylinder, θ is the temperature of the piston/cylinder, λ is the piston/cylinder elastic deformation coefficient

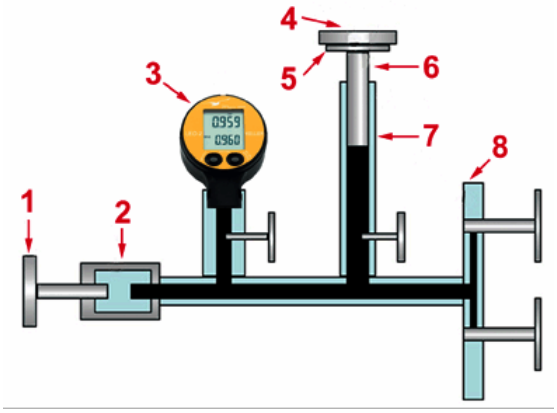

Figure 1.1: Schematic of a dead-weight standard: the hand pump (1) is used to regulate the pressure that the testing pump (2) applies to the pressure gage to be calibrated (3), the piston (6) and the filling connections (8). When the mass load given by the piston, the support (5) and calibration weight (4), is floating on the fluid there is balance and the pressure shown from the device under test should be equal to the ratio between mass load and the area of the fluid on which the load is applied. Figure acquired from [1].

and h is the height difference between piston gage reference level and the reference level of the unit under calibration.

The manometer instead (Fig. 1.2) is a self-balancing instrument which is described by a much simpler input/output relation:

$$h = \frac{p - p_0}{\rho_{fluid} g_1}, \tag{1.2}$$

where p is the unknown pressure and p_0 is the pressure at the instrument outlet (generally ambient pressure).

Another category of pressure sensors are based on a completely different pick-up method, namely the conversion of pressure into a mechanical deformation. These are called elastic transducers and group a huge variety of devices such as Bourdon tubes, diaphragms, bellows of different shapes and sizes. Among these we find also both piezoresitive and capacitive MEMS pressure sensors, which are based on the deflection of a thin membrane. Fig. 1.3 shows some example of deflection pressure transducers, in some cases the deflection of these devices is directly coupled to a pointer/scale readout, in other the motion is converted into an electrical signal employing piezo-electric, capacitive, optical or inductive readout methods. In the case of a circular diaphragm, the center point deflection is described by the following equation [13]:

$$w_0 = \frac{p a_0^4}{64 D} \tag{1.3}$$

where p is the pressure/load applied on the diaphragm, a_0 is its radius and D its flexural rigidity. A detailed analysis of circular plate deflection is presented in Chapter 2 where some special case such as contact mode between plate and substrate is also discussed. Vacuum pressure and ultra high pressure (over 700 MPa) are special cases where all the common methods mentioned above do not apply. Electrical devices based on Manganin or gold-chrome wire are used to measure both hydrostatic pressure or contact pressure between gears, cams and bearings up

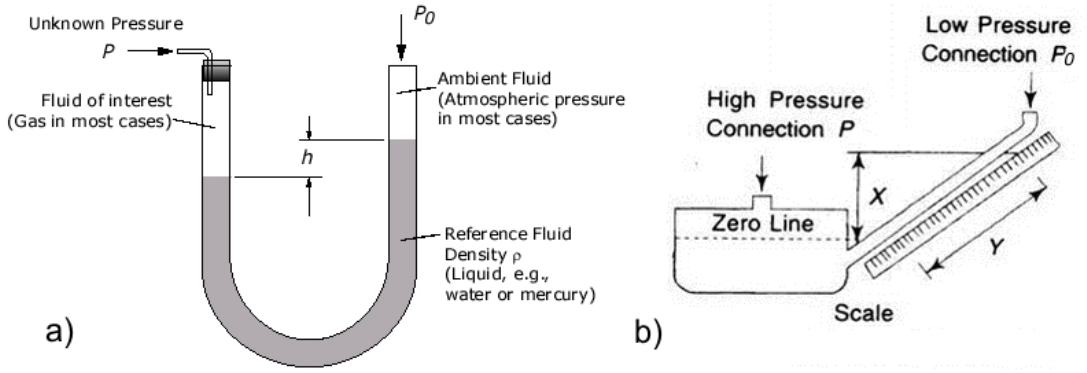

Figure 1.2: U-tube manometer (a) and Inclined manometer (b) operation principles: the fluid of interest at an unknown pressure, P, is forced into the transducer through a connector forcing the reference fluid, normally exposed to ambient pressure, P_0 at the output, to reach a hight, h (or x in case of the inclined manometer) which is proportional to the pressure applied. Figures acquired from [2, 3].

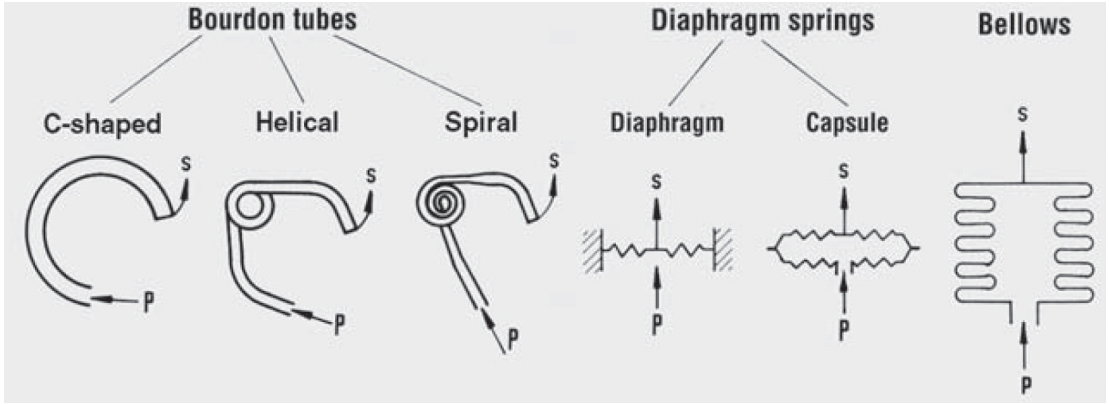

Figure 1.3: Different types of pressure transducers based on mechanical deformation. On the left C-shaped, helical and spiral Bourdon tubes are depicted. This devices are based on the fact that the force exerted by pressure (P) on the inside wall is greater than on the outside wall causing a deflection which is indicated with a pointer on a scale (S). Also in the case of diaphragm and bellows (on the right), pressure causes a deformation which is either directly coupled to a scale or converted to an electrical signal. [4].

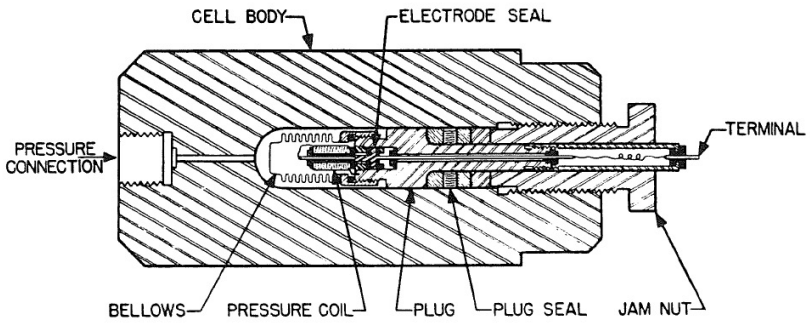

Figure 1.4: Manganin cell: the body has a pressure connector and a terminal at its ends which are the input and output of the cell respectively. The sensing element is constituted of a bellow which transfer the pressure from a possible conductive media to a non-conductive one [5].

to almost 1.4 GPa with a maximum inaccuracy of 0.5 %. A Manganin cell produced from Harwood Engineering is shown in Fig. 1.4; it measures the pressure as a function of the change in resistance in the Manganine coil when it is exposed to high pressure [5]. These kind of transducers have a coil resistance of around 120 ohm and a pressure sensitivity of 11.4 10^{-4} ohm/ohm/Pa which leads to a change of around 4 ohms over the entire pressure range. The change in resistance is measured by means of a common Wheatstone bridge.

While for ultra high pressure there are only few measurements methods, a variety of techniques are available for vacuum pressure measurements. This is also due to the fact that there are 6 different vacuum regimes ranging from low to extreme ultrahigh and only in one case, from the low to the high vacuum regimes (down to 10^{-3} Pa), where the reading does not depend on the media, the measurement can be done with the so called absolute pressure sensors. In this work an absolute capacitive pressure sensor has been developed and it is compared to other MEMS absolute pressure transducers in Section 1.2. For very- and ultrahigh vacuum measurements hot cathode ionization gages are used. Fig. 1.5a shows a Bayard-Alpert ion gage which have a reasonably linear response from 0.1 to 10^{-9} Pa, with maximum gage sensitivity of around 500 Pa. In this type of device a stream of electrons is emitted from the cathode (filament) and collected at the anode (grid), on their path they strike the gas molecules knocking out secondary electrons and generating positively charged ions which causes a ion current to flow in the collector. This current is a direct measure of the number of the gas molecules per unit volume and thus of the pressure. The sensitivity , S, of a Bayard-Alpert gage is given by:

$$S = \frac{i_i}{p i_e}, \tag{1.4}$$

where i_i is the ion current, i_e is the electron current and p is the gas pressure. At a pressure higher than 0.1 Pa too many scattering events will occur and the ions will not reach the collector. The lower limiting factor is the X-ray current generated by primary electrons when they hit the grid, this current is comparable to the ion current for pressure below 10^{-9} Pa. Extreme ultrahigh vacuum (i.e. below 10^{-9} Pa) can only be measured with partial-pressure analyzers, residual-gas analyzers or mass spectrometer. Among these, the most popular is the quadrupole mass filter (QMF), which can be thought as a ionization gage with a mass selective filter. A schematic of this instrument is presented in Fig. 1.5b where it is possible to see that it consists of a ion

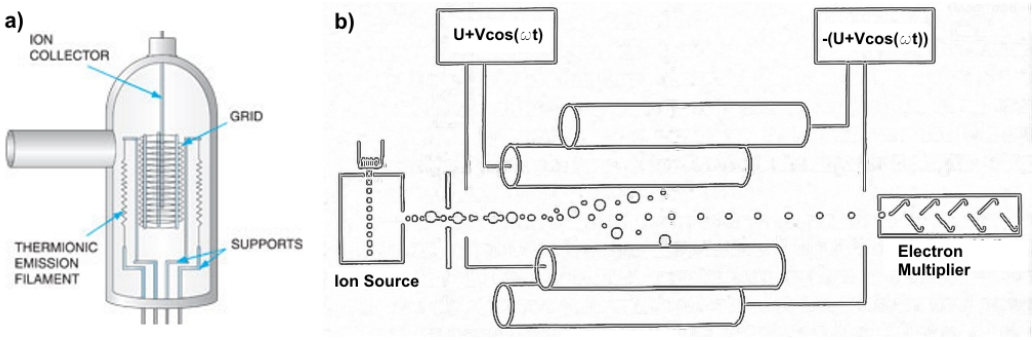

Figure 1.5: High to Extreme Ultrahigh pressure instruments: in Bayard-Alpert ion gage (a) a stream of electrons is emitted from a cathode (filament) and collected in the grid, on their path they strike the gas molecules originating ions which generate a current in the collector proportional to the pressure in the chamber. Quadrupole mass filters (b) are used for extreme ultrahigh vacuum, where only ions with a certain mass are allowed to travel from the source to the electron multiplier passing through the electromagnetic field generated by the four rods. [6].

source where the ions are generated, an aperture which is made of lenses that guide the ions into the quadrupole analyzer (four metal rods) and a detector. Applying the shown time varying voltages to the rods it is possible to achieve a band-pass filtering action since the alternating component of the electric field generated will cause the lighter ions to oscillate with increasing amplitude along the x-axis, while the constant component forces the heavy ions to diverge along the y-axis. Therefore, only ions with a certain mass will reach the detector.

In literature, high vacuum transducers are often considered separately from the other type of pressure sensors which are usually divided in four different groups:

- Absolute pressure sensor: it measures the pressure relative to perfect vacuum.
- Gauge or relative pressure sensor: it measure the pressure relative to atmospheric pressure (101.325 kPa).
- Differential pressure sensor: this sensor measures the difference between two or more pressures introduced as inputs to the sensing unit.
- Sealed pressure sensor: this sensor is the same as the gage pressure sensor except that it is previously calibrated by manufacturers to measure pressure relative to a fixed pressure value decided during fabrication.

Here all the most common type of macroscopic pressure sensors have been discussed, classified according to pressure range and measurement principle, Table 1.1 summarize what has been stated so far. In the next Section the choice of microfabricated sensors, for specific pressure range and applications, is motivated over other type of sensors and the MEMS capacitive pressure sensor is introduced.

Measurement devices	Pressure range	Maximum resolution	Error (% of full scale)
Mass Spectrometer	10^{-13} to 10^{-2} Pa	10^{-11} Pa (min partial pressure detectable)	N.A.
Bayard-Alpert ion gage	10^{-9} to 10^{-1} Pa	$2x10^{-8}$ Pa (X-Ray limit)	N.A.
Absolute pressure gage	10^{-6} to 10^{5} Pa	10^{-4} Pa (center point deflection =0.02 nm)	0.12
Inclined- Micromanometer	1 to $5x10^{4}$ Pa	0.25 Pa	0.003
Manometer U-Type	1 to $3x10^{6}$ Pa	1.3 Pa	0.1
Manometer Digital	1 to $7x10^{7}$ Pa	0.33 Pa	0.25
Dead-weight gages	1^{5} to $4x10^{6}$ Pa	2 Pa	0.015
Bourdon tube Helical	1^{5} to $7x10^{6}$ Pa	N.A.	0.1
Bourdon tube C-type	1^{5} to $7x10^{8}$ Pa	N.A.	0.1
Manganin cells	1^{5} to $1.4x10^{9}$ Pa	N.A.	0.75

Table 1.1: Macroscopic pressure measurement devices used from extreme ultrahigh vacuum to very high pressure. Maximum resolution and minimum error achievable are listed for comparison with the MEMS sensors described in Section 1.2.

1.2 Microfabricated pressure sensors

In the previous section macro-size pressure transducers covering a large number of sensing methods have been depicted with the aim of giving a general overview on pressure measurements and unifying, in a single table, suggestions for sensitive and reliable pressure techniques ranging from extreme ultrahigh vacuum to very high pressure. It is important to review these kind of devices because often MEMS pressure sensors are the micromachined version of their macroscopic counterparts. Furthermore, pressure sensors constitute one of the most successful MEMS developed and one of the most important device on the markets, especially if microphones are considered to be pressure sensors. This is shown in Fig. 1.6 where a research from Yole Development divides the MEMS market into the sum of contributions given from different devices and accelerometers, ink jet heads, pressure sensors, gyroscopes, RF MEMS and microfluidic devices are the main players.

Microsensors not only present the obvious advantage to target applications which could not be targeted from a bulky pressure transducer (e.g. the case of implantable sensors) but also have three other main benefits [14]:

- They allow for a high level of dimensional miniaturization, which is critical to the structural integration of sensors into the mechanical host environment.
- They provide multiplicity capability, which enables the fabrication of a large number of identical sensing units at the same time as one component, thus keeping the final cost of the product low (the low-cost aspect is critical to the industry's acceptance and technology transfer).
- They provide a natural interface to microelectronics, allowing for the union of localized signal conditioning with a microsized physical sensing element, all within a single MEMS sensing chip. This sensing chip is not only smaller in size than the traditional

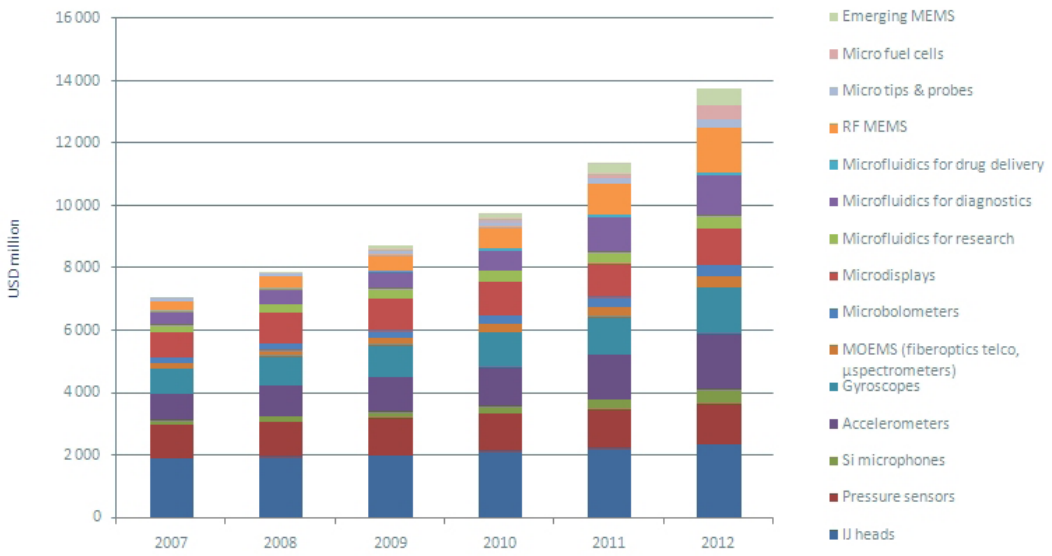

Figure 1.6: MEMS market 2007-2012: pressure sensors together with ink jet heads, accelerometers and gyroscopes are the most successful devices. Figures acquired from [7]

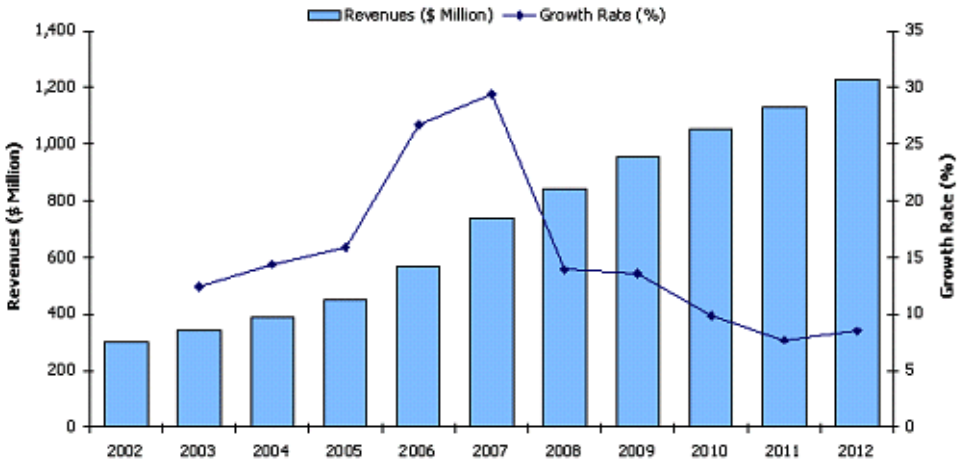

Figure 1.7: Automotive market for MEMS pressure sensors: in the last 8 years the market for this kind of devices has continuously grown with a peak of 30% growth in 2007. Figure acquired from [8]

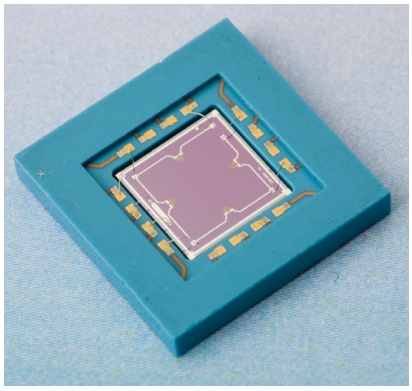

Figure 1.8: Example of a micromachined piezoresistive pressure sensor: the resistors are placed onto the membrane and as the last one deflects a change in resistance related to the pressure applied will be detected by an electronic circuit. Figure acquired from [9].

sensors but is also more robust in design. Many wire connections are eliminated and the interface is optimized among the various electromechanical subsystems.

According to [15], in order to be worth producing it, a new product has to be either 20% cheaper or perform 20% better for the same price. MEMS pressure sensors normally meet both requirements. This is proven in Fig. 1.7 where a growth ranging from 8 to 30% for the MEMS pressure sensors automotive market is depicted. This is a significant figure since the automotive is by far the leading market for this kind of device. Commercially available pressure sensors are almost exclusively piezoresistive or capacitive although other transduction methods such as such as resonating beams [16], servo-controlled [17], tunneling [18] and optical [19], [20] have been investigated. In this Section a brief overview of the piezoresistive, capacitive and optical micromachined pressure sensors is presented. Finally, since the capacitive pick-off method is particularly suitable for wireless sensing, which have been appointed as the main challenge for the future, a closer look to wireless MEMS pressure sensors is taken.

1.2.1 Piezoresistive pressure sensors

Commercially available micromachined pressure sensors are by a vast majority based on the piezoresistive effect, where a mechanical deformation causes a change in the electrical resistance of the sensing element which can easily be translated into a pressure signal. An example of a piezoresistive pressure sensor is shown in Fig. 1.8 where it is possible to notice the piezoresistors implanted in the membrane, this is fabricated by anisotropically etching a silicon wafer. This principle has been tested widely in the past 50 years and is often preferred to other approaches thanks to the fact that only standard cleanroom process such as ion implantation, oxidation and etching are involved. Compatibility to IC processes and therefore cheap process development are not the only reasons to prefer a piezoresistive sensor, also excellent linearity, simple conditioning circuits and high yield have been the key of the success of these kind of devices. Piezoresistive pressure sensors have undergone a enormous development through the years, from dimension of 5x5 mm they have shrink down to a the hundreds of micrometer size thanks to key processes such as anisotropic etching, ion implantation and anodic bonding. In 1985 Silicon direct bonding was reported [21] and was immediately implemented for

Fabricant and device	Die Size (mm)	Accuracy (%V_{FSS})	Sensitivity (mV/kPa)	T_r (ms)	P_{max} (MPa)	I_s (mA)	Price (USD)
Motorola MPXS4100A	2.7x2.8	1.8	54	1	1	7	30
Bosh BMP180	3.6x3.8	2.0	2.6	5	1	0.65	35
Freescale MPXV5100	5.0x3.0	2.5	45	1	1	7	50
Grundfos RPS 0-1	4.7x4.0	2	2	500	3	10	N.A.

Table 1.2: State-of-the-art piezorestive pressure sensors on the market. T_r indicate the time response of the device, P_{max} is the maximum overpressure applicable to the sensor and I_s is the current supplied during operation. All these devices have a pressure range of around 100kPa and, except for the last one, they have integrated signal conditioning electronics.

pressure sensor manufacturing both directly or by means of Silicon On Insulator (SOI) wafers. Nonetheless, strong temperature dependence of the piezoresistive coefficient π_{44}, limited pressure range and scalability (due to necessity of accommodating the piezoresistors on the membrane), necessity of a DC conditioning circuit, dependence to packaging induced stress and low sensitivity have ruled out this sensors in many cases. All these limiting factors are responsible for the "moderate" characteristics of the sensors commercially available. Table 1.2 highlights the main features of some state-of-the-art piezoresistive pressure sensors available, Grundfos coated pressure sensor is based on this principle but targets a special case, namely, harsh environment applications. The size of Grundfos die, which is particularly large compared to the one of the competitors, is justified from the particular packaging solution adopted. Grundfos sensor has a planar surface which is coated with a metallic corrosion-resistant layer that makes the sensor fully compatible with highly corrosive and wet media. Furthermore, this device is designed to be sealed with a double clamped O-ring from both side and this put a constraint on the dimensions of these transducers as explained in Chapters 3 and 4. In the next section the main alternative to the piezoresistive solution is discussed, namely, the capacitive pressure sensor (CPS).

1.2.2 Capacitive pressure sensors

Capacitive sensing has been historically a mechanical engineering field, mainly concerning positioning, pressure and sounds measurements [12]. In the beginning of the 70's Heerens [22] reviewed various techniques to mechanically design capacitive sensors; in the same years Jones and Richards [23] described an ultra sensitive capacitive micrometer and in 1982 Hugill [24] presented a capacitive displacement transducer. These sensors usually employed a transformer ratio bridge circuit in order to achieve the maximum possible sensitivity and an high degree of immunity to parasitic capacitance. Transformer ratio bridges, together with charge transfer circuit and more complicated methods such as switched capacitor circuits are still used to interface capacitive transducers [25–27]. While signal conditioning methods has always relayed on analog or mixed-signals electronics, the capacitive senor design, due to the needs of miniaturization, power consumption and costs issues, has shift from being realized by bulk mechanical parts to microfabricated silicon dies (see Fig. 1.9). An early example of this device

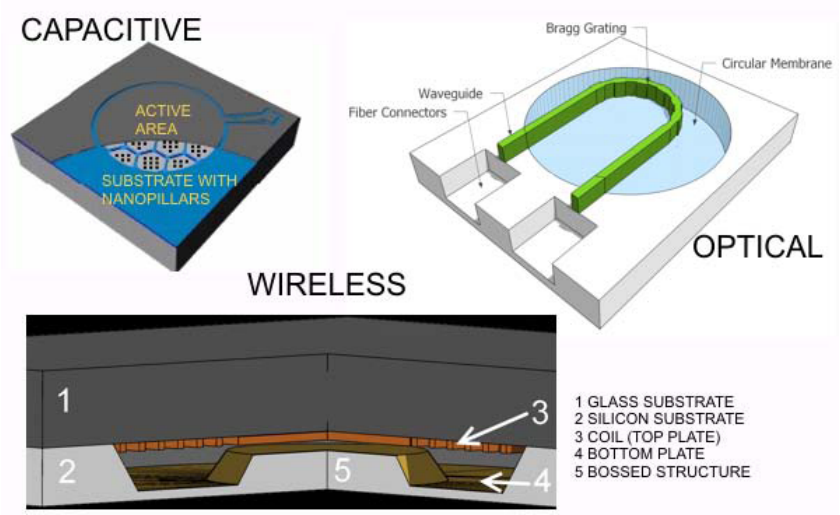

Figure 1.9: Artistic view of micromachined pressure sensors: capacitive, optical and wireless are the more promising technology appointed as alternatives to the more popular piezoresistive sensor.

Fabricant and device	**Die Size (mm)**	**Accuracy (%V_{FSS})**	**Sensitivity (mV/kPa)**	**Range (kPa)**	**P_{max} (MPa)**	**I_s (μA)**	**Price (USD)**
Motorola MPXY8000	2.6x2.6	3.0	1.2	250-450	1.4	1800	N.A.
VTI SCP1000	1.4x1.4	0.7	32.5	30-120	2.0	25	20
Vaisala Barocap	N.A.	0.03	40.0	50-110	0.5	N.A.	N.A.

Table 1.3: State-of-the-art capacitive pressure sensors on the market. P_{max} is the maximum overpressure applicable to the sensor and I_s is the current supplied during operation. Only the first of these device have integrated signal conditioning electronics.

was fabricated for medical purposes by Frobenius et al. [28] in 1973. In 1986 Ko [29] compares the capacitive pressure sensor with the well established piezoresistive device. In many respect capacitive sensing results more promising than its counterpart. In 1993, Puers [30], is of the same opinion as Ko and identifies pressure as the main field of application for capacitive measurements. In 1997, Baxter [31] wrote a book which threat thoroughly the wast subject of capacitive sensing but, with respect to silicon technology, he refers to the article written by Puers four years earlier. At the same time Eaton and Smith [15] reviewed the state of the art in micromachine pressure sensors technology, in their opinion capacitive micromachined pressure sensors were still under development. Only this century saw the first commercialized devices as pointed out by Gao and Zhang [14] in 2004. Some example are the tire pressure monitoring sensor (TPMS), shown in Fig. 1.10 and developed by Motorola, VTI absolute pressure sensor for implantable medical devises and Vaisala barometric sensor. Table 1.3 present the state-of-the-art of CPS commercially available, in Chapter 5 the prototype fabricated is compared with these.

Figure 1.10: Motorola MPXY8000 capacitive pressure sensor. The tire pressure monitoring sensor is an example of a commercialized MEMS capacitive pressure transducer. Figure acquired from [10].

1.2.3 Optical pressure sensors

Optical pressure sensors can in general be divided by detection method (amplitude or frequency modulated) and technology (electro-optical or all-optical design). The detection method defines characteristics such as sensitivity, with the amplitude modulated method being far superior, and multiplexing capabilities, for which frequency modulation is better suited. The choice of technology is a trade-off between the high flexibility and sensing capabilities of electronics and the immunity to electromagnetic interference, and also a trade-off elimination of parasitic capacitance and extremely low transmission loss of all-optical sensors. Several designs for optical pressure sensors have been suggested in literature, though with no or only very limited commercialization. While some of these sensors are made using III-IV technology [32], the flexibility of silicon technology makes this a more obvious choice. An example of an electro-optical amplitude modulated pressure sensor has been given by Hall et al. [33] which combines a vertical-cavity surface-emitting laser (VCSEL), a membrane with integrated diffraction grating and photodetectors into a microphone capable of detecting down to 24dB(A). Even though electro-optical designs show very good performance, they do not posses the qualities unique to all-optical sensors, and are thus in direct competition with electrical sensors. In the domain of all-optical pressure sensors, the most prominent designs are the Fabry-Perot cavity [34] and the Mach-Zender interferometer [35, 36] pressure sensors. In Fabry-Perot pressure sensors the deformation of a membrane causes a change in the width of a Fabry-Perot cavity which again changes the wavelength. Depending on membrane size this can be a relatively sensitive design which lends itself very well to distributed sensing. The Mach-Zender design utilizes the phase shift between waveguide crossing a deflected membrane and a reference waveguide to measure pressure. As this is an amplitude modulation method, the sensitivity can be even higher than for the Fabry-Perot, but at the cost of distributed sensing capabilities. A common advantage to these two designs is that both are passive components i.e. there are no power requirements for the sensor itself. A closely related alternative to the Fabry-Perot sensor is the Bragg grating sensor, which creates a change in wavelength due to deformation of a waveguide with integrated Bragg

grating. The Bragg grating sensor is also all-optical and frequency modulated and therefore has all the same inherent characteristics as the Fabry-Perot sensor. Contrary to the Fabry-Perot sensor, the Bragg grating sensor does not have multiple material interfaces in the light path, which reduces loss due to Fresnel reflection and it can be structured more flexible, allowing for mechanical force amplification. The concept of Bragg grating sensors is also known from fiber Bragg grating sensors (FBGs), where fibers with UV-written gratings acts as sensing elements. Fiber Bragg grating pressure sensors with detection limits of 0.36kPa has been achieved [37], however, using MEMS technology, much better control of material and structural properties than what can be achieved in fiber technology would allow for much higher sensitivities [38].

1.2.4 Wireless pressure sensors

Wireless sensing of physical and chemical parameters is highly desirable when physical access is limited, e.g. devices for the biomedical industry and for hazardous environments [39, 40]. Wireless sensing can be achieved both in an active or in a passive way. An active device has to be implemented with a microchip powered by a battery or inductively coupled power supply to make measurements [41, 42], while a passive wireless sensors can be made both with Surface Acoustic Waves (SAW) or with LC resonators [39, 43]. These can be measured remotely without any implemented power supply, giving passive devices the possibility of unlimited lifetime. The drawback is a limited interaction distance. The wireless development is closely linked to the medical industry since it opens new possibilities for monitoring of human parameters inside the body. In 1967 Collins et. al. [39] made a intraocular pressure sensor based on the LC resonance method with a sensitivity of 1 MHz/mmHg. As the IC technology was developed it gave engineers a toolbox for developing more compact system. In 1998 Park et. al. [44] made a wafer level hermetically sealed wireless pressure sensor with an integrated LC resonator in bulk micro machining, where electroplating, anodic bonding and an implanted boron etch stop were used to achieve a footprint of $3\times3\times1.6$ mm. The sensitivity was estimated to 2 MHz/mmHg with a resonant frequency of approximately 500 MHz. In 2001 Akar. et. al. [45] presented a batch fabricated sealed pressure sensor with a measured sensitivity of 120 kHz/mmHg in a pressure range of 0-50 mmHg. The development has continued to produce passive wireless sensors for measuring the cerebral ventricle pressure [46] and a comercially CardioMEMS product to measure aneurysm sac pulse pressure [47]. Finally, in 2007, Wise [48] predicts a future were MEMS of different type will be part of wireless integrated microsystems that will serve as the front-ends of information networks used in a huge variety of contexts; capacitive wireless pressure sensor is seen as one of the most probable candidate to be integrated in these systems.

1.3 Motivations

This project has been supported by Grundfos with the purpose of developing a demonstrator of a pressure sensor with the signal conditioning electronics fitting the existing packaging solution (see Fig. 1.11). The sensor proposed is designed to be an absolute pressure sensor for harsh environment, a product which is still missing in the company portfolio. Grundfos in fact produces differential pressure sensors with a maximum pressure range of 6 bar and relative pressure sensors with a range of 10 bar and 1 mbar resolution. Both pressure range and resolution can be improved employing capacitive sensing. Furthermore, capacitive sensors have three important advantages over their piezoresistive counterparts:

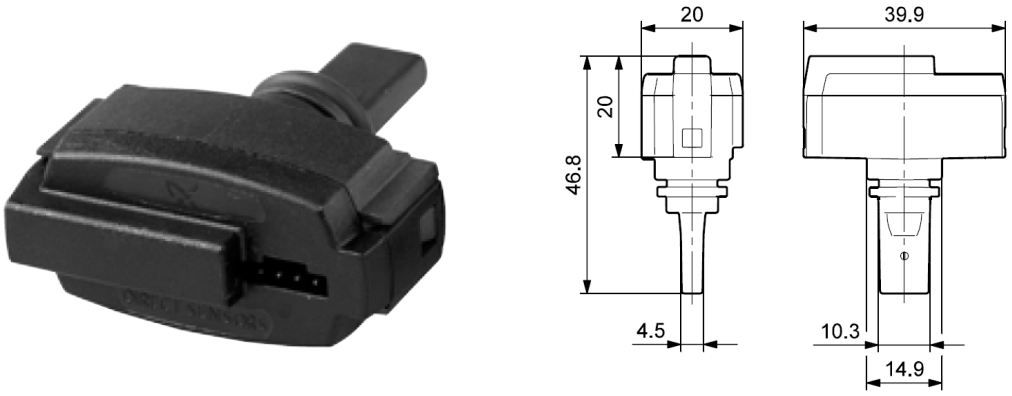

Figure 1.11: Grundfos packaging solution for micromachined pressure sensors: the existing packaging solution pose a requirement on the size of the die and interface electronics of the capacitive pressure sensor developed. On the right sketches the dimensions of the case are reported in millimeters.

- Dimensions: since in the capacitive sensor there is no need to have resistors on the membrane, the device can be scaled down in an easier way than the piezoresistive one.
- Power consumption: except for biasing there's virtually no power consumption with capacitive detection since the sensing element works with AC signals.
- Temperature sensitivity: provided a vacuum sealed cavity the capacitive device is insensitive to changes in temperature while the piezoelectric one does not have this remarkable feature since the piezo-coefficient π_{44} is temperature dependent.

Since the MEMS market is mainly driven from dimensions, power consumption and costs, and given the fact that wireless applications heavily rely on small, low power devices, CPS are definitely worth being investigated.

1.4 Results overview

Here the results obtained during this 3-years Ph.D. project in development of MEMS capacitive pressure sensor with signal conditioning electronics are briefly introduced. Firstly a mathematical model which describes with excellent accuracy the behavior of these type of sensors has been formulated and benchmarked against a finite element simulation. This model has been used as a designing tool for the numerous batches of transducers fabricated in a cleanroom facility. Most of these batches gave encouraging results consisting of touch mode sensors with high sensitivity, up to 800 fF/kPa (largely superior to VTI SCP1000 which has a maximum sensitivity of 55 fF/kPa), tunable pressure range and very low hysteresis, less than 1% in the entire pressure range. Different interfacing circuits for capacitive sensors have been studied, simulated, mounted and tested. One of them, the AC-Bridge circuit, has been implemented on a Grundfoss PCB which are desinged to fit the exsisting packaging solution. Finally a complete prototype was built and preliminary test have shown a sensitivity of 0.25 mV/kPa in normal mode and 1.8 mV/kPa in touch mode. In Chapter 5 a closer look on all the significant mea-

surements performed in order to characterize the sensor, the electronics and the full system is taken.

1.5 Dissertation outline

This dissertation is divided into six chapters and one appendix. In the following an outline of the remainder of the thesis is given.

- **Chapter 2:** Capacitive pressure sensor mathematical model. This chapter describes exact and approximate solutions for normal mode and contact mode plate deflection respectively. The deflection profile is then used to evaluate the capacitance of TMCPS and to obtain important process parameters. Furthermore, the model is validated with finite element calculations.
- **Chapter 3:** Device fabrication. This chapter presents the process flows implemented in a cleanroom facility to produce different batches of touch mode capacitive pressure sensor (TMCPS). The cleanroom techniques are briefly described and various improvements such as hysteresis reduction and gold coating are presented.
- **Chapter 4:** Interfacing circuits for TMCPS. Here different capacitance readout methods are presented. The fabrication of design discussed is analyzed and compared to the simulation results. In some cases thermal characterization of the PCBs is presented. Finally, the circuit chosen for the prototype implementation is described.
- **Chapter 5:** Measuremets and results. All the significant data collected in this project are here depicted. Characterization of the sensor, the electronics and the final prototype is widely investigated with numerous graphs and tables. Furthermore the measurement results are compared to the theoretical calculations presented in the previous chapters.
- **Chapter 6:** A conclusion on the project as a whole is given and the most important results are stated. Also, an outlook on the perspectives of the project is given.
- **Appendix A:** This appendix contains a list of contributions to various scientific journals and conference proceedings. These manuscripts describe some of the results of the project.

Chapter 2

Capacitive pressure sensor models

The micromachined capacitive pressure sensors presented in this dissertation share the same fundamental model, described by the governing equation for plate deflection. This equation needs to be solved in order to extract the correct process parameters to achieve, among other characteristics, the desired sensitivity and pressure range. In this chapter it is shown that only for some particular cases the exact analytical solution is known while approximate and/or numerical solutions are necessary to model the vast majority of the devices fabricated.

First, the theory of plate deflection is reviewed. This topic is crucial for the understanding of principles governing pressure sensors which convert a mechanical deformation into an electrical signal, being them capacitive or based on other type of transduction. The special case of contact mode is then studied both analytically and numerically. From the shape of the plate is then possible to evaluate the capacitance of the sensor which has also be done by means of an approximate solution and finite element calculations. Finally, a discussion on the models developed is presented in the conclusions.

2.1 Circular plate deflection

In this section the theory of plate deflection is reviewed with the purpose of applying it to the general structure of a capacitive pressure sensors (CPS). With this in mind a general cell of a CPS is drawn (Fig. 2.1), it consist of a plate and a substrate, both conductive, separated by insulating media (e.g. silicon dioxide and air). These sensors can be designed to work in normal mode, where the deflection of the plate is smaller than the cavity height, or in touch mode when the plate touches the insulator on the bottom electrode. Depending on the ratio between the height of the cavity (or gap distance) and the plate thickness, this type of sensors will work in a linear elastic regime or in a large deflection regime. Only the case of linear elastic deformations of a circular isotropic plate, i.e. the gap distance is less than half of the plate thickness [13, 49], is considered. The analysis starts with normal mode operations in Section 2.1.1 and continues with touch mode analysis in Section 2.1.2.

2.1.1 Normal Mode

Here the diaphragm type under consideration is that of a uniformly loaded circular plate with radius a_0 and thickness t, see Fig. 2.1. The mechanical properties of the plate are characterized by the isotropic Young's modulus E and the Poisson ratio ν. The differential equation, also

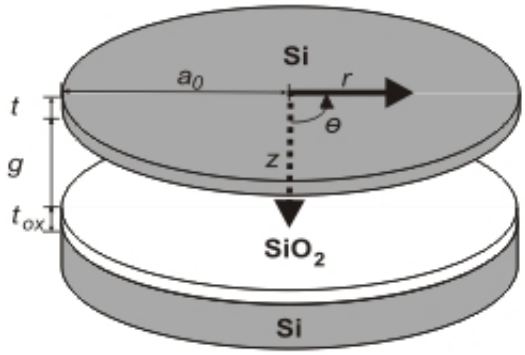

Figure 2.1: Schematic of the capacitive element. Both upper and lower plates are made of heavily doped silicon while the insulator layer is made of silicon dioxide. The polar coordinates used in this work are shown as well as some of the main dimensions such as the plate thickness t, the oxide thickness t_{ox}, the radius a_0 and the gap distance g.

called governing equation, describing the displacement as a function of the radial coordinate, $w(r)$, under pure bending can be written in terms of the applied external pressure, p, as [13]

$$D\nabla^2\nabla^2 w = p, \tag{2.1}$$

where D is the flexural rigidity of the plate given by

$$D = \frac{Et^3}{12(1-\nu^2)}. \tag{2.2}$$

To simplify determination of the constants of integration in a solution to Eq. (2.1) it is useful to calculate the shearing force per unit length F in the plate; F can be calculated from the force balance equation

$$2\pi rF = \int 2\pi prdr, \tag{2.3}$$

where r is the radial position, therefore

$$F(r) = \frac{pr}{2} + \frac{c}{r}, \tag{2.4}$$

where c is a constant of integration. In the normal mode case c is trivially zero as can also easily be seen if a definite integral had been used in Eq. (2.3); however, in the touch mode case which we shall consider later $c \neq 0$ and then Eq. (2.4) is needed for identification of c. Thus the deflection of a circular diaphragm fixed at the perimeter can be obtained solving Eq. (2.1) [13]

$$w(r,p) = \frac{pa_0^4}{64D}\left(1-\left(\frac{r}{a_0}\right)^2\right)^2 \equiv w_0\left(1-\left(\frac{r}{a_0}\right)^2\right)^2, \tag{2.5}$$

where w_0 is referred to as the center deflection and is a function of the pressure p. Being an exact solution, Eq. 2.5 does not need to be validated with finite element simulations and is used in Section 2.2 to evaluate the capacitance of the sensor cell of Fig. 2.1 as a function of the pressure.

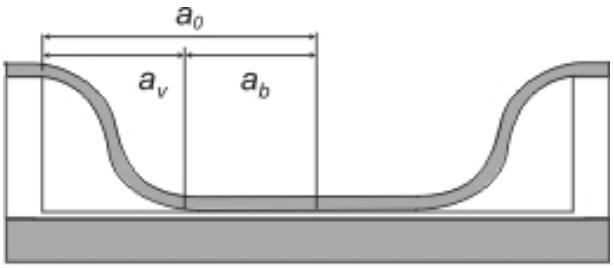

Figure 2.2: Touch mode operation. When the sensor is working in touch mode the problem is split into two parts: the touching circular area of radius a_b and the untouched area which is an annular region of inner radius a_b and outer radius a_0; a_v is defined as the difference between the outer and the inner radii.

2.1.2 Touch mode

When the top diaphragm of the capacitor comes into contact with the fixed bottom plate a transition occurs to a different operation mode, referred to as touch mode (see Fig. 2.2). In this case, the center point of the plate is no longer a part of the solution of Eq. (2.1) and the shearing force must vanish at the touching line so the constant of integration of Eq. (2.4) assumes the following value

$$c = -\frac{1}{2}a_b^2 p, \tag{2.6}$$

where a_b is the radius of the touching surface. With this assumption, the governing equation has been solved [13] but, even neglecting the stretching effect in the plate, the expression obtained is not suitable for the evaluation of the capacitance as a function of the applied load done later on in this section. A simpler approach considers the total capacitance as being made up by two distinct parts [50, 51]. One is given by the part of the diaphragm where the two electrodes are separated by the insulating oxide. This part is a simple parallel plate capacitor with a fixed oxide gap of t_{ox} and a radius a_b that increases with an increasing pressure. The second is given by the annular part of the diaphragm which is not touching the bottom electrode and has a fixed outer radius a_0 but a varying inner radius a_b which increases with increasing pressure, thus decreasing the area not touching the bottom electrode (the total area subtracted the area touching the bottom electrode). Therefore, we will assume that the deflection function in touch mode can be approximated by

$$w(r,p) = \begin{cases} g & 0 < r < a_b(p) \\ g\left(1 - \left(\frac{r-a_b(p)}{a_v(p)}\right)^2\right)^2 & a_b(p) < r < a_0 \end{cases}, \tag{2.7}$$

where the radius of the plate touching the bottom of the cavity, a_b, is a function of pressure as is also the part of the diaphragm not touching the bottom plate, a_v. Furthermore, Eq. (2.7), which will be used to model the shape of the deflected plate, is seen to satisfy the boundary conditions

$$w(a_0) = 0, \quad \tfrac{dw}{dr}|_{r=a_0} = 0, \quad w(a_b(p)) = g, \quad \tfrac{dw}{dr}|_{r=a_b(p)} = 0. \tag{2.8}$$

Note that $a_0 - a_b = a_v$, thus there is only one independent variable. Inspired by the work of [50, 51], we calculate the variable a_v by considering only the part of the plate bending, excluding the part touching the bottom of the cavity. In the simplified model proposed, the

center point deflection is forced to equal the gap distance $w(0,p) = w_0 = g$. If the membrane only touches in the center point $a_v = a_0$, and the pressure is obtained from Eq. (2.5). We now assume that Eq. (2.5) remains valid at higher pressures if a_0 is replaced by a_v and thus

$$a_v(p) \equiv \left(\frac{64Dg}{p}\right)^{1/4}. \tag{2.9}$$

In other words the radial deflection profile of the part of the diaphragm not touching the bottom electrode is taken to be the same as that of the diaphragm in normal mode. This will be shown, in Section 2.3, to be a reasonable assumption as has been shown for the case of large deflection [50, 51]. There, both the shape of the plate and the capacitance calculated in Section 2.2 are validated using a finite element software.

2.2 Capacitance evaluation

The capacitance-pressure curve (C-P) describing the behavior of a micromachined TMCPS can be divided into three different zones of interest: normal, transition and touch mode [17]. The region before the top plate reaches the bottom of the cavity is referred as the normal mode operation. Around the point where the plate touches the bottom of the cavity there is a highly nonlinear relationship between capacitance and pressure where the sensor is said to be in the transition zone. Finally, when the membrane is in contact with the insulator layer, which is placed on the bottom of the cavity to avoid short circuit of the device, the sensor works in touch mode. The capacitance in normal mode is calculated integrating the shape of the plate described in Eq. ((2.5)) over the radial distance as

$$C = \int_0^{2\pi}\int_0^{a_0} \frac{\varepsilon_0\varepsilon_{ox} r dr d\theta}{t_{ox} + \varepsilon_{ox}(g - w(r))} = C_0 \frac{\operatorname{arctanh}(\sqrt{\xi})}{\sqrt{\xi}}, \tag{2.10}$$

where ξ is the ratio of the center deflection to the effective thickness of the dielectric

$$\xi \equiv \frac{w_0}{g\left(\frac{t_{ox}}{g\varepsilon_{ox}} + 1\right)}, \tag{2.11}$$

and

$$C_0 \equiv \frac{\pi\varepsilon_0\varepsilon_{ox}a_0^2}{g\varepsilon_{ox} + t_{ox}}, \tag{2.12}$$

is the parallel plate capacitance for a vacuum-gap distance of g and a thin insulation layer of oxide on the bottom plate of thickness t_{ox} and relative dielectric constant ε_{ox}. The capacitance in touch mode using Eq. (2.7) is found to have an analytical expression

$$\begin{aligned} C &= \int_0^{2\pi}\int_0^{a_0} \frac{\varepsilon_0\varepsilon_{ox} r dr d\theta}{t_{ox} + \varepsilon_{ox}(g - w(r))} \\ &= \frac{\varepsilon_0\varepsilon_{ox}\pi a_b^2}{t_{ox}} + \frac{2\pi\varepsilon_0\varepsilon_{ox}}{g\varepsilon_{ox} + t_{ox}} \int_{a_b}^{a_0} \frac{r}{1 - \gamma\left(1 - \left(\frac{r-a_b}{a_v}\right)^2\right)^2} dr, \end{aligned} \tag{2.13}$$

where

$$\gamma \equiv 1/\left((t_{ox}/g\varepsilon_{ox}) + 1\right), \tag{2.14}$$

is a constant related to sensor design and attains a value between zero and one, $\gamma \in]0;1[$. For a large gap distance compared to the oxide thickness, γ will be close to 1. This is an interesting case which is considered in the following section since such a design has the largest sensitivity. Introducing a change of variables $u \equiv (r-a_b)/a_v$, the integral χ of Eq. (2.13) can be further simplified

$$\chi = \int_{a_b}^{a_0} \frac{r}{1-\gamma\left(1-\left(\frac{r-a_b}{a_v}\right)^2\right)^2} dr \tag{2.15}$$

$$= a_v^2 \int_0^1 \frac{u}{1-\gamma(1-u^2)^2} du + a_b a_v \int_0^1 \frac{1}{1-\gamma(1-u^2)^2} du$$

$$\equiv \left(k_1 a_v^2 + k_2 a_b a_v\right), \tag{2.16}$$

where the two integrals k_1 and k_2, are independent of the pressure. These two integrals can be solved analytically as follows:

$$k_1 = \frac{1}{2} \frac{\operatorname{arctanh}\sqrt{\gamma}}{\sqrt{\gamma}} \tag{2.17}$$

$$k_2 = \frac{\arctan\left(\frac{\sqrt{\gamma}}{\sqrt{\sqrt{\gamma}-\gamma}}\right)}{2\sqrt{\sqrt{\gamma}-\gamma}} + \frac{\operatorname{arctanh}\left(\frac{\sqrt{\gamma}}{\sqrt{\sqrt{\gamma}+\gamma}}\right)}{2\sqrt{\sqrt{\gamma}+\gamma}}, \tag{2.18}$$

where both k_1 and k_2 vary from 0 to ∞ as γ varies from 0 to 1.

Inserting Eq. (2.16) in Eq. (2.13) and rearranging in terms of the virtual radius a_v the capacitance in touch mode can be written as

$$C = C_{ox}\left(\left(1+2\frac{k_1-k_2}{\frac{g\varepsilon_{ox}}{t_{ox}}+1}\right)\frac{a_v^2}{a_0^2} + 2\left(\frac{k_2}{\frac{g\varepsilon_{ox}}{t_{ox}}+1}-1\right)\frac{a_v}{a_0}+1\right), \tag{2.19}$$

where C_{ox} is the oxide capacitance

$$C_{ox} \equiv \varepsilon_0 \varepsilon_{ox} \frac{\pi a_0^2}{t_{ox}}. \tag{2.20}$$

Thus, the capacitance of a sensor in touch mode can be described as a second order polynomial in terms of a_v which is linked, as shown in Eq. (2.9), to the applied pressure.

2.2.1 Special case $g\varepsilon_{ox} \gg t_{ox}$

The special case, where the product of the gap distance and the dielectric constant of the oxide is much larger than the oxide thickness, is interesting from a device design point of view, when high sensitivity is desired. Using this assumption in Eq. (2.19) together with Eq. (2.9) and defining

$$\kappa = a_0^4/(64Dg), \tag{2.21}$$

the capacitance becomes

$$C \approx C_{ox}\left(\sqrt{\frac{1}{\kappa p}} - 2\sqrt[4]{\frac{1}{\kappa p}} + 1\right), \tag{2.22}$$

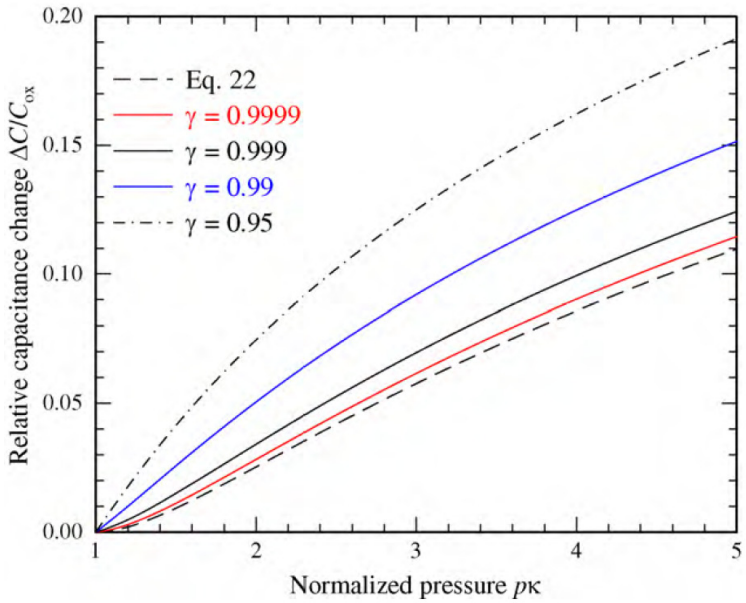

Figure 2.3: Comparison between the touch mode capacitance, Eq (2.19), as a function of normalized pressure κp calculated at different values of γ and the capacitance calculated from Eq (2.22).

and it is seen that C is a polynomial in $(\kappa p)^{-1/4}$. Note, that also the capacitance of Eq. (2.19) is a second order polynomium in $(\kappa p)^{-1/4}$, the coefficients though are different and are functions of γ only. This makes it simple to fit the capacitance-pressure curve in touch mode, as it can be seen in Section 4. Even though the results obtained will show that, in our case, this approximation gives a simple and reliable way to estimate the characteristics of the device fabricated, it should be kept in mind that it is based on the fact that the two terms $(k_1 - k_2) / \left(\frac{g\varepsilon_{ox}}{t_{ox}} + 1\right)$ and $k_2 / \left(\frac{g\varepsilon_{ox}}{t_{ox}} + 1\right)$, in Eq. (2.19), were taken to be negligible and that will intrinsically affect the accuracy of this model. For the sensor fabricated, $\gamma = 0.982$ and these two terms are -0.127 and 0.151 respectively.

In Fig. 2.3 the relative capacitance change $\Delta C/C_{ox}$ from Eq. (2.19) is plotted as a function of normalized pressure κp at different values of γ; for comparison also Eq. (2.22) is shown and it is seen that as γ approach 1 the two expressions agree.

2.2.2 Sensitivity

The sensitivity, S, of any type of capacitive pressure sensor can be evaluated taking the first derivative of the C-P curve with respect of pressure. Generally in a fabricated device, the special case described in the previous section is verified, therefore the C-P curve in normal mode is given by

$$C_{NM} = C_0 \sqrt{\frac{p_t}{p}} \operatorname{arctanh} \sqrt{\frac{p}{p_t}}, \tag{2.23}$$

and in touch mode

$$C_{TM} = C_{ox} \left(\sqrt{\frac{p_t}{p}} - 2\sqrt[4]{\frac{p_t}{p}} + 1 \right), \tag{2.24}$$

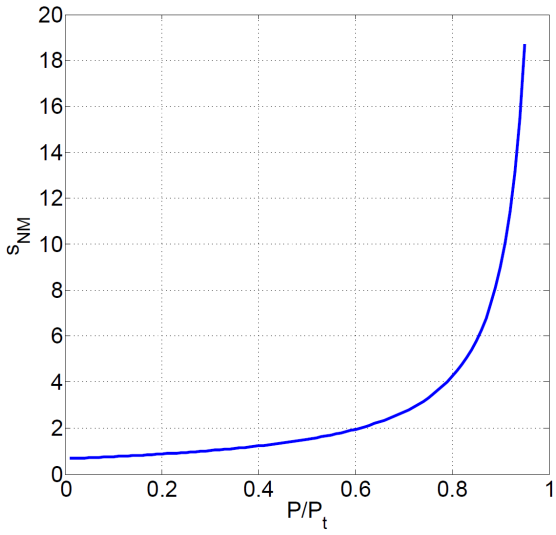

Figure 2.4: Normalized sensitivity in normal mode regime. The pressure is varied from 0 up to almost touch point pressure where the simplified model cannot approximate the C-P curve.

with the touch pint pressure, p_t, defined from

$$p_t = \frac{1}{\kappa} = (64Dg)/a_0^4. \tag{2.25}$$

Deriving with respect to pressure Eq. 2.23 and Eq. 2.24 the sensitivities in normal and touch mode respectively are calculated. The normalized sensitivity is then given by

$$s_{NM} = \frac{2S_{NM}p_t}{C_0} = \frac{p_t}{p}\frac{1}{1-\frac{p}{p_t}} - \sqrt{\left(\frac{p_t}{p}\right)^3}\operatorname{arctanh}\sqrt{\frac{p}{p_t}}, \tag{2.26}$$

in the normal mode case and by

$$s_{TM} = \frac{2S_{TM}p_t}{C_{ox}} = \sqrt[4]{\left(\frac{p_t}{p}\right)^5} - \sqrt{\left(\frac{p_t}{p}\right)^3}, \tag{2.27}$$

in the touch mode regime. From Fig. 2.4 is possible to notice that, in normal mode, the sensitivity grows very slowly and almost linearly for pressure values up to 60% of p_t, then it rises steeply as the cusp is approached (i.e. as the ratio between the pressure and the touch point pressure gets closer to 1). The sensitivity in touch mode has instead a maximum value near touch point pressure and then slowly decreases for pressures 4 or more times bigger than the touch point pressure as it is illustrated in Fig. 2.5. It is clear that the simplified models proposed fail around touch point which is a not differentiable point of the C-P curve.

2.3 Finite element validation

For the finite element model (FEM) the COMSOL Multiphysics stress-strain application mode has been chosen in order to validate the deflection profile suggested in Section 2.1. When using finite element analysis (FEA) methods it is always advisable to exploit the geometrical

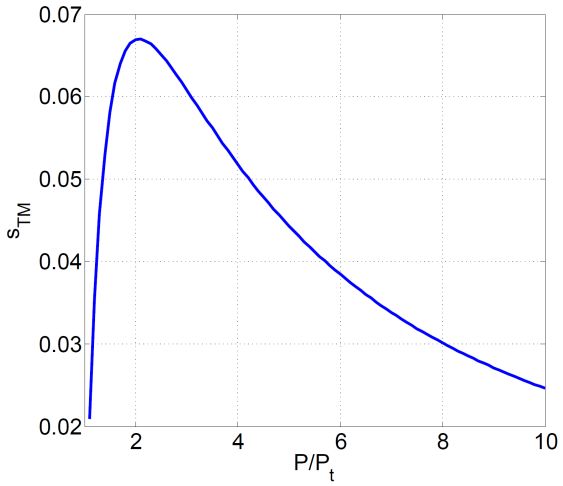

Figure 2.5: Normalized sensitivity for touch mode operations. After a maximum value the sensitivity in touch mode slowly decreases.

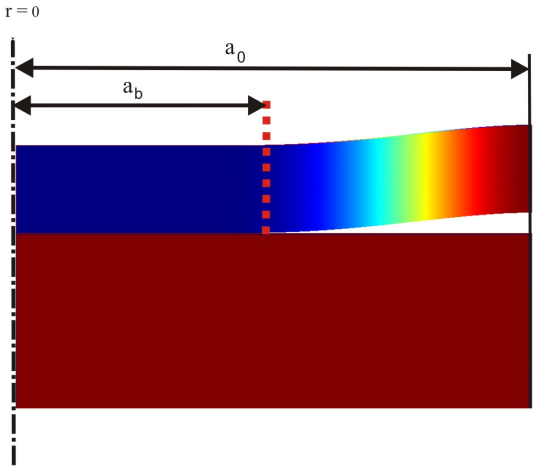

Figure 2.6: Schematic drawing of the finite element model (FEM) with the solution for the mechanical problem overlaid. The axial symmetry of the problem is exploited with respect to the centerpoint of the membrane at $r = 0$. The touching part of the membrane has the radius a_b, while the total radius of the membrane is a_0.

Subdomain	**Geometrical constants**		**Mechanical-electrical parameters**			**Boundary Conditions**			
	$a_0(\mu\text{m})$	$t(\mu\text{m})$	$E[GPa]$	ν	ε_r	$r=0$	$r=a_0$	Top	Bottom
Plate	75	2	170	0.28	-	A.S.	Free	Free	Free
Substrate	75	6	170	0.28	-	A.S.	Free	Free	Fixed
Air gap	75	0.5	-	-	1	A.S.	Z.C.S	1V	Free
Insulator	75	0.03	70	0.17	4.2	A.S.	Z.C.S.	Free	0V

Table 2.1: Parameter used for the FEM simulations. The geometrical and electromechanical properties are of course the same used in the analytical model.

symmetries of the structure to reduce computational time. Therefore, we assume 2D axial symmetry as shown in Fig. 2.6. Only 2 subdomains have been defined: a silicon plate, on top of which a distributed load will be applied and parameterized, and a silicon substrate which is kept fixed. The geometrical dimensions, the material's property and the boundary conditions (BC) of the two subdomains are seen in Table 2.1. It is important to underline that the bottom boundary of the plate (which lies at z=0 if no load is applied) is defined as the slave boundary while the top surface of the substrate is defined as the master when specifying the contact pair necessary to simulate touch mode operations [52].

Fig. 2.7 shows the deflection profiles for different pressure values calculated using Eq. (2.5) and (2.7) of the analytical model (indicated with "(A)" in the legend) and the one estimated by FEA (indicated with "(FEM)"). Fig. 2.8 shows the root of squares error (RSE) for the analytical model with regards to the FEM that has been calculated at five different pressure values with

$$RSE = \sqrt{\sum_{i=0}^{75} (w_{A,i\Delta r} - w_{FEA,i\Delta r})^2}, \tag{2.28}$$

where $w_{A,i\Delta r}$ and $w_{FEA,i\Delta r}$ are the analytical and finite element deflection profiles at the radial coordinate $i\Delta r$ and Δr is the discretization step chosen (i.e. 1 μm in the code developed). The analytical model and the FEM is in good quantitative agreement below the touch point pressure. Above the touch point pressure the deviation between the analytical model and the FEM increases with pressure. Although the analytical model and the FEM are not in quantitative agreement they match qualitatively across the whole pressure range. The reason behind the mismatch is the different boundary conditions assumed in the analytical model and the FEM. In the case of the analytical model at the touch point pressure and beyond the plate bending is fixed to have infinite curvature at the touch point. This strong boundary condition leads to a higher stiffness (leading to a reduced deflection) of the plate compared to the one predicted from FEA. The FEM better resemble the real physical problem which does not have the constraint of infinite curvature at the touch point. From Fig. 2.7 this difference in boundary condition is also seen to lead to a non-trivial shape of the deflection that cannot be described by simple mathematical expressions.

Two different frameworks need to be introduced when dealing with a multiphysics problem in COMSOL, one for the stress-strain application mode and the other for the electrostatic one. In the electrostatic model, a new subdomain is defined which is the air gap. This domain needs to be meshed in order to compute the electric field in this media. Due to the deformation of the plate under different loads, a moving mesh application is specified in the electrostatic model domain. Furthermore, the change in topology occurring when the sensor goes in contact mode

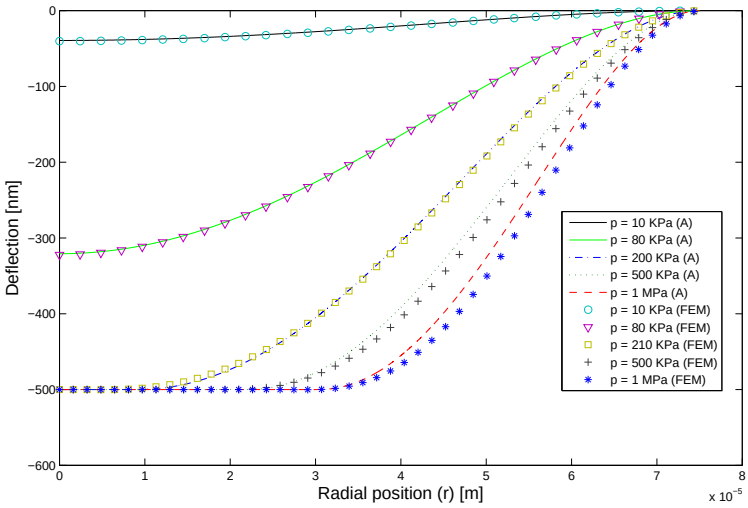

Figure 2.7: Graph of the plate deflection (in nm) as a function of the radial position (in m) for different pressures. The analytical model is marked by (A) and plotted as lines, while the FEM is marked by (FEM) and plotted as points.

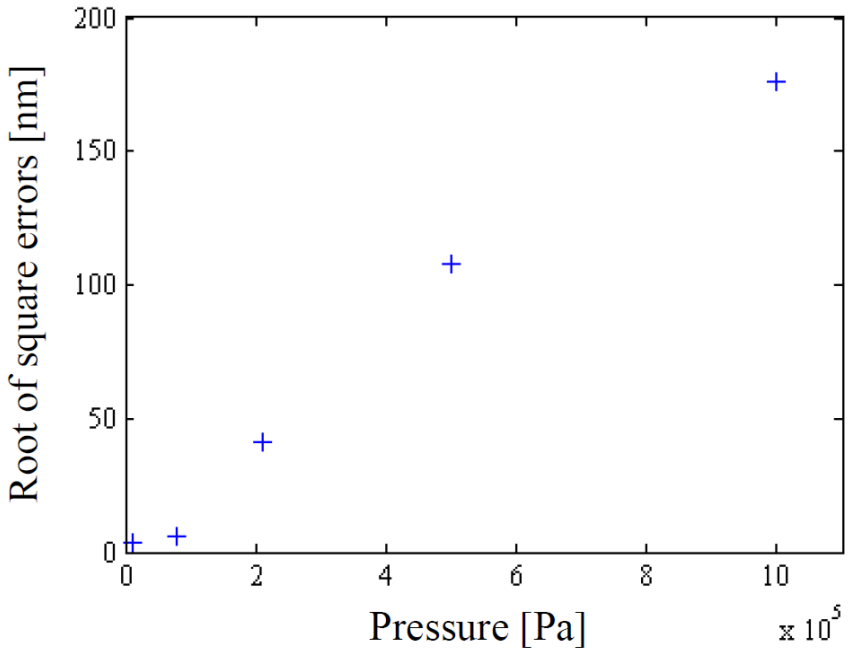

Figure 2.8: Graph of the root of square error (RSE) versus pressure. The error between the analytical and the numerical model is almost negligible when the exact solution (normal mode) is used to evaluate the capacitance while it increases sensibly in the touchmode regime.

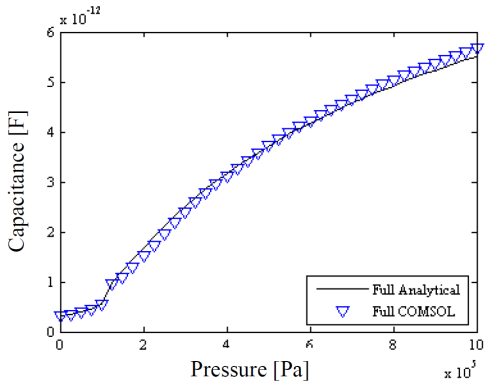

Figure 2.9: Graph of the capacitance (in Farads) as a function of the pressure (in Pascals) for the analytical model (line) and the FEM (triangle).

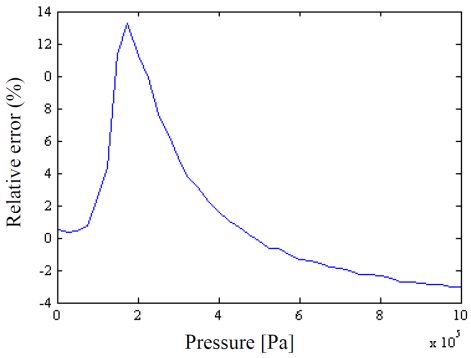

Figure 2.10: Graph of the relative error of the analytical model as compared to the FEM. The analytical model does not take into account the transition region, thus the peak around touch point.

demands for a solution of the electric field for each pressure step. Therefore, the capacitance-pressure curve has been obtained with a 3-step procedure for each single pressure value: first the structural mechanics problem including contact and moving mesh is solved, then the deformed geometry/mesh from the previous step is saved and finally the electrical problem on the deformed geometry is solved. Doing so we have assumed that the two physical domains can be uncoupled (i.e. the electrical problem does not affect the structural mechanics). This is a reasonable assumption given the mechanical pressure compared is order of magnitudes larger than the electrostatic pressure in the whole pressure range apart from close to the touch point. In the transition region between normal mode and touch mode we expect a larger contribution of the electrical forces. A MATLAB script has been used to automate the 3 step evaluation procedure. Fig. 2.9 shows the comparison between the curve calculated with the analytical model and the one obtained using FEA. The error between the two is illustrated in Fig. 2.10. Up until 4 bar the analytical model overestimate the capacitance while, for higher pressure values, it underestimates the capacitance.

As a final remark it is important to evaluate the convergence of the FEA model and to compare the two codes in terms of computational complexity and speed of computation. The finite elements software uses two different solvers in order to obtain the plate deflection profile, namely the nonlinear and the augmented Lagrangian solver. In both cases error tolerances have been set to the default value and the two solvers reach convergence within the maximum number of iterations allowed (which also was left untouched). Another aspect important to evaluate is the convergence of the results as the mesh is made finer. On the left plot of Fig. 2.11 the convergence of the capacitance calculated with the FEA software as the mesh is made finer is shown. For mesh maximum dimension allowed smaller than 5ìm no appreciable improvements are seen. At 1KPa a capacitive value of around 0.549pF has been found with the finest mesh allowed which match extremely well the one of 0.563pF calculated using the analytical model. Finally, from the right plot in Fig. 2.11, is possible to notice that the relative error between the coarsest mesh and the finest has a maximum value of 0.6% which is reached around touch point.

As expected, it has been found that the computational complexity of the two methods in-

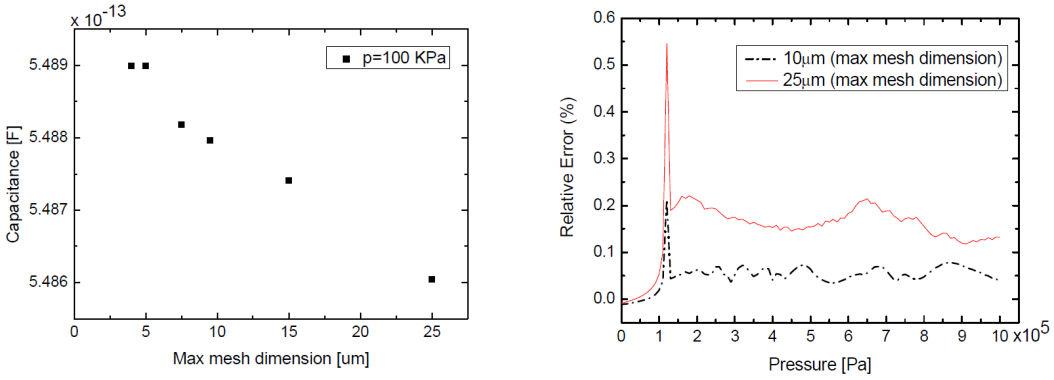

Figure 2.11: On the left the capacitance as a function of the maximum dimension of the mesh element allowed in the FEA software is plotted. The values are plotted for an applied load of 100 kPa which results in a capacitance of 0.562Pf if calculated with the analytical model. On the right the relative error between two different mesh and the finest mesh available is shown.

creases linearly with the number of pressure points considered. The same behavior is found for the analytical code as the radius of the plate is discretized in smaller elements. However this does not happen for the finite element model where the time required to solve the problem increases non linearly when the mesh is refined.

2.4 Conclusion

In this chapter an analytical model for the deflection shape and capacitance of a touch mode pressure sensor has been presented. In Chapter 5 the agreement between the analytical model and the experimental data is exploited and here is demonstrated that this is because the approximated deflection shape compares well with the exact solution. This has been shown through FEA of the mechanical problem. The FEM is also used to compute the capacitance of the pressure sensor in both normal mode and touch mode and good agreement, within 14% is achieved. The deviation is largest at the transition region, for which the mechanics is accurately captured by the FEM. In conclusion the analytical model for a touch mode capacitive pressure sensor has been shown to agree well with FEM. The analytical model provides an understanding on how the deflection and capacitance depends on the physical parameters of the sensors. This provides a clear picture of the physics underlying the pressure sensor operation and provides equations for design in terms of key parameters such as sensitivity, touch point pressure etc. This is necessary to obtain a proper design of a TMCPS which fabrication is described in the next chapter.

Chapter 3

Touch mode capacitive pressure sensor fabrication

In the previous chapter a mathematical toolbox which can be use to design touch mode capacitive pressure sensors (TMCPS) has been described. The code written is also used to fit the measurement data collected from the devices which fabrication is described in this chapter. The topic of this chapter is, in fact, the cleanroom fabrication process developed to produce TMCPS.

Many small variations have been introduced since, in 2006 the first process flow was proposed from Thomas Pedersen, who is holding currently a post doctoral position at DTU Nanotech. None the less, this chapter starts from the description of the original process flow which is necessary in order to understand the modifications and improvements brought about in this project. In 2007, the author of this work, has investigated, during his M.Sc. project, the possibility of fabricating capacitive sensor with ultra thin membrane (i.e. 340 nm) working under the large deflection assumption and has firstly introduce an interfacing solution for these transducers. The results of that work are omitted in order to avoid confusion between two different sensor concept (i.e. small and large deflection devices). Here is instead discuss how, in this project, two mask steps of the original process are combined in a single step; this is certainly a topic of greater relevance also from the industrial perspective.

One of the well known problems of all the elastic types of pressure sensors is hysteresis, namely the different input/output characteristic that can be seen when pressure is increased and decreased in a given range. TMCPS normally exhibits a strong hysteresis which can be significantly reduced with an extra mask step as it is shown in this chapter. Then a brief look to some of the most critical steps in the fabrication of TMCPS is taken with the aim of foreseeing possible issues in a future technology transfer process between DTU Danchip and Grundfos. Finally, all the knowledge acquired on the fabrication of TMCPS is summarized in the conclusion.

3.1 Touch mode capacitive pressure sensors design

Micromachined capacitive pressure sensors have been previously introduced in this dissertation (see Section 1.2.2), where a state-of-the-art for these kind of devices has been presented. A micromachined capacitive pressure sensor which allows the sensing element to flatten onto an insulation layer deposited on the bottom electrode is known as touch mode capacitive pressure sensor (TMCPS). The TMCPS was firstly introduced in 1990 by Ding et al. [53], while an array

of capacitive sensing elements in parallel was presented in the work of Dudaicevs et al. [54] in 1994. The MEMS fabricated in this project is a TMCPS which is made of an array of elements supported by a SiO_2 honeycomb structure.

The basic fabrication process, where the top plate is defined in the device layer (DL) of a silicon on insulator wafer (SOI), while the bottom plate and the support structure are fabricated on a double side polished wafer (DSP), can be summarized with the following basic steps:

1. Making the capacitor plates by wafer doping (both SOI and DSP).
2. Growing an oxide layer on the DSP wafer.
3. Etching of the cavities and the support structure in the oxide grown on the DSP.
4. Etching an insulating groove on the SOI wafer to separate the active area from the rest of the die.
5. Growing a thin insulation layer on the bottom plate to avoid short circuit when working in touch mode.
6. Fusion bonding the wafers.
7. Removing the handle wafer and some of the box oxide of the SOI wafer.
8. Metal deposition of contacts for wire bonding.

The process is described in details in the next section where a sketch of the flow helps to visualize the 8 steps just mentioned. Here the focus is mainly on the constraints which have been discussed together with Grundfos in order to achieve the best possible result: a functional proof of concept of a TMCPS with interfacing electronics and packaging.

There are of course a huge number of options available when a TMCPS is designed, for example, tuning the radius to gap distance ratio leads to the desired value for touch point pressure. Given a fixed gap distance (of 550 nm) and plate thickness (of 2 μm), then plate radius is the parameter that is decisive to fix touch point pressure. If the process flow described above is considered, it is clear that gap distance and plate thickness are the same for all the sensors since they are defined by an etching process and the choice of the SOI wafer respectively. The radius of the plate can instead be tuned just by having different layouts on the same mask as it is shown in Figure 3.1.
In this project three different sensors have been designed, the first goes into touch mode around atmospheric pressure (1 bar), the second works in normal mode up to 2.2 bar while the third goes in touch mode at around 5.3 bar.

Using Eq. 2.5 in the previous chapter:

$$a_0 = \sqrt[4]{\frac{64D}{p}} w_0, \tag{3.1}$$

is it possible to calculate the corresponding radii which in turns are 75 μm, 62 μm and 50 μm respectively. The first option (i.e. touch point pressure at atmospheric pressure) is motivated by the possible comparison between the existing Grundfos RPS 0-1 and the new TMCPS, the second (i.e. touch point pressure at 2.2 bar) gives a wider normal mode range and can be used around barometric pressure, the last is the sensor with the widest pressure range, it has a wide

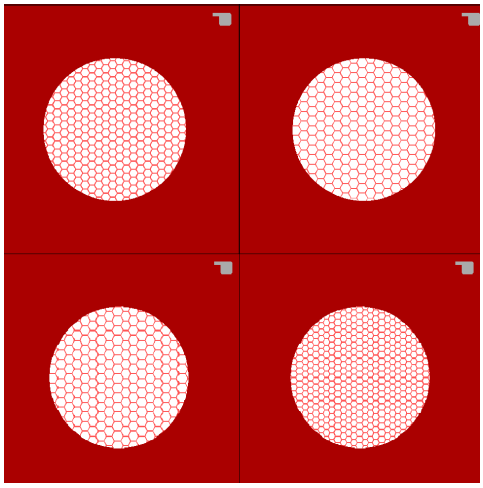

Figure 3.1: *Mask 1, zoom on selected circles to show the hexagons of different sizes. The bottom contact is seen in top right corners.*

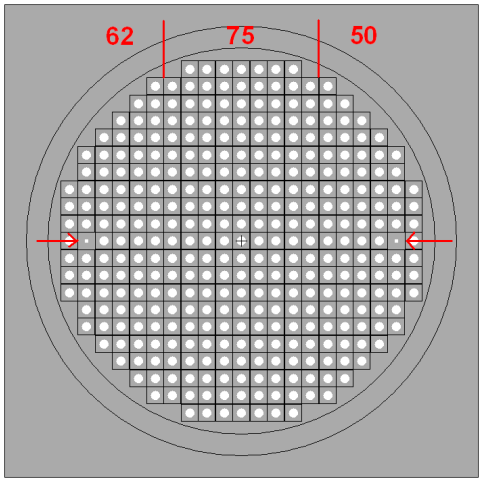

Figure 3.2: *Mask 1, Overview of the sensors position on the wafer. The arrow marks the position of the alignment marks.*

linear region both in normal mode and in touch mode. On a wafer scale the number of sensors of each type is roughly the same as it is shown in Fig. 3.2.

In this project, apart from touch point pressure, there are some other constraints given by the fact that a strong focus on the possibility of obtaining a new product is required. It also important to notice that good results are obtained only when a very broad perspective is kept, therefore many different solutions should be considered. In order to minimize the time to market the following considerations were done:

1. the size of the sensor should fit the actual casing/packaging solution (i.e. die: 4x4 mm, max hight 650um; active area: 2.1 mm in diameter),

2. possibility for a corrosion-resistant coating (i.e. flat active area) as it is done with Grundfos piezoresistive sensors,

3. simplest possible cleanroom process (i.e. minimum number of masks, use mostly standard processes and as many batch processes as possible),

4. improvement to the current solution (i.e. wider pressure range, higher sensitivity, lower power consumption, over pressure protection, reduced hysteresis).

Keeping these concepts in mind, different solutions are presented in the following part of this chapter. The first solution eliminates a mask step from the the first process flow. The second reduces the hysteresis of this kind of devices. The third adds a metal layer on top of the sensors fabricated with the actual process flow so that the electrical properties of a conductive coating can be investigated. Finally, section 3.3 is dedicated to test and consideration done to ease the technology transfer process that will lead to production of TMCPS in Grundfos facilities.

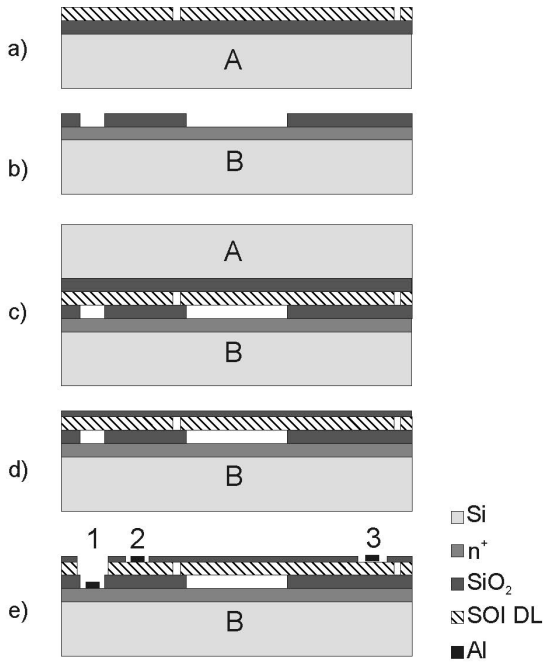

Figure 3.3: Process sequence for the capacitive pressure sensor. Note that the membrane support structure inside the cavity is not shown here. The DL of the SOI wafer has been given a separate color to make it easily distinguishable. The numbers 1-3 indicate contact numbers in accordance with the text.

3.2 Original process flow, mask design and modifications

In this section the original process flow (5-masks process), as Thomas Pedersen designed it, is described. A number of modifications to that process have been made. One of these, the three different radii size for the plate, has already been described in the previous section; the others, namely, the reduction of the number of masks, the hysteresis attenuation and the gold coating of the sensors are depicted here.

3.2.1 The 5-masks process

In the original process the sensor is fabricated from an SOI wafer (A) and a standard DSP wafer (B), the process flow is illustrated in Fig. 3.3. The device layer (DL) of wafer A acts as both top electrode and the sensor membrane. Wafer B forms the bottom electrode of the capacitor. Wafer A has a 2 μm thick device layer and a 1 μm buried SiO_2 layer. Both wafers are subjected to a one hour phosphorous predeposition using $POCl_3$ at 1000°C in the first processing step. SIMS analysis shows that this gives a peak phosphorous doping level of $7x10^{20}$ cm^{-3}, a sheet resistance of 1.5 Ω/square in the device layer of wafer A, and a 3 μm deep dopant profile into wafer B.

A 10 μm wide groove is etched into the device layer of wafer A, Fig. 3.3(a). It is etched all the way through to the buried oxide such that it serves as an electrical insulation between the active part of the device layer, e.g. the membrane area and the rest of the highly doped device layer. If these regions are not separated from each other the area outside the active membrane

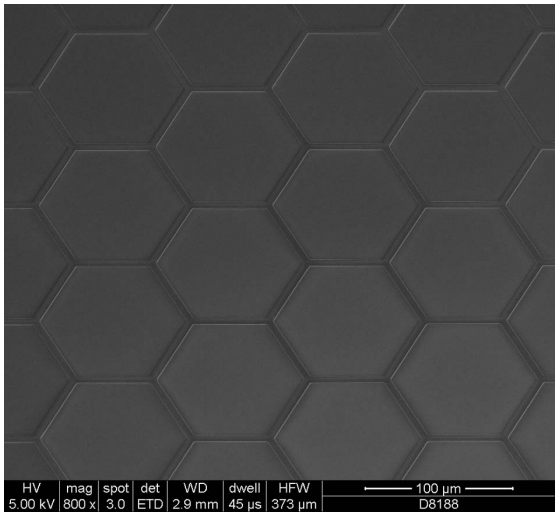

Figure 3.4: SEM image of the support structure etched into a 450 nm thick SiO_2 film. The line width of the support structure is 5 μm. The image is taken at an angle of 25°.

would add a considerable parasitic capacitance to the system, as it is estimated in Chapter 4. A 450 nm thick oxide is grown on wafer B and the cavity of the sensor is etched into this oxide, Fig. 3.3(b). The cavity is etched to form the hexagonal structure mentioned earlier. This etch is performed in a CF_4/CHF_3 Reactive Ion Etch (Surface Technology Systems). A SEM image (FEI Nova 600 NanoSEM) of the etched structure is seen in Fig. 3.4. A second oxidation is performed to re-grow a 30 nm SiO_2 layer in the bottom of the cavities, hereby the final gap distance of 420 nm stated earlier is reached. This SiO_2 layer serves as a short circuit protection for sensors used in touch mode operation.

Wafer A is turned upside down in order to fusion bond it front side to front side with wafer B as seen in Fig. 3.3(c). In this way the buried cavities are created. Bonding is done in vacuum (10^{-2} mbar nitrogen) in order to leave the cavity of the sensor evacuated for use as an absolute pressure sensor. The absence of gas in the cavity also ensures low temperature sensitivity. Before fusion bonding the wafers are cleaned and hydrated in a solution of sulfuric acid and hydrogen peroxide (4:1 ratio) and a solution of deionized water, 5% hydrofluoric acid and isopropanol (100:10:1 ratio). As part of the bonding process the wafers are annealed at 1000°C for one hour, this annealing step also serves as a drive in process for the phosphorous dopant. Alignment before fusion bonding is done by infrared alignment in an EVG 610 aligner and bonding is done in an EVG 520HE bonder. In this way an alignment accuracy better than 2 μm is achieved. Subsequently the handle wafer of A is etched away in an isotropic SF_6/O_2 plasma etch (STS ICP Advanced Silicon Etcher). Due to a very stable etch rate of the equipment and a high $Si:SiO_2$ selectivity of 80:1 it has proven as a very reliable method to use the buried oxide as an etch stop. The buried oxide is etched back to a thickness of 500 nm using BHF, Fig. 3.3(d). Hereby the membrane has a nominal thickness of 2.5 μm with 2 μm Si and 0.5 μm SiO_2. A cross sectional SEM image of the structure is seen in Fig. 3.5. At this point it is possible to deposit a thin film for corrosion protection. As the process leaves a uniform and flat surface at this point, there are no problems with step coverage and thus high quality protective coatings can be applied. No coating has however been applied in the first capacitive pressure

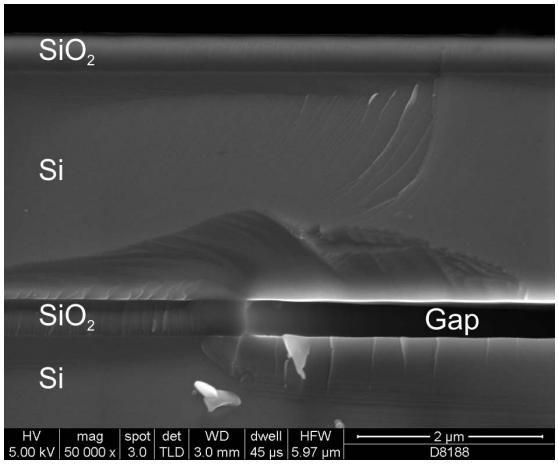

Figure 3.5: Cross sectional SEM image showing the bonded interface, the cavity and the Si/SiO_2 membrane. In this case the total membrane thickness is 2.9 μm instead of the intended 2.5 μm due to the uncertainty in device layer thickness of the SOI wafer.

sensor project developed.

Two contact holes are opened through the buried oxide layer that is now exposed, Fig. 3.3(e). One contact is made to the active membrane area (contact 3 in Fig. 3.3(e)) and another contact is made to the separated part of the device layer (contact 2). Another window is opened through the buried oxide layer and further through the device layer to reach the bottom electrode (contact 1). The contact areas are metalized with 1 μm Al by e-beam deposition and patterned by a phosphoric acid etch.

This process is fairly long, it consist of five masks and a couple of critical steps such has fusion bonding and handle removal. The lithographic steps performed are the following:

1. Mask 1: oxide etch in order to form the cavities and the support structure.

2. Mask 2: isolation groove etch with the purpose of separating the active area from the rest of the die.

3. Mask 3: top contact opening in the box of the SOI.

4. Mask 4: bottom contact opening in the box and DL of the SOI.

5. Mask 5: alluminum etch for contact release.

Except for the first mask, previously shown in Fig. 3.1, the mask's set is shown in Fig. 3.6. Here masks 2, 3 and 4 are of course of dark field type since the insulation groove and contacts area are the structure that needs to be etched. Only mask 2 is printed right reading since it is used on the DL which after bonding results upside down. The most prominent parasitic effect of this kind of sensors, namely their hysteresis, has been improved with the modification to the process flow described in the next section.

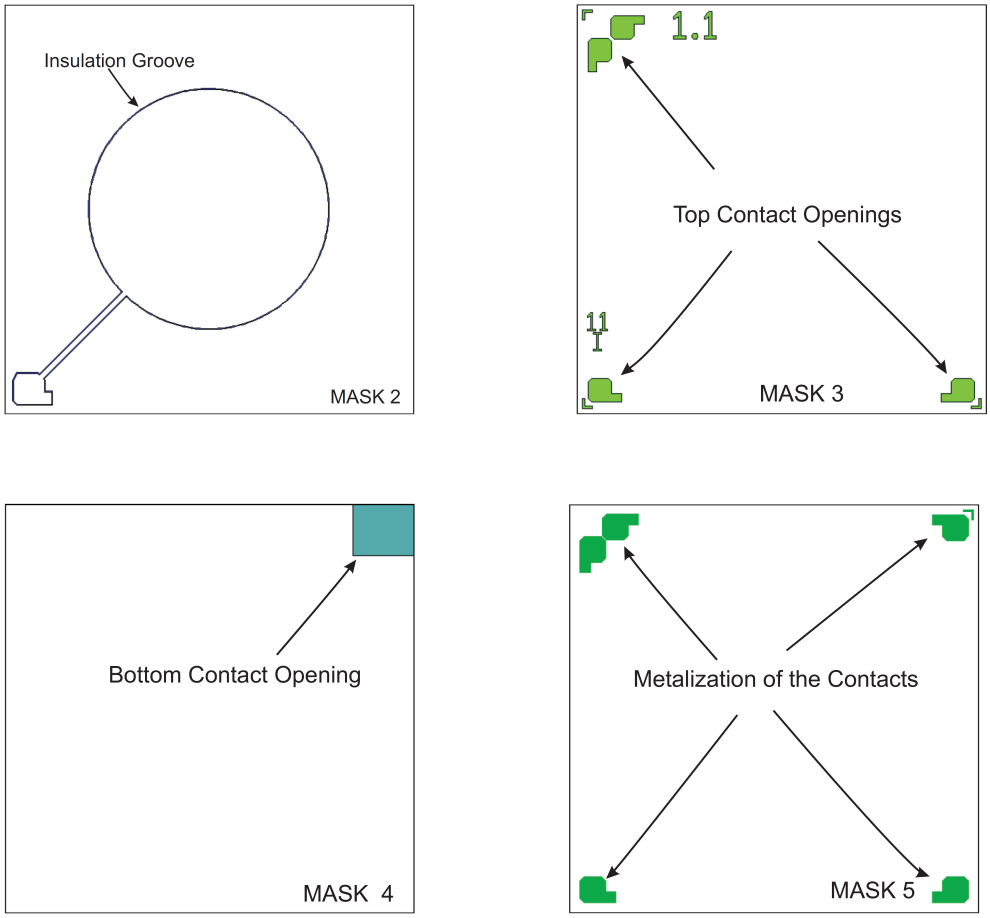

Figure 3.6: Mask set of the original TMCPS, the first mask has been previously shown in Fig. 3.1 and is not reported again. It consist of an hexagonal honeycomb structure and a contact that are etched in the oxide grown on the DSP wafer. The other four masks are here shown (on a single die level), mask 2 is used to etch the insulation groove in the DL of the SOI, mask 3 and 4 are used to open top and bottom contacts respectively and mask 5 is used to remove the metal everywhere except in the contact reagion.

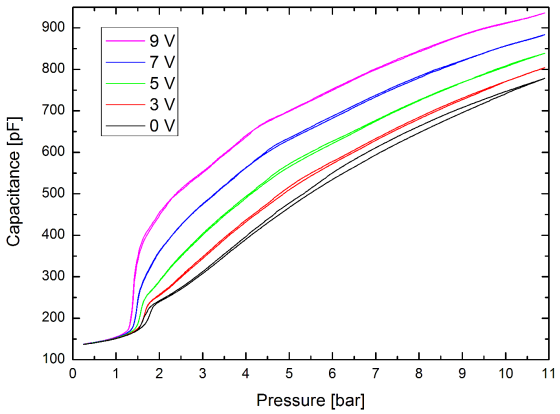

Figure 3.7: Capacitance measured as a function of pressure for different bias voltages. As the voltage is increased, the hysteresis, as well as the linearity of the device in the touch mode area, are clearly reduced.

3.2.2 Hysteresis reduction

The hysteresis observed in TMCPS is attributed to adhesion forces between the membrane and the underlying substrate when these are in contact in touch mode operation. Thus, if the pressure is decreased the adhesion forces will tend to maintain the membrane in the position of higher pressure. This results in a higher capacitance for a decreasing pressure than for an increasing pressure in touch mode. The hysteresis can be reduced in different ways. One way is to include an extra process step during fabrication with the purpose of creating corrugations on the substrate in the membrane area, hereby minimizing the area of physical contact. Another way is to add an additional force that is larger than the adhesive force, such that the adhesion forces are reduced in relative magnitude.

Therefore, as an experiment an electrostatic force is applied to the sensor by imposing a DC bias between the plates. The effect of this is seen in Fig. 3.7, where the capacitance as function of pressure is plotted for different bias voltages. It is clearly shown how the hysteresis is reduced by the addition of an electrostatic force. The application of a DC bias however changes the output characteristic of the sensor. Due to the additional force a higher capacitance is achieved and the sensor enters touch mode at a lower pressure than without a DC bias. Furthermore, this method clearly affects the linearity of the device in touch mode operations.

Another way to approach the hysteresis problem, whether due to stiction forces or to poor quality of the insulating layer, is a reduction in the contact area between the top electrode and the insulation layer. Two different type of corrugation can serve this purpose, a definite one obtained with a lithographic step or a random corrugated surface obtained without the use of a mask. Even though the first option requires an extra mask step, it must be preferred if the process involve fusion bonding of two wafers in order to keep a sufficiently smooth bonding surface. Furthermore, in the first case, the lithography limits when defining structures in a cavity (i.e. with a proximity distance between the mask and the photoresist) must be considered. Experimental results has proven to be extremely difficult to approach the theoretical critical dimension, CD, given by [55]

$$CD \equiv \frac{2}{3}\sqrt{\lambda\left(d - \frac{t_r}{2}\right)}, \tag{3.2}$$

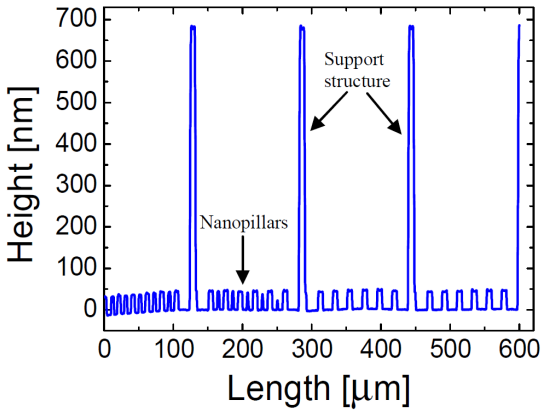

Figure 3.8: Profilometer measurement of the pillar structure etched on the bottom of the cavities. The 50 nanometer pillars are measured inside the walls of the honeycomb structure which height is roughly 650 nm.

where λ is the wavelength of the source used, d is the proximity distance between the mask and the photoresist and t_r is the photoresist thickness.

In our case, with a photoresist thickness of 1.5 μm, a wavelength of 365 nm and a proximity distance equal to the gap distance between the two electrodes (650 nm) the theoretical limit was calculated to be 1.3 μm. However, to achieve good results pillars of 6 μm radius and around 50 nm height where fabricated with an isotropic SF6/O2 plasma etch (STS ICP Advanced Silicon Etcher). Fig. 3.8 shows a contact profilometer (Dektak8) measurement of the nanopillars structure fabricated on the bottom of a 650 nm cavity etched in SiO_2. A SEM image of a TMCPS fabricated with the pillar structure and diced afterwards is shown in Fig. 3.9. This method affects the sensitivity of the device in touch mode as a direct effect of the contact area reduction but on the other hand it does not degrade its linearity. The sensors with the nanopillars structure have been compared with some that have been fabricated without this feature. Fig. 3.10 shows the comparison between the hysteresis, κ, of the two designs which has been calculated as follows:

$$\kappa \equiv \frac{C_{down}(p) - C_{up}(p)}{C_{up}(p)} \cdot 100, \tag{3.3}$$

where C_{down} and C_{up} are the capactive output signals at a pressure p, measured on the decreasing pressure curve (from 10.5 bar to 250 mbar) and on the increasing pressure curve (from 250 mbar to 10.5 bar) respectively. The new sensors showed a reduction in hysteresis by a factor of 3 in touch mode and no peak around touch point pressure at an expense of an increase of fabrication complexity given by an extra lithographic step.

In the next section a simplified process that employ one mask less than the original process is presented together with a coating solution adopted which requires only a different design of the last mask. Often, in the MEMS field, device performances can be slightly compromised for a simpler process and therefore an higher yield (i.e. lower production costs).

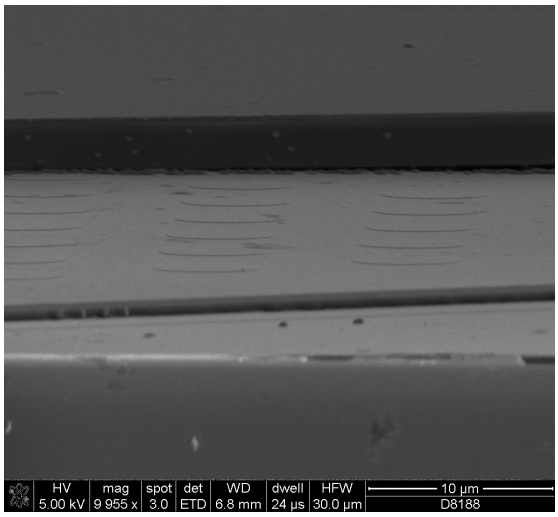

Figure 3.9: A SEM image of a fabricated chip. Part of the top plate has been removed in order to see the underlying pillar structure.

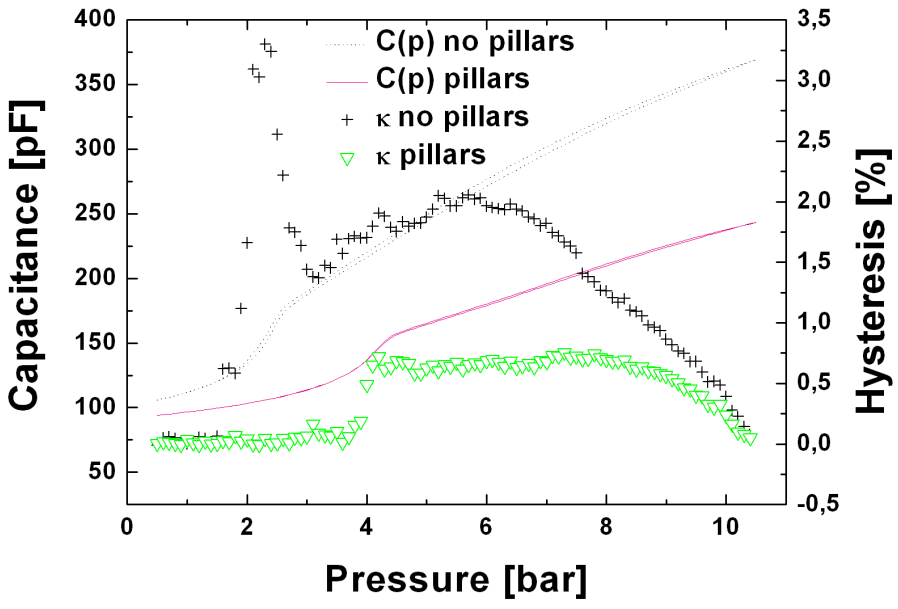

Figure 3.10: Hysteresis, comparison between two chips of the same batch, one of them fabricated with the pillar structure, the other without. Capacitances curves have been added to show qualitatively the hysteresis of the sensors.

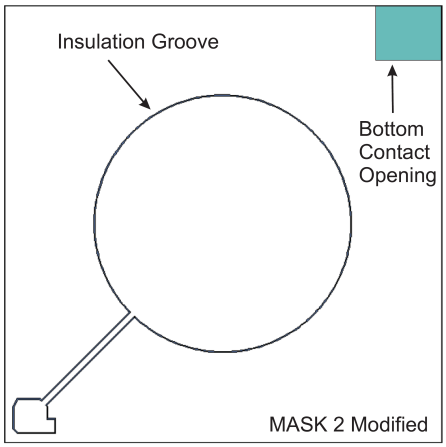

Figure 3.11: Modified mask 2. In the new process it also contains the features of mask 4.

3.2.3 The 4-masks process and gold coating

In this project a reduction to a 4 masks process was achieved by adding the rectangular feature in mask 4 (see Fig. 3.6) to mask 2 and using mask 5 of the original process to open top and bottom contacts at the same time (i.e. just removing the box from the contact area). In this way the old mask 4 can be removed from the process. The new mask 2 is shown in Fig. 3.11, while the new mask 4 which contains the coating is described later in this section. Adding a big feature to mask 2 is not as trivial as it may seem since the insulation groove has a much smaller feature size compared to the bottom contact opening in the DL (see Fig. 3.11). Therefore microloading effects (i.e. etch rate depends on etchable area on a chip or feature scale) happen and their relevance must be evaluated. Fig. 3.12 shows on the left the etch depth as a function of the number of etch cycles measured in the insulation groove while on the right the same measurement is performed for the bottom contact. From these graphs around 1 μm/min difference in the etch rates (6.1 μm/min for the groove and 7.2 μm/min for the contact) is found.

Using a SOI wafer with 2 μm DL and given a Si:SiO_2 selectivity of 80:1 for the DRIE, microloading results not to be a problem. None the less, after the handle wafer is removed a suspended SiO_2 membrane of 600x500 μm and 1 μm thick remains exposed. When the contacts are opened this membrane cracks leaving the support structure exposed to the BHF. This causes a short circuit between the coating and the bottom contact which is clearly visible in the SEM image of Fig. 3.13. As it is shown later in this section, a different mask has therefore to be design in order to define the coating considering this issue. All the process steps performed after the etch of the insulation groove with the new mask 2 remain the same until top and bottom contacts have to be opened.

In order to use mask 5 of the original process to etch the box of the SOI (therefore avoiding to order a new mask), a mask reversal process is needed. It consist of a bake of 2 min at 120°C followed by a long flood exposure (30 s) done after mask 5 has been transfer on the photoresist with the common alignment and exposure process. This process is standard and does not give particular concern. After the contacts have been open the only lithographic step left is their metalization and at the same time the coating material can be deposited and patterned. A new mask has been designed for this purpose, Fig. 3.14 shows two verision of this mask. The

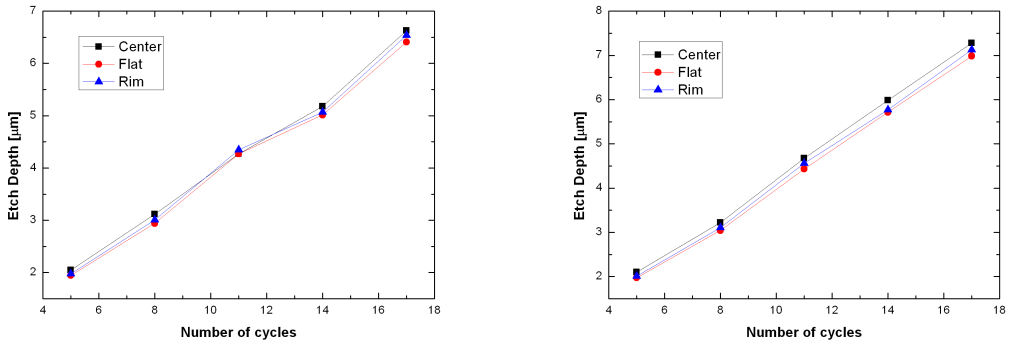

Figure 3.12: Insulation groove (left) and contact hole (right) etch depths measured as a function of the etch cycles. The measurements have been performed with a stylus profilometer on three different positions on the wafer, in the center, near the main flat and close to the wafer edge. The etch rate found is homogeneous, around 6.1 μm/min for the groove and 7.2 μm/min for the contact.

first design of this mask has not taken into account the possibility of cracking of the box oxide therefore the coating contacts the bottom plate in top left corner corner of the bottom contact opening (see Fig. 3.13). Furthermore, with the first design, there is a risk of removing or melting part of the gold at the chip borders while dicing the wafer. From Fig. 3.14 it is clear that, in the second metal etch design, solves the short circuit problems just discussed. The final optimized process flow for TMCPS with gold coating has been fully analyzed, it consist of four masks, namely:

1. Mask 1: oxide etch with different support structure radii.
2. Mask 2: isolation groove and bottom contact etch.
3. Mask 3: contacts opening (mask 5 of the original process is used).
4. Mask 4: metal etch (coating and contacts).

A detailed table of this process flow together with all the process parameters is given in Appendix B. The critical steps, namely fusion bonding and handle removal, remained the same and especially the first one will pose a serious challenge for the technology transfer between DTU and Grundfos as it is explained in the next section.

3.3 Technology transfer

The last topic of this chapter is dedicated to some considerations about technology transfer between DTU Danchip and Grundfos.The ultimate goal of the TMCPS project is in fact to start a production of this kind of sensors in Grundfos Direct Sensors' cleanroom. In order to do so the possibility of performing there the last process described, which is also the simplest, must be investigated. Currently these facilities are producing piezoresistive pressure sensor as it was pointed out in the introduction of this dissertation. These transducers have ion implanted

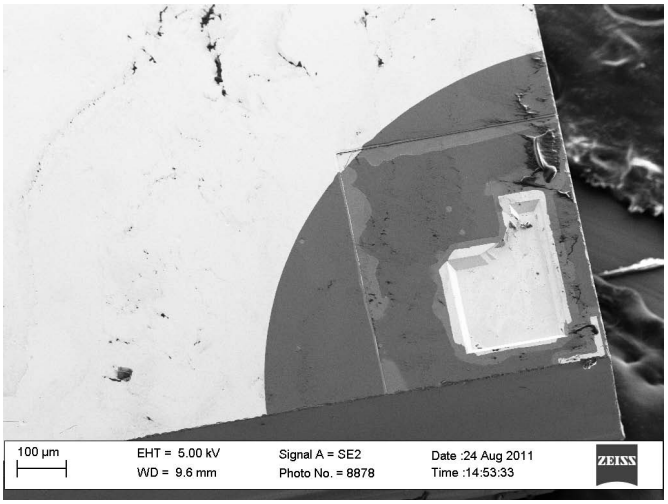

Figure 3.13: SEM image of the bottom contact of a device fabricated with the first coating design. The coating is electrically connected to the bottom plate in the top left corner of the rectangle etched with mask 2 in the DL. This happens because the box is completely removed during the contact opening step.

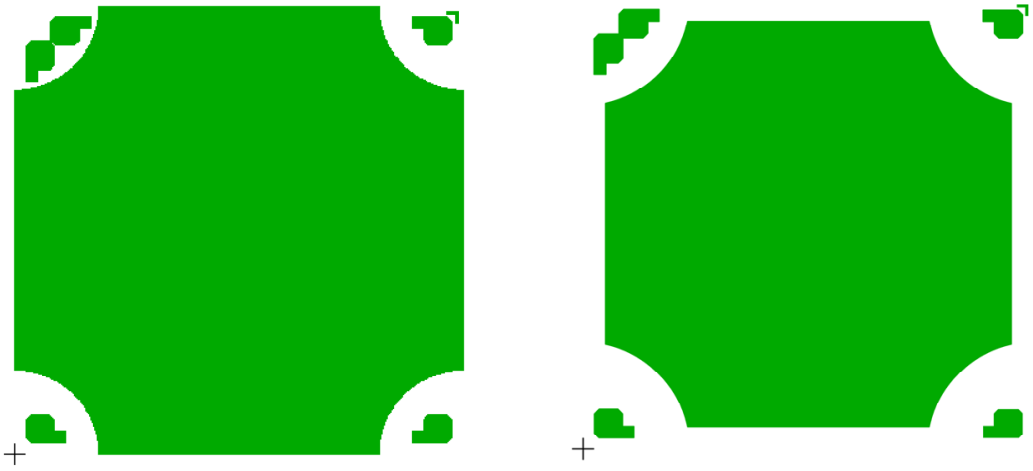

Figure 3.14: First (left) and second (right) design of the new mask for metal etching. In the second design the distance between the contacts and the coating is increased, furthermore a clearance between two adjacent dies is implemented by means of a smaller coating area.

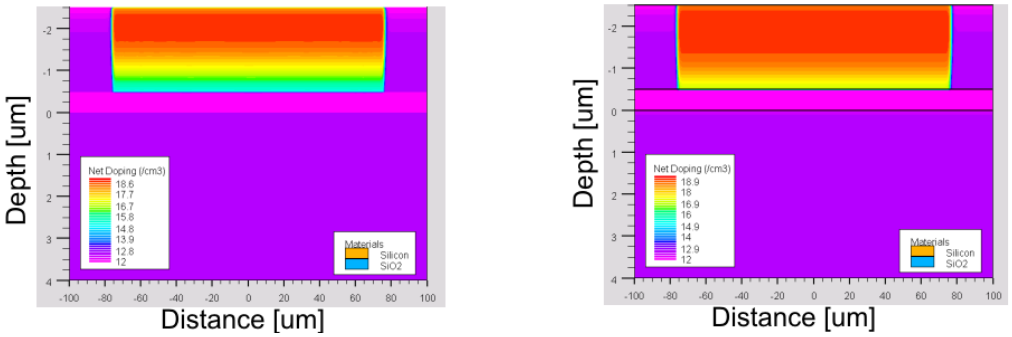

Figure 3.15: Simulation results of phoshorus (left) and boron (right) ion implantation on an SOI wafer. As expected, p-type doping results in deeper junction provided the same dose and energy. Grundfos standard high dose parameters have been used for this simulation.

piezoresitors in a silicon wafer which is then etched on the back side using TMAH to release a 20 μm thick membrane. The coating process concludes the fabrication. The company outsources ion implantation, a process too costly to be performed in house, therefore the doping of the SOI and DSP wafers done to obtain the two capacitor plates has to be outsourced as well. A simulation of the high dose ion implantation process ($2.45 \cdot 10^{15}$ ions/cm^2 at an energy of 150 keV) that is used from Grundfos has been implemented with a commercial software (SUPREM). A 1 μm thick aluminum mask with a 150 μm opening is proposed with the purpose of doping only the active area of the device. A 0.1 μm oxide is deposited before applying the mask to preserve the surface integrity. The results of the simulations are shown in Fig. 3.15 where it can be noticed that boron gives a deeper profile than phosphorus. Furthermore, boron should be preferred since it gives a better surface integrity. While doping seems not to be a problem for the technology transfer process, fusion bonding is. Currently there is no bonding machine at Grundfos therefore a solution considered was to perform only the bonding step at Danchip. Unfortunately, the results of different particles counting scans, performed at Grundufos after new wafers were put in contact with the bonding chuck and the aligner tray of the EVG machines, ruled out this possibility. To avoid doubts that the wafers were contaminated during transportation a first test performed was to carry some clean wafers from Grundfos to Danchip and let them stay there in an open wafer box for a day. Then, these wafers were taken back to Grundfos and measured. No evidence of contamination was found. A new scan was done after the bonding chuck and the aligner tray were cleaned with acetone and in the plasma asher, then blew with the nitrogen gun and not used for 12 hours hoping that the High-Efficiency Particulate Air (HEPA) would have removed a big number of particles. Fig. 3.16 illustrates the fact that even after these different cleaning procedures the bonding chuck still contaminates the wafer while the aligner tray results clean. If fusion bonding has to be performed in Danchip a dedicate set of tools is therefore suggested.

3.4 Conclusion

In this chapter the fabrication of TMCPS has been thoroughly described. Firstly a design which results in sensors with different touch point pressure has been described. Then, starting from the original process flow, many different modifications have been introduced. Successful so-

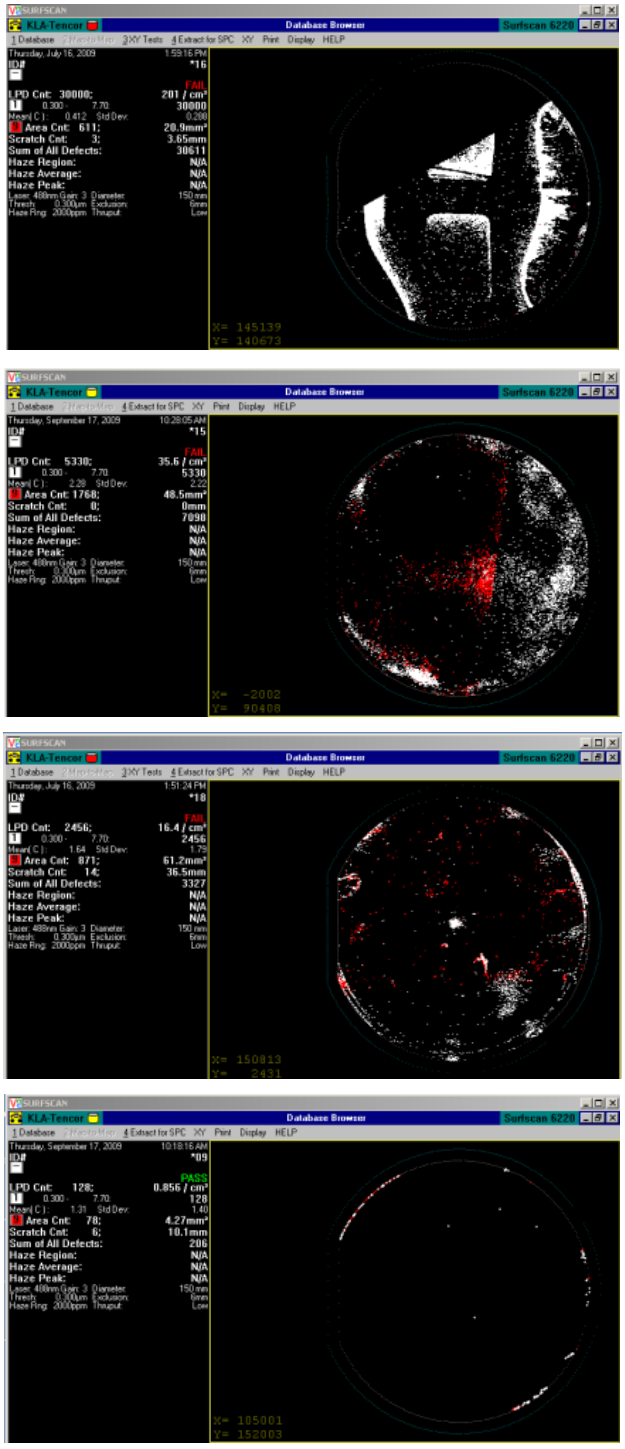

Figure 3.16: Particles count on wafers that have been put in contact with the bonding chuck or the aligner tray of the EVG machines in Danchip. From the top, the first image shows the counts on wafer that has been in contact with a dirty chuck (more that 30.000 particles), the second indicates the counts after cleaning of the chuck (still 5000 particles), the third and fourth refers to the tray, where much better results are obtained (only around 100 particles after the cleaning).

lutions to reduce hysteresis, an intrinsic problem in TMCPS, have been commented in Section 3.2.2. Furthermore, the process recipe has been reduced from 5 lithographic steps to 4, including the coating. Finally, a study on the feasibility of a technology transfer between Danchip and Grundfos facilities has been presented. More than 4 different batches of TMCPS devices have been completed in this project, each one of them consisting of around 200 hours of effective cleanroom time plus many hours of test runs due to machines upgrade or different cleanroom/materials conditions. A detailed description of the processes optimization done in this work goes by far out of the scopes of this dissertation where only the most important fabrication results are presented. In the next chapter multiple solutions to electronically interface the TMCPS here depicted, are discussed.

Chapter 4

Interfacing circuit for capacitive microsensors

In this chapter, different solutions for interfacing a touch mode capacitive pressure sensor are presented. The results described in the previous chapters, where this type of sensor is modeled and its fabrication process is depicted, are now used to develop an electrical equivalent circuit. Capacitive sensing in fact always threat the sensing element as an ideal capacitor and validity of this assumption is checked also in this project.

Three circuit that have the potential to fulfill Grundfos requirement are presented namely, the switch capacitor interface, the charge-discharge circuit and the AC bridge circuit. The first solution proposed is the most complicated and therefore its analysis and simulation is firstly divided into three main blocks, the control signals block that generates the clocks for the switches in this circuit, the sample and hold block that keeps memory of the sensors charge during conversion time and the differential integrator block that subtract the offset capacitance (or steady state capacitance) from the sampled signal and converts it into a digital signal. Furthermore, the operations performed by the last two blocks are divided in four steps that cover all possible circuit configurations.

The charge-discharge circuit is described right after to show a much simpler interfacing method that has only one minor drawback as the output is analog, on the other side, the circuit has many advantages such as size and complexity among others. Finally the most studied method in this project, the AC bridge circuit, is presented. Also in this case, the analysis is split in blocks; the reason for this choice is not the complexity but rather a need for studying different component solutions and layout options. All these circuits have been simulated with the aid of a commercial software (B2SPICE) and their fabrication and characterization (presented in Chapter 5) closely follow the theoretical and numerical results here shown.

4.1 Sensor electrical characteristics

The main and most important assumption made in order to use, in good conscience, signal conditioning circuits for capacitive transducers to interface MEMS capacitive sensors is that the devices considered can be threated almost as ideal capacitors (i.e. the real part of their impedance must be negligible). From the electrical point of view, it is possible to identify three different version of the TMCPS:

- the first device where the bottom plate was contacted from the back side (Fig. 4.1)

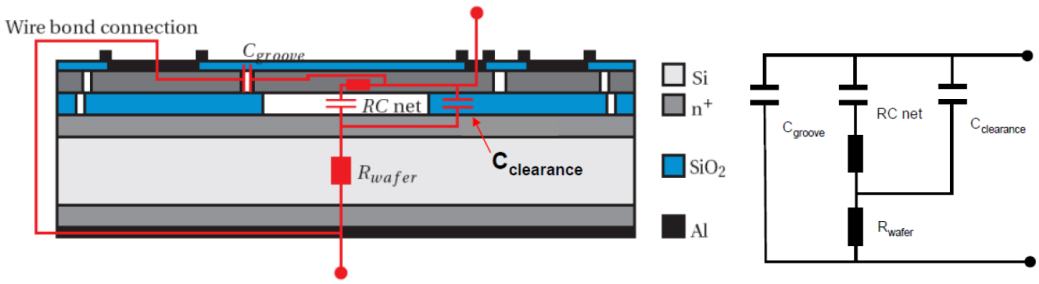

Figure 4.1: Cross section of the first TMCPS developed (on the left) and its electrical equivalent circuit (on the right). Only in this design a contact is placed on the bottom side of the wafer, thus the wafer resistance is considered in the equivalent circuit.

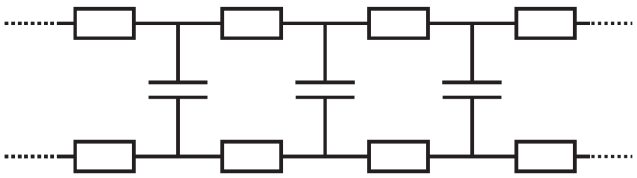

Figure 4.2: Equivalent circuit of the capacitor plates. The capacitors each represent a small fraction of the entire capacitor system whereas the resistors represent the resistance in the highly doped silicon that make up the capacitor electrodes.

- the TMCPS without coating (Fig. 4.3)
- the TMCPS with coating (Fig. 4.4)

Only the first of the three versions has a different resistive contribution given from the wafer resistance which can be calculated from

$$R_{wafer} = \rho \frac{t_{wafer}}{A} \tag{4.1}$$

where ρ is the resistivity of the wafer, t_{wafer} is the thickness of the wafer and A is the effective conducting area. This area is difficult to calculate but is, in principle, equal to the die area which is defined from Grundfos specifications to be 16 mm^2. The wafer used as substrate is a 500 μm thick n-type wafer with a resistivity of 1-20 ohm cm. Thus the wafer resistance is expected to be approximately 6.25Ω in the worst case (high resistivity). This is an insignificant contribution to the total impedance (which is in the MΩ range at low frequency) and it will be ignored in the following. The other resistive contribution is given from the RC network consisting of the parallel contribution of the capacitor cells that form the honeycomb structure and of the distributed resistance of the plates. An equivalent circuit of this network is seen in 4.2. Each capacitor in this diagram represents a small fraction of the membrane and the resistors represent the resistance in the highly doped silicon that make up the capacitor electrodes. This contribution has previously been estimated with the following formula [56]:

$$R_{plates} = \frac{1}{8\pi} R_{\square} \tag{4.2}$$

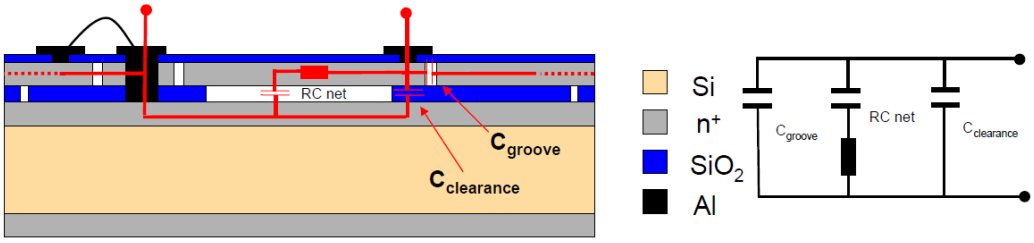

Figure 4.3: Cross section of the 4-mask TMCPS die (on the left) and its electrical equivalent circuit (on the right). In this design both contacts are placed on the top side of the wafer, thus the wafer resistance can be discarded from the equivalent circuit.

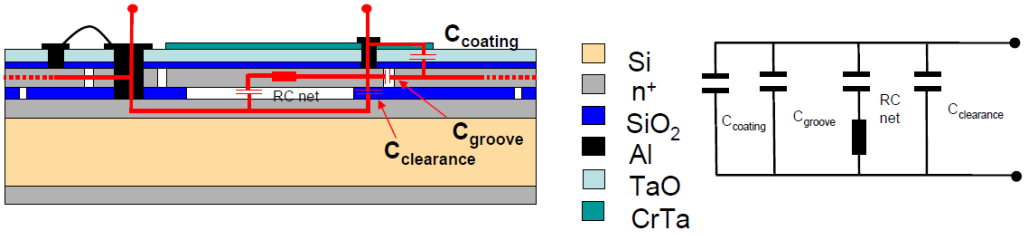

Figure 4.4: Cross section of the TMCPS with coating (on the left) and its electrical equivalent circuit (on the right). Only in this design a coating is placed on the box of the SOI wafer and overlaps both the active area and part of the area outside the groove, thus an extra capacitive contribution is considered in the equivalent circuit.

where $R_{\square}$ is the sheet resistance. In this work, the sheet resistance has been measured each time a new batch of sensors was made; it never exceeded 10 Ω/□. Therefore the maximum resistive contribution given from the plates is around 0.4 Ω, again a negligible value compared to the impedance of the sensor at low frequency.

Higher interest must be given to the different parasitic capacitances that are intrinsically arising from the geometry proposed. The active area is separated from the rest of the device layer thanks to the isolation groove and connected to the bottom plate by means of wire bonding, this results in great reduction of the parasitic capacitance otherwise being:

$$C_{parasitic} = \varepsilon_0 \varepsilon_r \frac{A_{die} - A_{active}}{g} = 741pF \tag{4.3}$$

where ε_0 and ε_r are the permittivity of vacuum and SiO_2 respectively, A_{die} and A_{active} are the die and the active areas and g is the gap distance. The estimated value of 741pF (10 times larger than the sensor capacitance which is around 60pf as it has been shown in Chapter 2) ,motivate the necessity of the isolation groove. From Fig. 4.1, Fig. 4.3 and Fig. 4.4 it is possible to notice that there are other two undesired capacitive contributions common to all the designs namely, the capacitance given from the insulation groove, C_{groove}, and the one, $C_{clearance}$, given from the sum of all the clearance left around the groove plus the oxide pillars which form the support structure. Fig. 4.5 illustrate all the different parts that are taken into account to evaluate $C_{clearance}$:

1. 20 μm wide ring between the groove and the support structure (C_1)

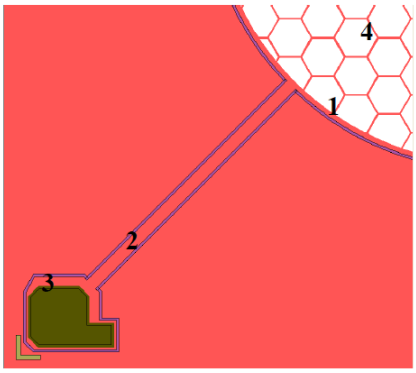

Figure 4.5: Parasitic capacitances arising from different contributions. The ring around the support structure (1) together with the contact finger (2), the extra contact area (3) and the pillars forming the support structure (4) constitute what is called the clearance capacitance.

2. contact finger (C_2)
3. contact area (C_3)
4. oxide pillars (C_4)

All the capacitances mentioned are calculated with the simple parallel plate capacitance formula where the distance between the plates is either the gap distance, in the case of $C_{clearance}$, or the DL thickness, for C_{groove}. The last model considered has a major difference with the previous ones which is a conductive coating deposited on top of the box of the SOI. The coating will introduce an offset term similar to the parasitic just discussed therefore in parallel with the sensor capacitance. In Fig. 4.4 the coating is connected to the top plate, this solution make sense assuming that the majority of the coated area lies on top of the active area. To evaluate the amount of area of the die which is exposed to the corrosive media (and therefore must be coated) but is not pressure sensitive, some packaging parameters must be discussed. Grundfos packaging solution makes use of O-ring clamping as a hermetic sealing for their MEMS pressure sensors (see Fig. 4.6). The top O-ring size and its contact area under squeezing are the factors that influences the minimum coating dimension. According to [57], who has studied this problem for Grundfos piezoresistive sensors, the O-ring is compressed to around 20% by the force induced from the package. This compression results in a O-ring contact area of around 1 mm. Therefore, in principe, a design with a circular coating of radius 1.3 mm could be sufficent to proctect the silicon die. The circular coating is the solution which minimize the parasitic given from the coating area which does not overlap the active area. None the less, in the final design, a more conservative solution is implemented. The coating area is maximized (as shown in the previous chapter) in order to make sure that the sensor can be exposed without risks to the aggressive media even if the die thickness and therefore the O-ring contact area are smaller. The final design poses higher demands on the electronic conditiong circuit as it is obivious from table 4.1 where $C_{coating}$ has two values that idicate the parasitic given the circular coating just discussed and the one estimated for the actual design respectively. Table 4.1 summarizes the discussion on the electrical equivalent circuits for all the designs of TMCPS fabricated in this and previous works. In the next section different possibilities for signal conditioning of these

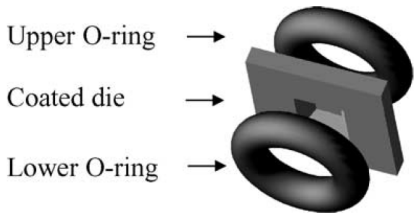

Figure 4.6: O-ring clamping as a hermetic sealing solution adopted by Grundfos. In the case of piezoresistive pressure sensors a study of the stress induced by the sealing is necessary, for CPS this is factor is of much less important compared to the top O-ring contact area under squeezing which influences the minimum coating dimension.

Electrical parameter	First design	TMCPS without coating	TMCPS with coating
R_{wafer}	<6.25 Ω	N.A.	N.A.
$R_{distributed}$	<0.4 Ω	<0.4 Ω	<0.4 Ω
C_{active}	67 pF	67 pF	67 pF
$C_{clearance}$	61 pF	61 pF	61 pF
C_{groove}	6.5 fF	6.5 fF	6.5 fF
$C_{coating}$	N.A.	N.A.	15 pF to 174 pF

Table 4.1: Electrical parameters of the TMCPS. It can be noticed that the contribution from the groove capacitance can be neglected while the contribution of the coating can be much reduced with proper design.

kind of devices are discussed, some of them are implemented in this work and their suitability for Grundfos application is investigated.

4.2 Interfacing circuits for capacitive sensors

Numerous applications of MEMS capacitive sensing such as proximity sensing, acceleration and liquid level measurements are already strongly present on the market [30, 31]. Pressure is not among these ones (if we exclude MEMS microphones) even though a big number of fabrication techniques have been reported [28,29,53,54,58]. This is due to the fact that a piezoresistive sensor is generally easier to fabricate, can be interfaced with a simpler and cheaper circuit and has a more linear characteristic.

The development of capacitive sensors have been strongly influenced by these factors and, in literature, many articles report complex conditioning circuit that can be used to measure very small change in capacitance, even of the order of Attofarads [26, 59]. Among these Jones and Richards [23] have reported a circuit which has a resolution of 0.1 fF on a full scale signal of 50pF with an output voltage sensitivity of 30 mV/fF. Huang et al. [25] has reviewed four different methods to measure small capacitance changes of the order of 0.1 fF where the full scale signal is around 10 pF, suggesting a choice dependent on the measurement frequency. In general these techniques can be implemented with purely analog circuits as opposed to switched capacitor techniques [27] and capacitance-to-phase angle techniques [60] where a digital con-

trol circuit and ADCs (analog to digital converters) are needed. The need for a simple and sensitive front end circuit which converts the capacitive signal of a MEMS to a DC voltage, readable with a multimeter or a data logger, is therefore justified when a capacitive sensor has to be tested without the use of a bulky measurement instrument such as an impedance analyzer or a capacitance meter.

The main requirements for the interfacing circuit are therefore a simple layout which can easily be reproduced with discrete components and interface, an adjustable dynamic range, inherent immunity to stray capacitances and high sensitivity. Furthermore, Grundfos has pointed out a set of criteria that should be considered when aiming at an industrial product:

- Design for mass production, no variable capacitors, no potentiometers, no linearization, calibration or adjustments.
- Low cost.
- Low power. (I<<4 mA).
- Fast settling time of circuit during power up (Must be able to run in "burst mode").
- Small size - The circuit must be able to fit the OEM sensor PCB mounted with 4 pin connector as in current sensors (see Fig. 4.7).
- Good measurement accuracy.
- Low long term drift. The final product is intended to be running for up to 10 years.
- Robust with respect to the surrounding environment: immunity to electro-magnetic (EM) interference, low sensitivity towards temperature (the final product is intended to run with media temperatures between 0°C and 100°C).
- The circuit can have either analog or a digital output.

When choosing the capacitive pick off method most of these demands have been accommodated and in particular, the circuits considered do not have variable components or need for clibration/adjustments, have a good accuracy, can have both analog or digital output and two out of three of them meet the size constraints. Moreover, even if not optimize, the other criteria such as costs, temperature sensitivity and power consumption have been addressed. In this work a total of three systems have been designed, simulated, implemented and tested with both variable capacitors of different sizes (dummy sensors) and TMCPS which fabrication is described in Chapter 3, the first of which, the switch capacitor concept, is described in the following section.

4.3 Switched capacitor interface for TMCPS

The switched capacitor interface that is presented in this section is inspired from the work published from [11]. It consists of a sample and hold stage which sense the charge of the sensor and keep its output value until it is compared with a reference charge in the second stage of this circuit, a differential integrator. This solution gives a digital output (a series of peaks) which is proportional to the transducer capacitance. A block diagram of the switched capacitor configuration is shown in Fig. 4.8. $C(x)$ denotes the capacitive microsensor, S/H the Sample

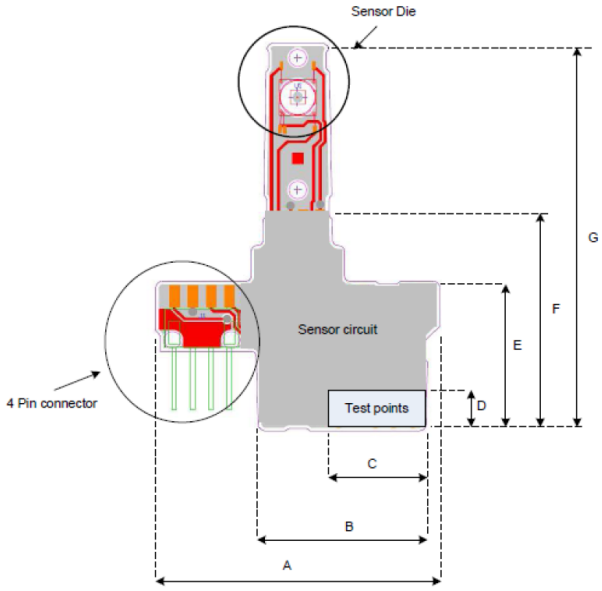

A	31.00 mm
B	18.30 mm
C	11.00 mm
D	4.50 mm
E	16.60 mm
F	25.00 mm
G	43.90 mm

Figure 4.7: Grundfos OEM sensor PCB. It can be noticed that the total available area for the signal conditioning electronics is around 303.8 mm^2 (i.e. BxE).

and Hold, *DI* the Differential Integrator, *CP* the Comparator. $Q(x)$ is the charge sensed by the S/H and Q_r is the reference charge. The output from CP is a digital value which is stored by a counter, *CNT*. In this project the counter has not be added in the final layout being it not necessary for the proof of concept requested. The switched capacitor interface is by far the most complex system designed in this work therefore its analysis, simulation and fabrication have been split in 3 main blocks:

1. the control signals generation
2. the sample and hold circuit
3. the differential integrator and comparator

The single blocks are described in the following sections where their working principle and simulation are illustrated.

4.3.1 Control signals

The operation principle of the switch capacitor interface is completely defined from four signals which control all the switches in the circuit. These signal are two clocks that regulates the frequency of the single steps during a full conversion cycle and a sample and a hold that define how long a conversion cycle takes, thus defining the range of capacitance measurable. To prevent unwanted voltage spikes resulting from untimely switch conditions and overlapping, the signals have been designed as shown in Fig. 4.9. So non-overlapping clocks as well as non-overlapping rising/falling edges between clocks and sample and hold signals have been implemented with the aid of delay lines. Fig. 4.10 shows a block diagram of the circuit designed to generate the

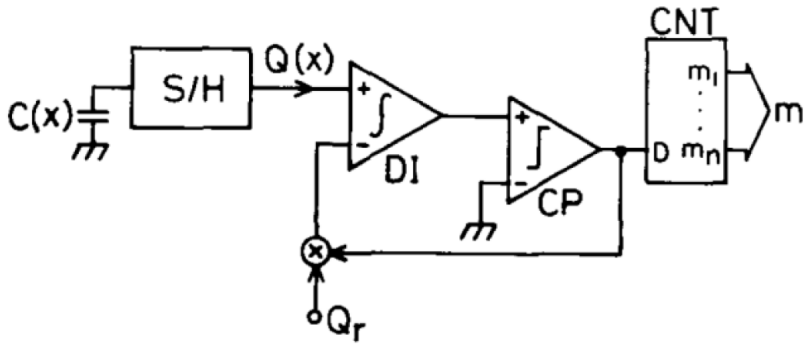

Figure 4.8: SCI block diagram. $C(x)$ denotes the capacitive sensor, S/H the Sample and Hold circuit, *DI* the Differential Integrator, *CP* the Comparator, *CNT* the counter, Q(x) the charge sensed by the S/H and Q_r the reference charge. Figure acquired from [11].

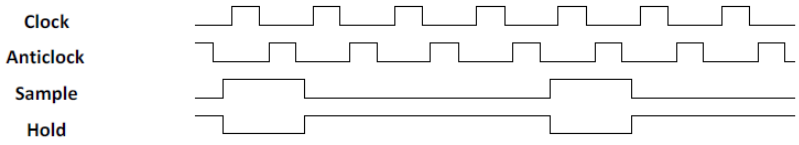

Figure 4.9: Control signals for the switches of the SCI. The number of clock cycles during the hold time here depicted is lower than in the actual interface in order to illustrate the non-overlapping nature of the signals.

control signals which consist of a common 555 timer, two delay lines, a 8 bit binary counter, a D-type flip flop and a set of AND and NOT gates. The counter decides the length of the hold time which has been chosen to be 52 periods in order to allow enough dynamic range for the measurement. These is explained by the fact that the change in capacitance is a functions of the number of output peaks generated during the hold time as it is shown in Section 4.3.3. The clock frequency chosen for this circuit is subjected to a trade off between two factors, a low frequency minimizes electromagnetic interferences and cross talk between control signals but it may not give enough time to fully charge the capacitors in the system. The biggest capacitor of the system (3.9 nF) has set the lower limit for the frequency. It charges/discharges through a switch that has a maximum ON resistance of 20 Ω thus giving a time constant:

$$\tau = R_{ON} C_{max} = 78ns \tag{4.4}$$

where R_{ON} is the maximum ON resistance of the chosen switch and C_{max} is the biggest capacitor in the circuit. A frequency of 10 kHz gives therefore plenty of time to fully charge (i.e. T=50 μs$>>5\tau$) the capacitors in the circuit and is below the limit of 50 kHz given in order to completely neglect interferences. The control signal circuit has been simulated with a commercial software (B2Spice) and the results have shown the desired non-overlapping nature of the clock signals. These signals drive all the switches used in the sample and hold as well as in the differential integrator block.

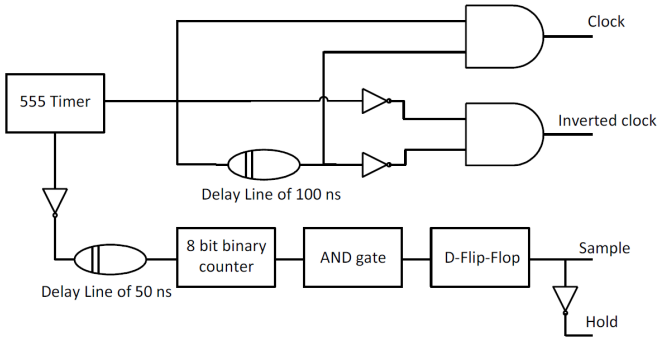

Figure 4.10: Control signals block diagram. A total of 5 AND gate is needed since the 8-bit binary counter is substituted with two 4-bit counters due to availability of these components.

4.3.2 Sample and hold

The S/H circuit is designed to sample the charge on the sensor and hold its value until the DI has converted it into a digital signal. The S/H circuit is shown in Fig. 4.11 and consists of a voltage reference V_r, the capacitive sensor $C(x)$, the hold capacitor C_h, the sample capacitor C_s, and the compensation capacitor C_p. Furthermore there are 10 switches controlled by the four control signals mentioned in the previous section and an operational amplifier A_1. The sampling capacitor is charged to the same level as the sensor from the operational amplifier. This charge is held constant by the hold capacitor which closes the amplifier feedback loop.Finally the charge is transferred into the differential integrator that is described in the next section. During the hold time, the sampling capacitor is discharged into the differential integrator and charged again from the hold capacitor every clock period. The steps describing the 4 possible S/H configurations just discussed are shown in Fig. 4.12 where the status of each capacitor is pointed out. Moreover, it must be noticed that this circuit compensate for the offset voltage of the operational amplifier, since C_p is charged from the offset voltage in the first step and never discharged. The simulation of the S/H has been carried on together with the differential integrator as it is depicted in the next section.

4.3.3 Differential integrator

The DI quantizes the charge, $Q(x)$, held by the S/H stage, with respect to the reference charge, Q_r. The schematic of the DI together with CP is shown in Fig. 4.13, it consists of four capacitors, namely, the reference capacitor C_r, contribution capacitor C_c, the dump capacitor C_d, and output capacitor C_f, nine voltage controlled switches, two operational amplifiers (A_2 and $COMP$), a D-type flip flop and an AND logic gate. Furthermore, the output node of the S/H b, the voltage reference V_r and the contribution voltage V_c, are indicated on the schematic.

As in the previous section, operations are explained in four basic steps which are shown in Fig. 4.14. In the first two steps the DI disconnected from the S/H circuit. All the capacitors are discharged, except for C_d and C_f which are set to the value of the input offset voltage of A_2 in step one and two respectively. CP outputs a digital 1, which is then delayed by one period, and inverted by the Flip-Flop, therefore in these two steps $\Phi_c = 0$. In the third step and fourth steps, C_r is not charged, but the DI is connected to the S/H therefore the charge from the sampling

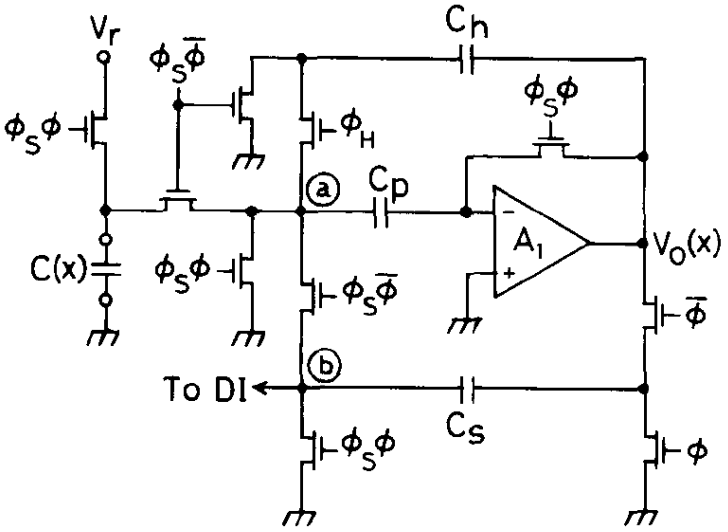

Figure 4.11: S/H block diagram. The charge in the sensor $C(x)$ is sampled in the capacitor C_s and its value is held by C_h for 52 clock periods.

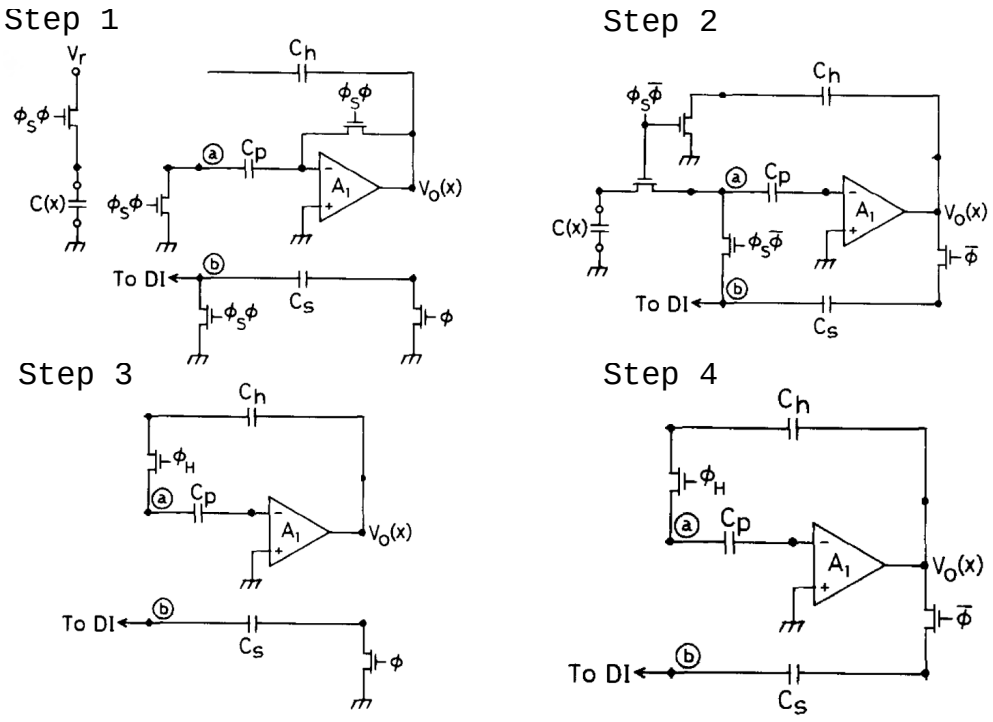

Figure 4.12: Possible switches configuration of the S/H circuit. C_p and $C(x)$ are charged in the first step while C_s and C_h are charged in the second step. In the 3 step C_s transfer its charge to the DI and in the fourth its charge is restored from C_h. Only in the third and fourth steps the S/H is connected to the DI.

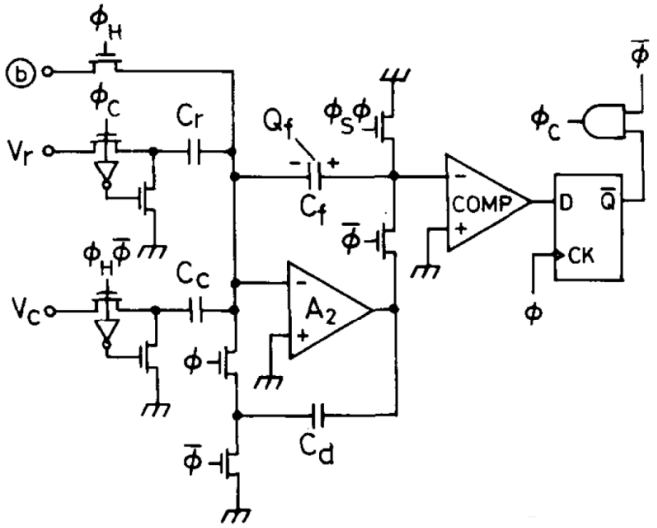

Figure 4.13: DI block diagram. The charge transferred from the S/H is is quantized by the charge C_r and at the same time the offset charge stored in C_c is subtracted from the measurement. The digital output is proportional to the number of clock cycles (2^n) times the ratio between the measured charge and the reference charge.

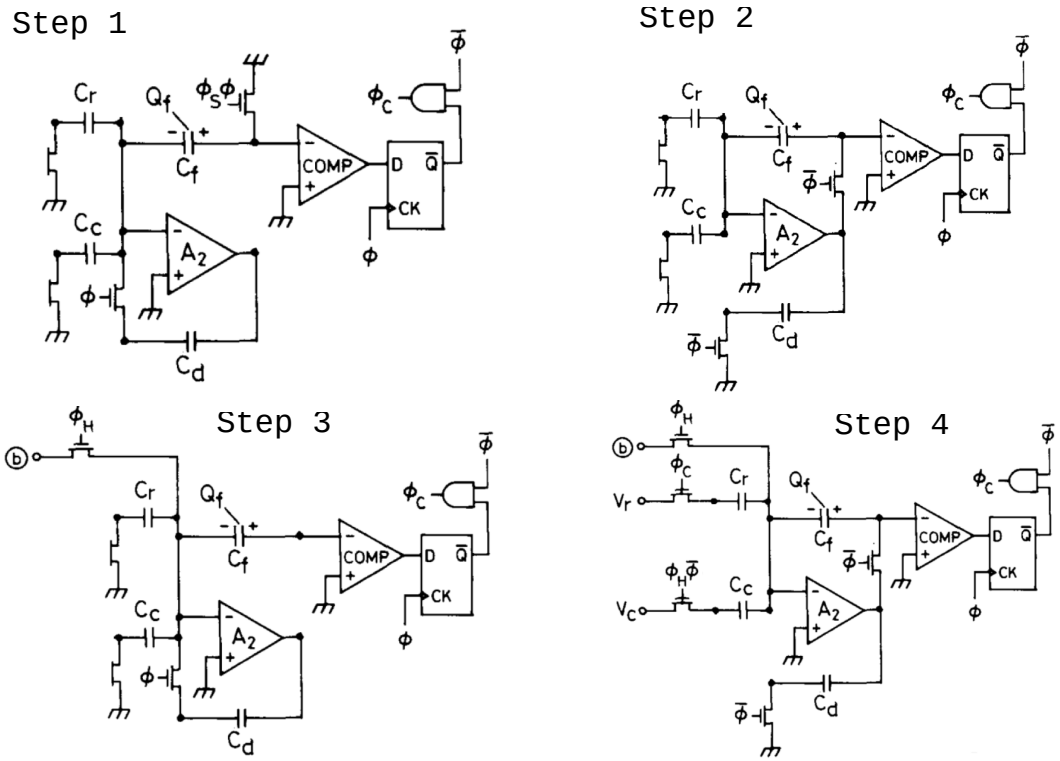

Figure 4.14: Possible switches configurations of the DI circuit. In the first step C_d is charged at the offset voltage of A_2 and in the second C_f is charged at the same value. The third and fourth steps are repeated during the hold time to perform the quantization of the sampled charge.

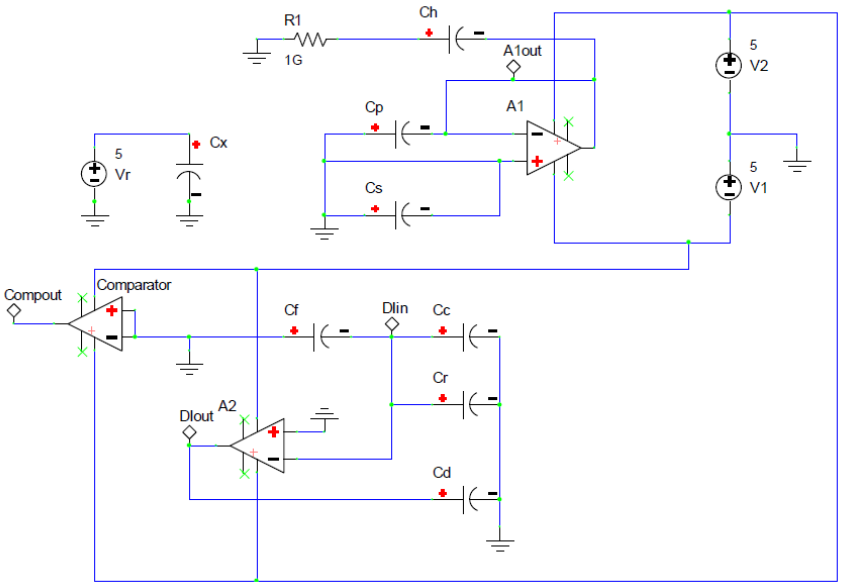

Figure 4.15: Schematic of the simulation of the SCI's first step. The switches are assumed to be either open or closed depending on their control signals, the S/H is in fact not connected to the DI in this step.

capacitor is first transfer into C_d (in step 3) and then into C_f (in step 4). At this point, if $Q_s > Q_c$ the charge in C_f is positive and the comparator saturates to the negative rail and in the following period the flip flop outputs a digital one which sets the voltage V_r on C_r. The quantization of the charge Q_s starts based on the charge balance principle applied on the inverting node of A_2. At this node the charge coming from the S/H is added to Q_r and Q_c and the result stored in C_f every clock cycle (during the hold time). The charge Q_c balances the zero pressure capacitance of the sensor according to:

$$C_0 V_r = C_c V_c \tag{4.5}$$

provided that a proper value for C_c is chosen, while C_r set the quantization step of the charge accumulated on $C(x)$ when pressure is applied, according to:

$$\Delta C(x) = C_r \frac{m}{2^n} \tag{4.6}$$

where m is the output signal (number of peaks, $\Phi_c = 1$) and 2^n is the number of periods. A full system simulation was not performed for the switch capacitor interface since its debug would have been a tedious and unnecessary work (the system has in fact 19 switches, 6 And gates, 2 D-type flip flops and many other components) but, after the control signals were designed, the S/H and DI interface were simulated step by step (as shown in Fig.4.12 and 4.14) forcing the proper initial conditions (voltages on the capacitors) and switch state. Fig. 4.15 shows the first of the four step discussed, from every step the voltages extracted from the simulation and reported in table 4.2.

There is perfect agreement between the data extracted from the simulations and the theoretical values:

$$V_{C_s} = Q_{C(x)}/C_s = 300[pC]/1[nF] = 300mV, \tag{4.7}$$

Capacitor	**Step 1** $\Phi = 1 \wedge \Phi_s = 1$	**Step 2** $\Phi = 0 \wedge \Phi_s = 1$	**Step 3** $\Phi = 1 \wedge \Phi_s = 0$	**Step 4** $\Phi = 0 \wedge \Phi_s = 0$
C(x)=60 pF	V_r= 5 V	0 V	0 V	0 V
C_p=100 nF	V_{os_A1}=1 mV	V_{os_A1}=1 mV	V_{os_A1}=1 mV	V_{os_A1}=1 mV
C_s=1 nF	0 V	300 mV	0 V	300 mV
C_h=3.9 nF	0 V	300 mV	300 mV	300 mV
C_d=1.5 nF	V_{os_A2}=1 mV	V_{os_A2}=1 mV	166 mV	34 mV
C_c=50 pF	0 V	0 V	0 V	V_c= 5 V
C_r=100 pF	0 V	0 V	0 V	V_r= 5 V
C_f=1.5 nF	0 V	V_{os_A2}=1 mV	0 V	34 mV

Table 4.2: Simulation results for the SCI. A pressure applied on C(x) is assumed so that its capacitance is equal C_0+10 pF where C_0=C_c=50 pF.

in steps 2 and 4 and

$$V_{C_d} = (Q_{C(x)} - Q_{C_c})/C_d = 50[pC]/1.5[nF] = 34mV \tag{4.8}$$

in step 4.

Even though a great deal of this type of interface could have been realized with the aid of a microcontroller, as it is done for the circuit described in the next section, it is not possible to fit the switch capacitor interface on a Grundfos PCB so the effort to redesign the circuit is not justified.

4.4 Charge-Discharge circuit for TMCPS

Even though the Switch Capacitor Interface described in the previous section has some desirable characteristics such as the digital output, high immunity to noise and stray capacitances, compensation for the zero pressure capacitance and single supply operation, its complexity (i.e. cost) and especially size are clearly inadequate for Grundfos application. The Charge Transfer Principle is therefore studied because of its circuit simplicity (i.e. low cost), suitability for manufacturing as a single integrated circuit and its ability to eliminate stray capacitance [61]. The measurement method is based on a sensor and a reference capacitor, which are simultaneously charged with a DC voltage with the same amplitude but opposite polarity. When pressure is applied on the sensor the difference between the two capacitances leads to a current pulse, which is read by a current detector also known as a transimpedance amplifier. The current detector output is proportional to the pressure change on the sensor.

Fig 4.16 shows the basic schematic for this circuit, C_x and C_r indicate the sensor and reference respectively, $S1$-$S6$ are 6 CMOS switches, C_f and R_f are the feedback capacitor and resistor respectively and C is a decoupling capacitor which absorbs spurious spikes generated from the discharging current that flows in the input impedance of the amplifier without affecting the mean charge measured. The charge/discharge sequences are controlled by six switches, operating at a frequency of 50 kHz which control signals are presented in Fig. 4.17. The frequency chosen gives enough time to the capacitors in the circuit to be fully charged and is high

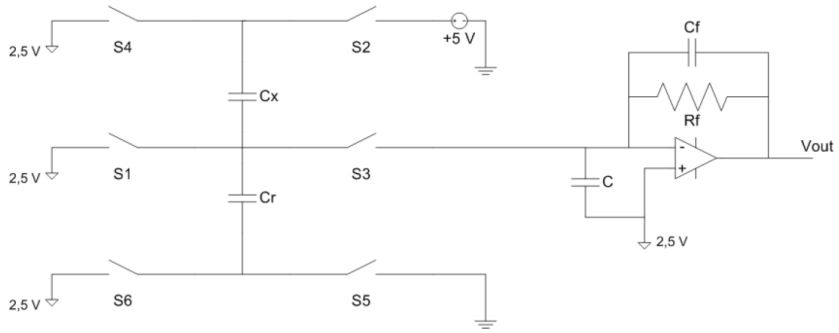

Figure 4.16: Charge-discharge system designed to work with single supply using 2.5 V as ground reference. S1 to S6 are CMOS switches, C_x and C_r are the sensor and reference capacitance respectively while C is used to absorb the spikes generated by the switches.

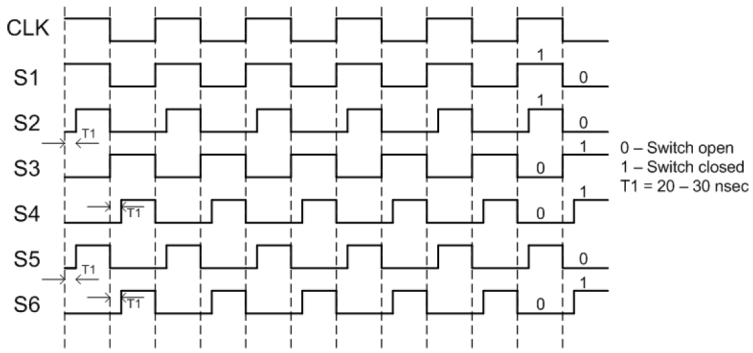

Figure 4.17: Timing diagram showing the control signals for the switches S1-S6 of the charge discharge conditioning circuit.A build in time delay T1 makes sure that no overlapping occurs in places where voltage supplies could get short-circuited to ground.

enough to guarantee a good sensitivity but low enough to keep noise at a reasonable values. The output characteristic of this system has previously being estimate [25]:

$$V_{out} = fR_f(C_x - C_r)\frac{V_{dd}}{2} + V_{os} + iR_f, \tag{4.9}$$

where f indicate the switching frequency, V_{dd} is the supply voltage, V_{os} is the input offset voltage of the amplifier and i is the input offset current.

The theoretical sensitivity achievable is evaluated by differentiating eq. 4.9 with respect to the difference between the two capacitances:

$$S = fR_f\frac{V_{dd}}{2}, \tag{4.10}$$

which, for the circuit presented, is calculated to be 6.25 mV/pF. Unfortunately, as shown from the simulations, the dynamic range of this circuit is strongly influenced by the maximum output

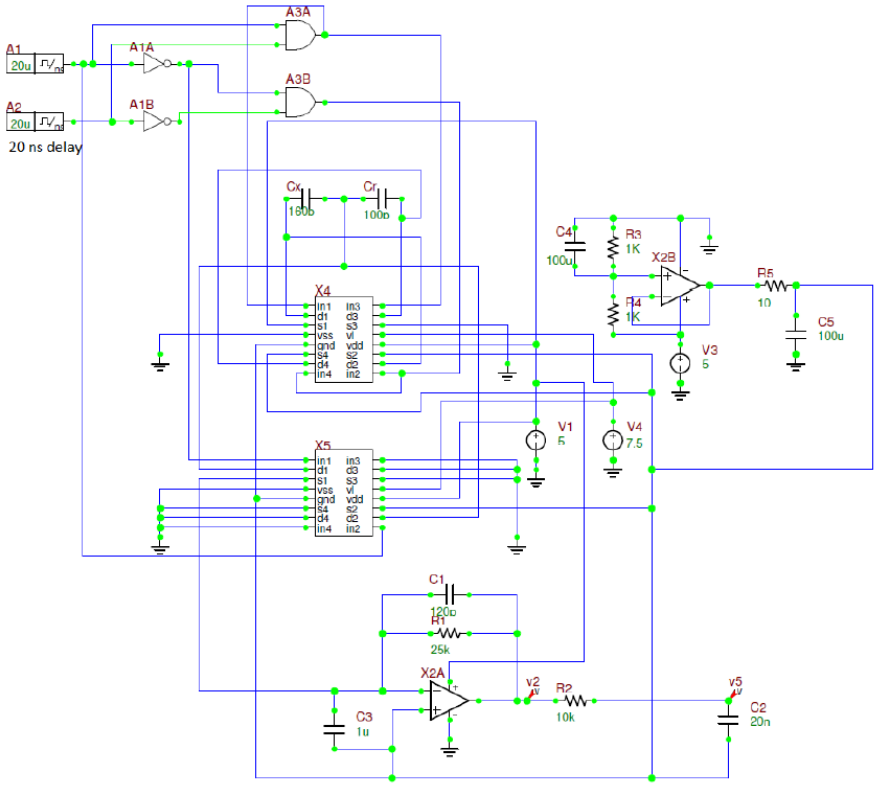

Figure 4.18: Complete Charge Transfer circuit simulation done in B2Spice. Single supply with 2.5 V as ground reference created by the operational amplifier X2B. To make sure the switches operate properly, a 7.5 V supply has been used.

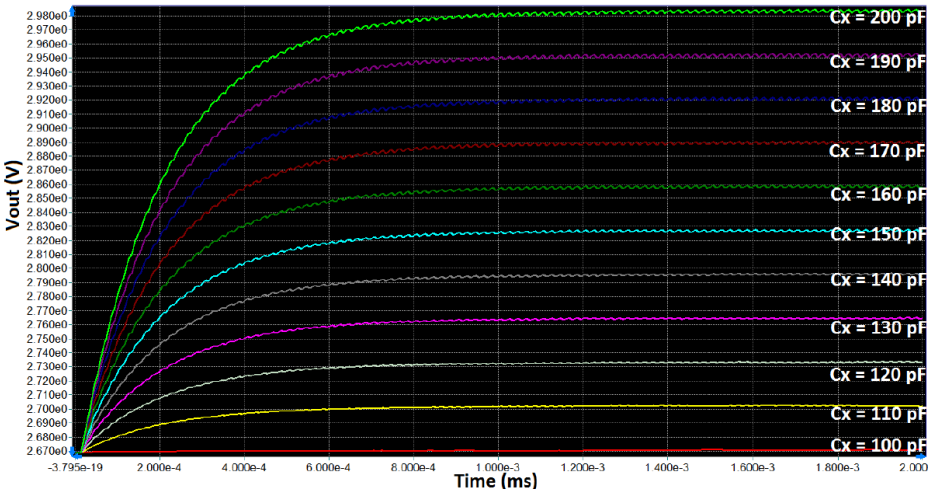

Figure 4.19: Transient simulation of Charge Transfer System. A parametric sweep of the sensor capacitance C_x from 100 to 200 pF results in change in output voltage.

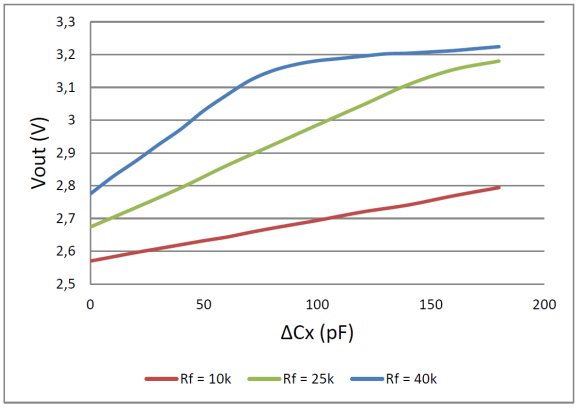

Figure 4.20: Simulation of output voltage based on the difference in capacitance between the sensor and reference of The Charge Transfer System for three different values of the feedback resistor R_f.

voltage of the operational amplifier. Fig. 4.18 shows the schematic of the charge/discharge circuit simulated and the result of a parametric simulation which varies C_x from $C_x = C_r = 100pF$ to $C_x = 200pF$ is shown in Fig. 4.19, from the last figure a sensitivity of 3.1 mV/pF can be evaluated. The output voltage swing has an impact on the sensitivity of the circuit an its dynamic range as it is shown in Fig. 4.20 where the parametric simulation has been performed for different values of the feedback resistor and therefore for different sensitivities. Furthermore, differentiating Eq. 4.9 and dividing the result by eq. 4.10, the change in measured capacitance due to parameters variations can be obtained:

$$\Delta C_m = \Delta C_x - \Delta C_r + (C_x - C_r)\left(\frac{\Delta V_{dd}}{V_{dd}} + \frac{\Delta R_f}{R_f} + \frac{\Delta f}{f}\right) + 2\frac{\Delta V_{os} + \Delta i R_f}{f R_f V_{dd}}. \tag{4.11}$$

In this project the sensor and reference capacitor are meant to be two TMCPS dies picked from the same wafer and fabricated close to each other, therefore they can be considered almost identical (less then 0.1% maximum variation). Furthermore, they have almost identical baseline drift being placed close to each other an subjected to the same temperature changes. The last term of Eq. 4.11 results to be in the order of 0.01pF for a 10°C if a JFET input operational amplifier in chosen and a sensitiviti of around 10 mV/pF is achieved. So, it can be safely stated that, the baseline drift is not an issue for this type of circuit. Finally, in the next chapter, it is shown how the charge/discharge circuit is implemented with a very limited number of components therefore making it suitable for Grundfos application.

4.5 The AC bridge circuit

The system proposed is a stand alone implementation of the well known AC-Bridge where both the source and the detector have been designed. Furthermore an AC-DC converter has been added to be able to read the output signal with a simple multimeter. In Fig. 4.21 a block diagram of the circuit proposed is shown. First an AC signal is generated by the source which, in this case, is the Wien-Bridge oscillator described in the next section. The output signal is then

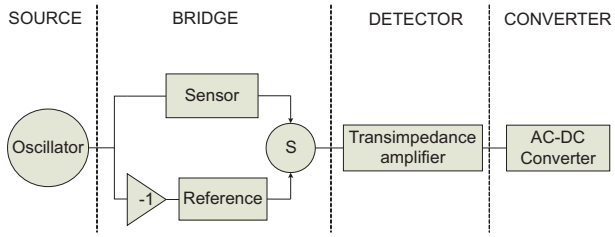

Figure 4.21: Block diagram of the system proposed. Only four main building blocks are used: a signal source, an AC-bridge network, a current detector and an AC-DC converter.

replicated and fed into the sensor in one half of the bridge by means of a center tapped transformer or a fully differential amplifier. In the other half the signal is phase-inverted and fed into the reference; both sensor and reference are TMCPS microfabricated on a silicon die. The amplitude of the output of the transimpedance amplifier (indicated as detector in the drawing) will then be proportional to any imbalances of the two halves of the bridge. Finally, in order to get a DC voltage readable with a simple multimeter, the signal is rectified and low pass filtered by means of an AC-DC converter. In sections 4 and 5 the bridge circuits and the AC-DC converter implemented will be described. For the sensors and the reference capacitance different solutions have been tried, the use of variable capacitances and the use of microfabricated TMCPS which are described elsewhere [58]. In the last case, a setup capable of varying the pressure applied on the sensor, from 1 to 7 bars, in steps of 100 mbar, while monitoring the output of the system with a multimeter, has been implemented. Overall, the design proposed consists of only 4 building blocks, namely, the source, the bridge, the detector and the converter; this simplifies its implementation with discrete components and its debugging. Furthermore, utilizing a current detector with very low input impedance makes the system inherently immune to stray capacitance, as it will be demonstrated in Section 4.5.2.

4.5.1 Source

Multiple ways of creating an oscillator exists today. The Wien-Bridge is one of these. For the system mentioned in the previous section a Wien-Bridge is used to generate a sinusoidal signal. In Fig. 4.22 the Wien-Bridge is shown where two possible configurations used as amplitude limiters are depicted (figure 4.22 A and B). The Wien-Bridge consists of an operational amplifier connected in the non-inverting configuration with a closed-loop gain, G,

$$G = 1 + (R1/R2), \tag{4.12}$$

when the automatic amplitude control branch is disregarded. The positive feedback loop is connected to a RC network which determines the oscillation frequency, f,

$$f = 1/(2 * \pi * R * C), \tag{4.13}$$

where $R = R4 = R5$ and $C = C1 = C2$. In order to make the system oscillate, the Barkhausen criterion for oscillation must be fulfilled, i.e. the amplitude of the transfer function of the system must be equal to one and its phase has to be zero. Of course these conditions cannot be met by relying on very precise components, therefore, to guarantee oscillations, the amplitude of the transfer function is made bigger than one and some kind of amplitude stabilization is needed.

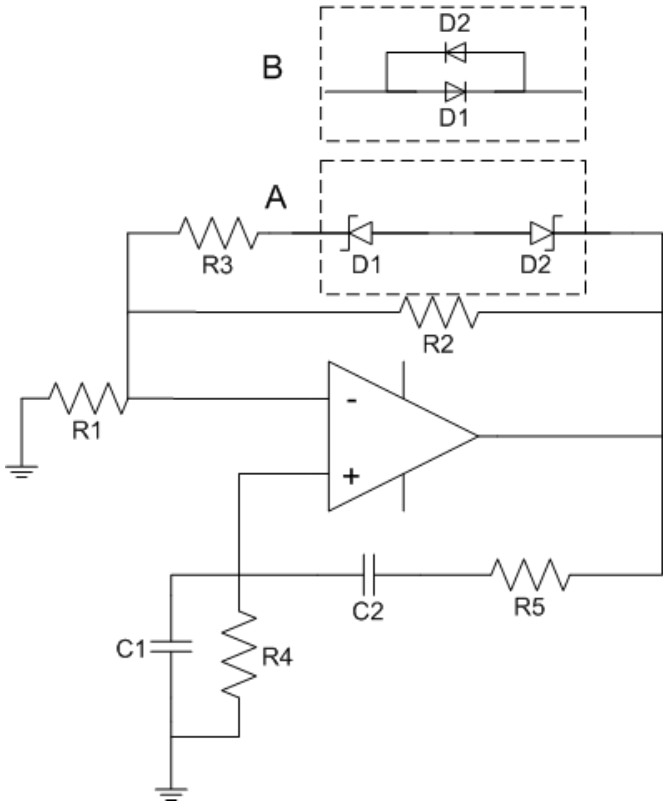

Figure 4.22: Oscillator circuits. A Wien-Bridge oscillator with two different limiting circuits has been tested, the first has a back to back Zener diodes configuration (A), while the second has two signal diodes in an anti-parallel configuration (B).

Aplitude stabilization method	R3 (KΩ)	Theoretical f_0 (KHz)	Measured f_0 (KHz)	Deviation (%)
Back to back Zener diodes	0	14.18	10.63	23.98
	2.5	14.18	10.96	22.71
	0	98.83	54.15	45.20
	0.05	98.83	54.50	44.85
Signal diodes	10	14.18	13.93	1.80
	13.62	14.18	13.74	3.14
	50	98.83	84.91	14.08
	170	98.83	95.66	3.21

Table 4.3: Theoretical and measured resonance frequency for the two configuration proposed in Fig. 4.22 evaluated for the minimum and maximum value of $R3$ which still allows oscillation.

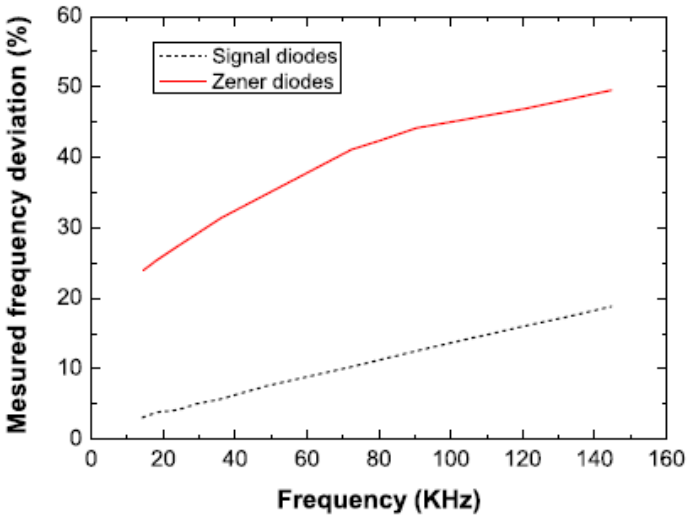

Figure 4.23: Measured frequency deviation from the theoretical resonance frequency calculated for the circuits in Fig. 4.22 A (solid) and B (dashed).

A way of limiting the amplitude of the oscillations is by adding, in parallel to the resistor $R2$, a branch made of a back to back configuration of Zener diodes ($D1$ and $D2$ in Fig. 4.22 A), in series with a resistor, $R3$. Another way would be to add an anti-parallel configuration of signal diodes instead of the back to back configuration of Zener diodes (figure 4.22 B). Both of these options have been tested and the results can be seen in table 4.3 where the theoretical frequency and the measured frequency along with their discrepancy are reported for the minimum and maximum value of $R3$ which allows oscillations. The frequency interval chosen, namely 14 KHz ($R4 = R5 = 5.1$ KΩ and $C1 = C2 = 2.2$ nF) to 100 KHz ($R4 = R5 = 7.32$ KΩ and $C1 = C2 = 220$ pF), is motivated by the fact that the lower corner frequency of the transformer chosen for the bridge circuit (which has a bandpass transfer function) is in fact 10 KHz and by the fact that the distortion and deviation from the theoretical frequency rise with an increase in frequency. As the table clearly shows, the Zener configuration have several disadvantages, not only a strong deviation of the measured frequency from the expected value, but also a much smaller tolerance on the value of $R3$ in order to allow oscillation. In the worst case there was more than 50 % difference between theoretic and measured values. Figure 4.23 shows that the relationship between frequency and deviation of the measured value from the expected value is almost linear in both cases, but the deviation is much bigger if the Zener diodes are used. Finally we also noticed that at 14 KHz the amplitude of the output signal is larger when the anti-parallel diode configuration is used being 3.25 V instead of the 2.97 V measured when the Zener diodes are used. Based on all the measurements presented it seems obvious that the anti-parallel configuration gives the best results for the application proposed, therefore an oscillator employing that configuration will be used.

4.5.2 Bridge circuits and current detector

The general structure of the AC-Bridge is shown in Fig. 4.24 A, where the AC-Bridge is designed to measure one of the four impedances shown. In Fig. 4.24 B and C two special cases

of the AC-Bridge are shown, namely the transformer arm-ratio bridge [62] and an electronic ratio-arm bridge where the two sinusoids with opposite phase are generated with a fully differential operational amplifier. An earlier version of this circuit, described in [63], used two wide bandwidth operational amplifiers with low output impedance in order to generate the necessary signals. The two amplifiers are connected in the inverting and non-inverting configuration to achieve the 180° phase shift but, due to a difference in the phase of the transfer function of the two configuration, to achieve good results this phase difference must be compensated. The new solution here proposed consists of a fully differential operational amplifier which eliminates the need of such compensation. In the case of the transformer arm-ratio bridge, impedances $Z1$ and $Z4$ corresponds to the secondary coils of a center tapped transformer, while for the electronic ratio-arm bridge, they are the output impedances of the fully differential amplifier. In both cases $Z2$ and $Z3$ are given by the sensor capacitance, C_x, and the reference capacitance, C_r, respectively. A transimpedance configuration is then used as a current detector. The feedback network of the transimpedance amplifier is given by the parallel combination of a large value resistor, R_f, (100MΩ) and a low value capacitor, C_f, which sets the dynamic range of the measurement. As it is clear from the frequency response of the system

$$H(j\omega) = \frac{j\omega(C_r - C_x)R_f}{1 + j\omega C_f R_f}, \tag{4.14}$$

given the following condition,

$$\omega C_f R_f >> 1 \tag{4.15}$$

the modulus of the frequency response becomes dependent only on the capacitors present in the circuit,

$$|H(j\omega)| \cong (C_r - C_x)/C_f \tag{4.16}$$

and the phase shift is close to zero,

$$\angle H(j\omega \cong 0 \tag{4.17}$$

where ω is the angular frequency. The high value resistor in the feedback loop is necessary to guarantee the condition given by (4.15), but it can be substituted by a T configuration of smaller value resistors as shown in [31]. As previously mentioned, the output of the current detector is fed into an AC-DC converter in order to obtain a stable DC signal measurable with a simple multimeter; the converter will be described in the following section.

4.5.3 Converter

To make the AC to DC conversion, a well-known full wave rectifier together with a low pass filter is used (see figure 4.25). A variable resistor, R_f, has been placed in the feedback loop of the low pass filter in order to adjust the dynamic range and the resolution of the system. A large value capacitor is used in the low pass filter to minimize the ripple of the output voltage accordingly to the following criterion [64]:

$$C_f >> 1/(4\pi R_f f_{min}) \tag{4.18}$$

where f_{min} is the minimum operating frequency of the system, which in our case is 15 KHz (limited by by the transformer bandwidth). Finally, a fast-settling JFET-input operational amplifiers has been chosen so that a high peak-to-peak signal with large bandwidth can be processed.

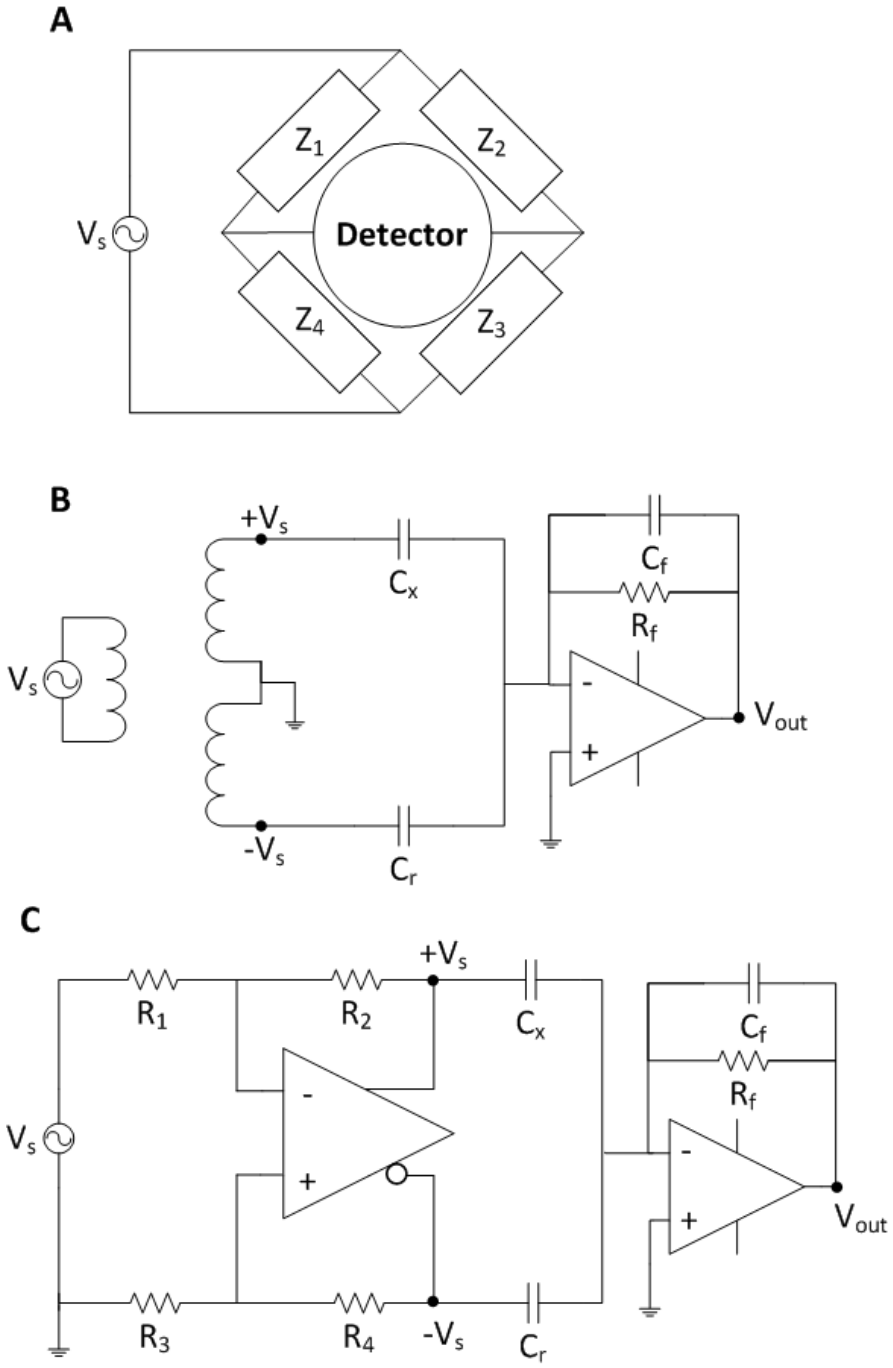

Figure 4.24: Bridge circuit schematics. AC-bridge principle (A), the transformer arm-ratio bridge (B) and the electronic-arm ratio bridge (C). In the last two cases the detector is given by the operational amplifier in the transimpedance configuration shown with feedback loop consisting of a large value resistor, R_f, and a small value capacitor, C_f.

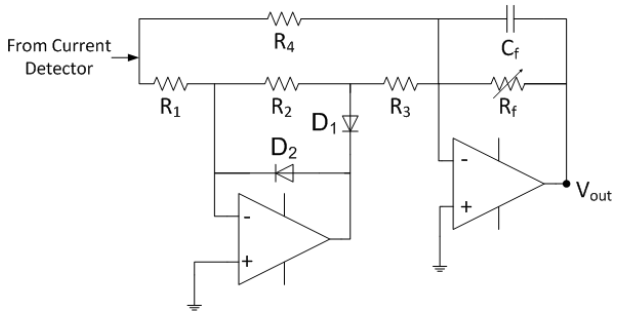

Figure 4.25: AC-DC converter. The circuit is given by a full wave rectifier and a low pass filter with a variable resistor, R_f, which allows for adjustments of the dynamic range.

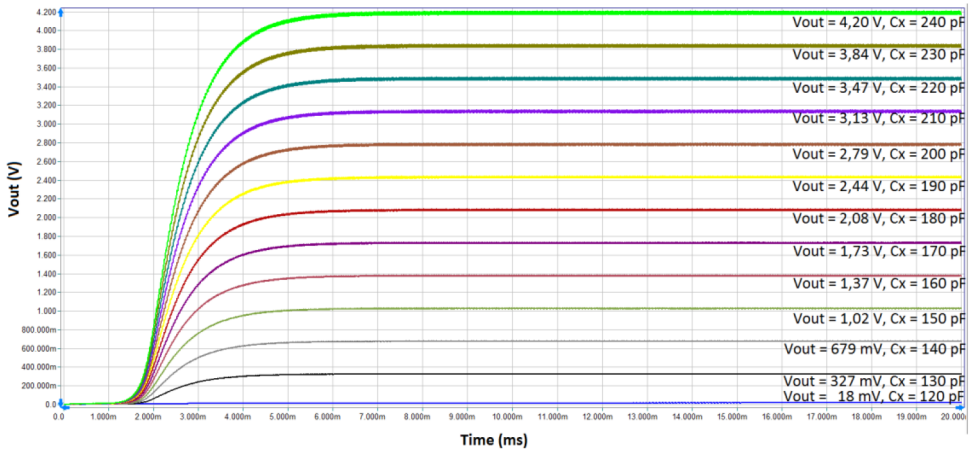

Figure 4.26: A B2Spice simulation of electronic-arm-ratio bridge. The transient simulation shows the output voltage for 10 pF increase in sensor capacitance with a dynamic range of 120 pF.

Both the electronic-arm-ratio bridge and the transformer-arm-ratio bridge have been simulated showing a sensitivity of 34 mV/pF and 37 mV/pF respectively. These results are extracted from Fig. 4.26, where a parametric sweep of the sensor capacitance from 120 pF to 240 pF is shown. The theoretical value for this circuit is calculated differentiating, with respect to difference in capacitance, the output of the full system:

$$V_{out} = \frac{(C_x - C_r)}{C_f} A_{ac-dc} V_{in}, \tag{4.19}$$

where V_{in} is the peak value of the oscillator output, that can at most reach the positive rail of 4.2V, and A_{ac-dc} is the gain of the convreter that is typically adjusted to 1.11. The theoretical sensitivity is therefore given by

$$S = \frac{A_{ac-dc}}{C_f} V_{in} = 38.8 mV/pF, \tag{4.20}$$

and it is in close agreement with the simulation results.

The AC bridge circuit is the interface that has been studied more intensively in this project and since it was a mature and tested method much before the other type of conditioning circuit were studied, it has been chosen to be implemented on a Grundfos PCB as it is shown in the next chapter. All the method so far proposed and studied are summarize in the next section which concludes the chapter of the electronics developed for signal conditioning of TMCPS.

4.6 Conclusion

In this project great effort was made to propose different electronic solutions to interface the TMCPS described in the previous chapters. The signal conditioning electronics is in fact equally important to the sensor in an optic of product development. To address this problem an equivalent circuit for the TMCPS was studied and the effects of the resistive contributions as well as the parasitic capacitances contributions was pointed out. Then three possible solutions are proposed, and compared in terms of their theoretical characteristics and advantages or disadvantages with respect to Grundfos requirements. Their theoretical behavior has also been validated by means of numerical simulations performed with a commercial software. This study is finalized in the next chapter where the fabrication and characterization of these circuits is described together with the other important results achieved in this project. Furthermore, the AC bridge circuit just illustrated, is chosen as the signal conditioning circuit to be mounted on the first demonstrator of the full system consisting of sensor, electronics and packaging solution. The results of the measurement on the full system are also presented in the next chapter.

Chapter 5

Characterization of capacitive pressure sensesor and interfacing electronics

After discussing the model, the fabrication and the interfacing electronics for TMCPS, it is necessary to present the experimental results collected in this project. This chapter starts form the device characterization where the model described in Chapter 2 is used to fit the capacitance pressure curves measured. Furthermore, the die is characterized at different temperatures and a small discussion on the coating is drawn. Then,the different electronic circuit are depicted starting from their fabrication and concluding with their complete characterization. This chapter ends with the most important result of the project namely a demonstrator of a TMCPS with the interfacing electronics fabricated onto a Grundfos PCB and therefore completed with a packaging solution.

5.1 Touch mode pressure sensor characterization

This project starts with the development of touch mode capacitive pressure sensor which design and fabrication are described in Chapter 3. An example of a finished chip is shown in Fig. 5.1, this die has been produced with the 4-mask process and no coating was applied in this case. The insulation groove is seen to enclose both the membrane area and also a bonding pad (contact 3) that is connected to the membrane area. In order to characterize the response of the sensor it is glued to a TO head with a non-conducting epoxy. The separated part of the device layer and the bottom electrode are connected by the wire bond between contacts 1 and 2. This ensures that these are kept at the same potential, hereby removing a large part of the parasitic capacitance that, in the previous chapter, was estimated to be more than 700pF. The membrane area is interconnected using a wire bond to contact number 3. In all the batches produced, the bonding pads have been placed in the corners of the chip to make room for the O-ring as part of the final packaging of the sensor. All the chips fabricated are assumed to have negligible resistive contribution in the electrical equivalent circuit illustrated in the previous section. To proof what has been stated so far a measurement setup consisting of a Druck DPI 520 pressure controller and a HP 4294A Precision Impedance Analyzer (see Fig. 5.2). Both instruments have been connected to a laptop and controlled by a custom Labview program. The TO head with the glued TMCPS is then placed in a stainless steal chamber connected to the pressure controller.

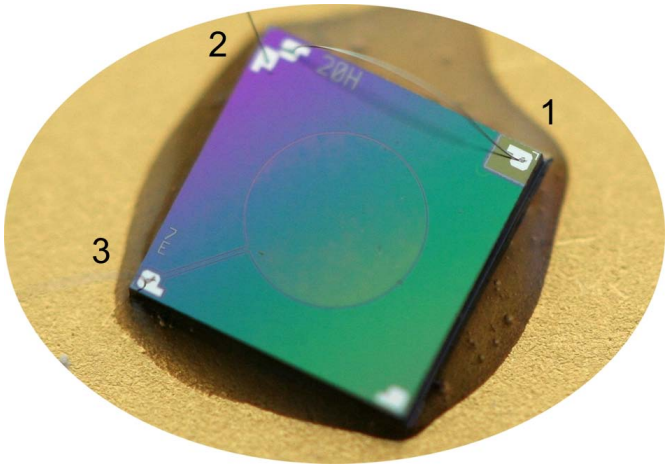

Figure 5.1: Picture of a finished sensor mounted with glue on a TO head for testing. The groove that separates the membrane area from the separated device layer area is seen to extend down and around contact number 3. Note that this groove is covered by a 500 nm SiO_2 layer to prevent liquid from entering the groove. Numbers indicate contact number according to Fig. 2.

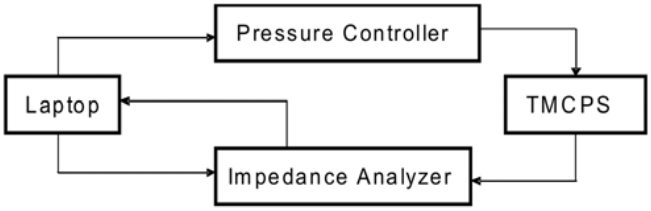

Figure 5.2: Schematic of the measurement set-up. A Druck DPI 520 pressure controller and a HP 4294A Precision Impedance Analyzer are controlled by a laptop where a Labview code has been implemented. For each pressure value applied on the TMCPS an impedance measurement is performed by the analyzer.

The C-P curve has been obtained varying the pressure from 250 mbar to 10 bar with a minimum achievable step of 10 mbar. Fig. 5.3 shows a typical measurement performed on a sensor to characterized it electrically (no pressure applied). The frequency ranges from 50 Hz to 10 MHz where the sensor exhibits almost perfect capacitor behavior in the entire frequency range, thus neither series resistance nor parallel conductance affect the device significantly. Up to around 5 MHz (far more than what is interesting for any Grundfos application) the device can be assume to be an ideal capacitor since the following equation holds up to the numerical limits of the instrument

$$C = \frac{1}{2\pi f |Z|}, \tag{5.1}$$

where f is is the frequency and $|Z|$ is the modulus of the impedance.

In the next section, the sensor is characterized mechanically and electro-mechanically and, with the aid of the model proposed in Chapter 2, some of its important fabrication parameters are fitted from the measured capacitance-pressure (C-P) curves.

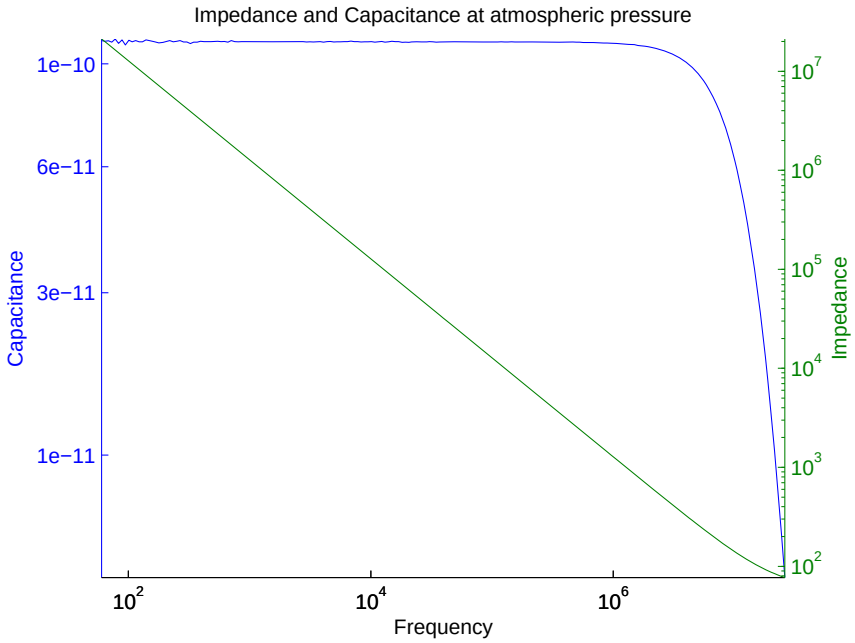

Figure 5.3: Capacitance and Impedance as a function of frequency measured for one of the working sensor.

5.1.1 Fitting of measurements data

Eq. (2.10) and (2.22), which where derived in Chaper 2, can be used here to fit the C-P curve measured with the setup described in the previous section. The first of them

$$C = \int_0^{2\pi} \int_0^{a_0} \frac{\varepsilon_0 \varepsilon_{ox} r dr d\theta}{t_{ox} + \varepsilon_{ox}(g - w(r))} = C_0 \frac{\operatorname{arctanh}(\sqrt{\xi})}{\sqrt{\xi}}, \tag{5.2}$$

models the sensor capacitance in normal mode operations while the second

$$C \approx C_{ox} \left(\sqrt{\frac{1}{\kappa p}} - 2\sqrt[4]{\frac{1}{\kappa p}} + 1 \right), \tag{5.3}$$

with κ being defined from (2.22)

$$\kappa = a_0^4 / (64 D g). \tag{5.4}$$

applies to touch mode regime. In order to do so, some geometrical parameters measured during fabrication, are needed, their values are presented in Table 5.1. Then, fitting parameters are calculated and physical quantities such as the flexural rigidity and the parasitic capacitance are estimated.

Normal mode

Fig. 5.4 shows the capacitance pressure characteristics for the sensor when working in normal mode. Eq. (2.10) is a useful starting point for analysis of the sensor. By adding a parasitic

Parameter	Measured value
a_0	75 μm $\pm$1 μm
N	180
g	420 nm $\pm$5 nm
t_{ox}	30 nm $\pm$5 nm

Table 5.1: Measured geometrical values of the sensor fabricated.

Parameter	Fitted value
NC_0	62.0 pF
C_p	71.8 pF
D	2.19×10^{-7} Nm

Table 5.2: Results from the analysis of normal mode behavior.

capacitance C_p and assuming $g\varepsilon_{ox} \gg t_{ox}$, we obtain

$$\xi = \frac{w_0}{g\left(\frac{t_{ox}}{g\varepsilon_{ox}}+1\right)} \approx \frac{w_0}{g}, \tag{5.5}$$

and

$$C(p) = NC_c(p) + C_p = NC_0\sqrt{\frac{1}{\kappa p}}\operatorname{arctanh}\left(\sqrt{\kappa p}\right) + C_p, \tag{5.6}$$

Noting, that $C(0) = NC_0 + C_p$, we can write

$$C = NC_0\left(\sqrt{\frac{1}{\kappa p}}\operatorname{arctanh}\sqrt{\kappa p} - 1\right) + C(0), \tag{5.7}$$

which is a suitable fitting function with three parameters C_0, $C(0)$ and κ to be determined from the plot. This expression has been used as a fitting function to analyze the data shown in Fig. 5.4, the solid line shows the fit. As a_0, N and g can be measured it is possible to obtain the effective plate stiffness, D, from the fit. The extracted values are shown in Table 5.2. The rigidity is as expected around 2×10^{-7} Nm, as can be estimated from Eq. (2.2).

Touch mode

In Fig. 5.5 the overall capacitance pressure characteristics is shown. The fact that Eq. (2.19) can be represented by a second order polynomium in $p^{-1/4}$ is used in this section for analysis of the sensor when working in touch mode (see Fig. 2.2). By adding a parasitic capacitance, C_p, to Eq. (2.19) we obtain

$$C(p) \equiv b_0 + b_1 p^{-1/4} + b_2\left(p^{-1/4}\right)^2, \tag{5.8}$$

where the coefficients are $b_0 = NC_{ox} + C_p$, $b_1 = -2\left[1 - k_2(1-\gamma)\right]NC_{ox}/\sqrt[4]{\kappa}$, and $b_2 = \left[1 + 2(1-\gamma)(k_1 - k_2)\right]NC_{ox}/\sqrt{\kappa}$.

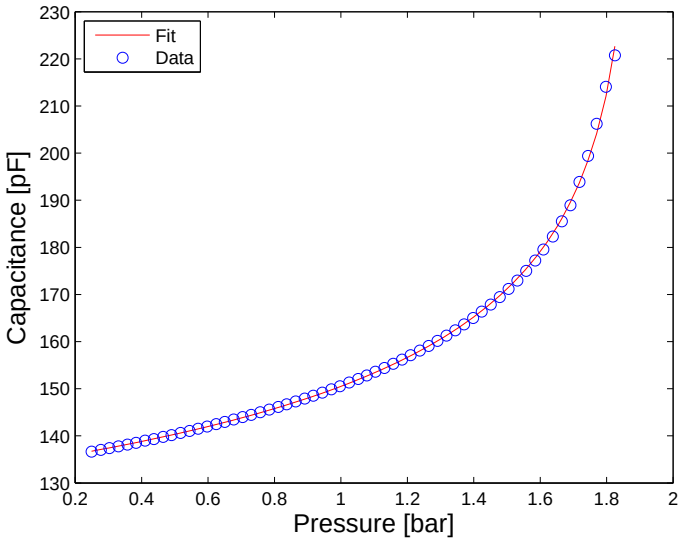

Figure 5.4: Capacitance pressure characteristics of the sensor in normal mode. The solid line represent the fit calculated using Eq. (5.7), on the data points (circles) measured from 250 mbar to 1.8 bar.

From the relation between γ and the capacitance ratio

$$\gamma = 1 - \frac{NC_0}{NC_{ox}} = 1 - \frac{NC_0}{b_0 - C_p}, \tag{5.9}$$

we calculate γ, which is very insensitive to errors in the parasitic capacitance C_p since $NC_{ox} \gg C_p$ (for the present sensor C_p is less than 2% of NC_{ox}). The oxide thickness may be calculated directly from

$$t_{ox} = N\frac{\pi a_0^2 \varepsilon_0 \varepsilon_{ox}}{NC_{ox}} = N\frac{\pi a_0^2 \varepsilon_0 \varepsilon_{ox}}{b_0 - C_p}, \tag{5.10}$$

which also is quite insensitive to C_p. Finally, the flexural rigidity (and thus κ) may be calculated from

$$D = \frac{1}{4g}\left(\frac{a_0 b_2}{-b_1}\right)^4 \frac{\left[1 - k_2(1-\gamma)\right]^4}{\left[1 + 2(1-\gamma)(k_1 - k_2)\right]^4}, \tag{5.11}$$

while the exact value of C_p is calculated such that the coefficients b_0, b_1, and b_2 are consistent with the calculated parameters.

Thus, the oxide thickness t_{ox}, the parasitic capacitance C_p and the flexural rigidity D can be obtained from the fit. Table 5.3 shows the extracted values in the touch mode case. The oxide thickness is in good agreement with the fabrication value and the value extracted for the parasitic capacitance is close to the one reported in Table 5.2 for the normal mode case. Also here, the rigidity is around 2×10^{-7} Nm.

In the next section we will use the results obtained from this section in order to fit the entire C-P curve of the TMCPS described previously.

Parameter	Fitted value
t_{ox}	27.5 nm
C_p	70.5 pF
D	2.72×10^{-7} Nm

Table 5.3: Results from the analysis of touch mode behavior.

Complete C-P curve

In the previous section the problem was split into two: the normal mode and the touch mode region. Combining Eq. (5.7) and Eq. (5.8) it is possible to obtain a fitting function for the entire C-P curve as it is shown in Fig. 5.5. An excellent match between the data points and the fitting functions is obtained both in the normal mode and in the touch mode region. As shown in the inset of Fig. 5.5, the model does not give as satisfactory as result in the transition region because pull in and adhesive forces have not been taken into account. None the less, the maximum deviation of the model from the data points is only 3.7%. Comparing the extracted values of Table 5.2 and 5.3, two different results for the flexural rigidity are found. This is due to the fact that when the plate touches the bottom of the cavity it becomes stiffer as was noticed in previous work [65]. So, in order to obtain an accurate result for this parameter, both stretching effects and the exact value of the terms in Eq. (2.19) should be taken into account in the fitting function. As seen from Table 4 the fit allows extraction from measurements of the parasitic and ideal capacitance value, the latter being within 10% of the value calculated from the geometrical parameters. The parasitic capacitance extracted from the measurements $C_p \sim 72$ pF is larger than the calculated value of 61 pF, since the calculated parasitic is the pure die parasitic capacitance. The bonding wires, the chip carrier and the measurement set-up add some capacitance that may explain the discrepancy; for instance we have measured 4 pF for an empty chip carrier.

The touch point pressure has been estimated to be at the maximum in the sensitivity curve which is given by the first derivative of the C-P curve, this can easily be extracted from the data points collected. The experimental result of 1.77 bar compares well to the expected value of 1.70 bar calculated from the design.

All the main electro-mechanical parameters such as flexural rigidity, hysteresis, touch pint pressure, active and parasitic capacitance, offset capacitance and frequency limit of the fabricated device have now been investigated. As it has been discussed in Chapter 2, the sensitivity is simply given from the derivative of the capacitance curve with respect to pressure. This has been done numerically on the measured data points. The result is shown in Fig. 5.6 where, as expected, there is a spike around touch point pressure while in touch mode the sensitivity is slowly decreasing still maintaining a high average value (ca. 75 pF/bar). In the next section the temperature dependence of these sensor is addressed.

5.1.2 Temperature dependence

To perform the temperature tests on the TMCPS, the stainless steel chamber containing it is inserted in a Binder M53 temperature test oven for laboratory measurements. Fig. 5.7 shows the capacitance as a function of the applied pressure at different temperatures. It can be noticed that the sensor fabricated has more than 100 pF capacitance change in the range of pressure measured, namely from 250 mbar up to 10 bar. Fig. 5.8 shows the relative change of the output

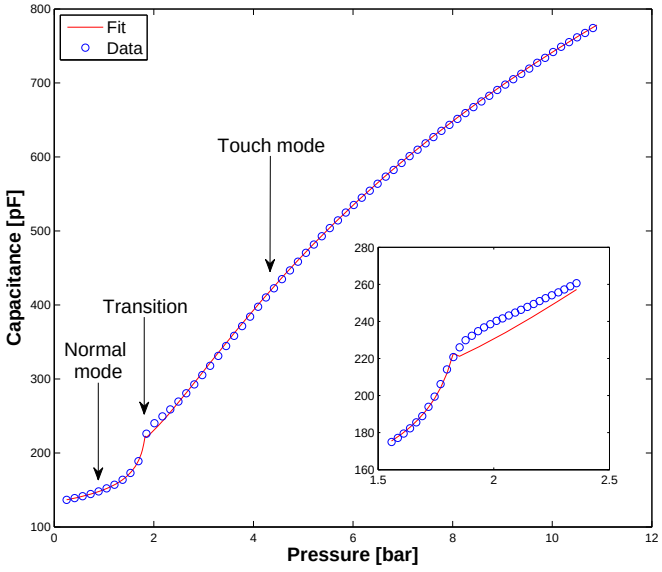

Figure 5.5: Capacitance pressure characteristics in normal, transition and touch mode. Using Eqs. (5.7) and (5.8) a curve (solid line) that can fit the data points (circles) measured both in normal and touch mode has been obtained.

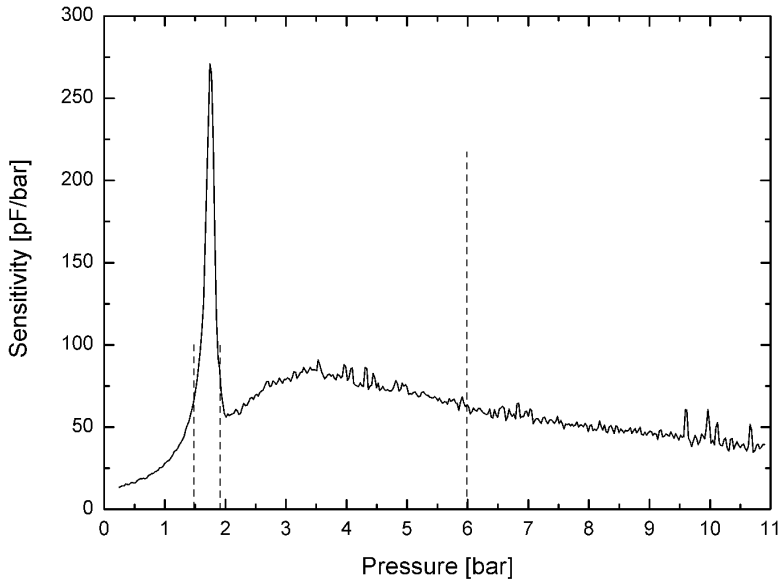

Figure 5.6: Sensitivity curve calculated numerically from the measured capacitance values. The graph closely resemble the shapes of the normalized sensitivities predicted in Chapter 2.

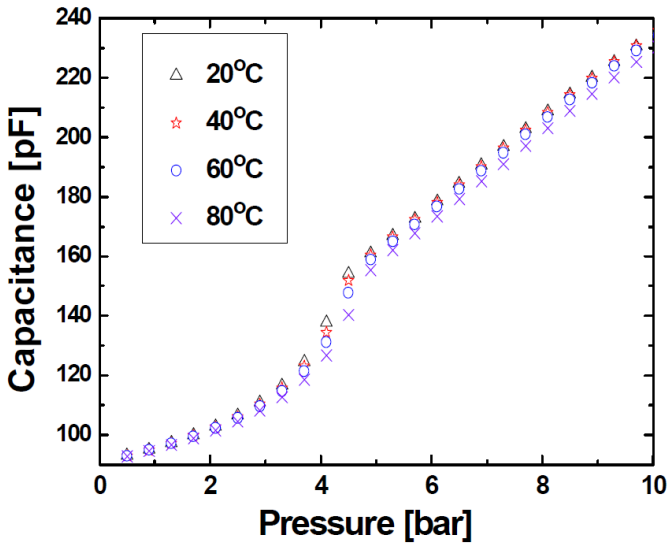

Figure 5.7: Measured capacitance as a function of the pressure at different temperatures.

signal α with respect to the signal at 20 °C (the relative temperature coefficient)

This change has a peak around the touch point pressure and is almost constant or, more precisely, very slowly decreasing, in the touch mode region. In this region an average change in the signal of 0.008 %/°C, 0.023 %/°C and 0.044 %/°C have been measured at 40 °C, 60 °C and 80 °C respectively.

The relative temperature coefficient is unfortunately not linear with temperature increase, non the less, in the worst case is still well below 0.1%/°C, a value that results in a change of 0.8% of the full scale at 80°C which is well below the accuracy of most commercial sensors. In the following section the results for TMCPS fabricated in this project are summarized and compared to the state-of-the-art of this type of device found in literature and on the market.

5.1.3 TMCPS final remarks

A complete characterization of the sensor fabricated has been described so far. Unfortunately, even though sensors with gold coating have been fabricated, it was not possible to perform significant measurements on them. Fig. 5.9 shows a wafer of TMCPS fabricated with the modified coating mask that allows more space around the contacts and a larger clearance between two chips. Even if no defect can be detected by inspection with an optical microscope and even if, as it can be noticed from the image, around 90% of the chip have intact membranes, a resistance of around 100 Ω is measured between top and bottom contact. This make it clearly impossible to measure the capacitance of the dies. A possible cause for this connection between the top and bottom plate of the TMCPS is seen in Fig. 5.10 where a big amount of pinholes are shown. Poor quality of the photoresist layer deposited in the last lithographic process is the reason for the unwanted contacts. None the less, in the previous chapter, the parasitic capacitance due to the coating was estimated to be between 15 pF and 175 pF depending on the coating design. This is not of big concern in the opinion of the author since the pick off methods proposed are based on differential configurations where the sensing element and the reference bear the same

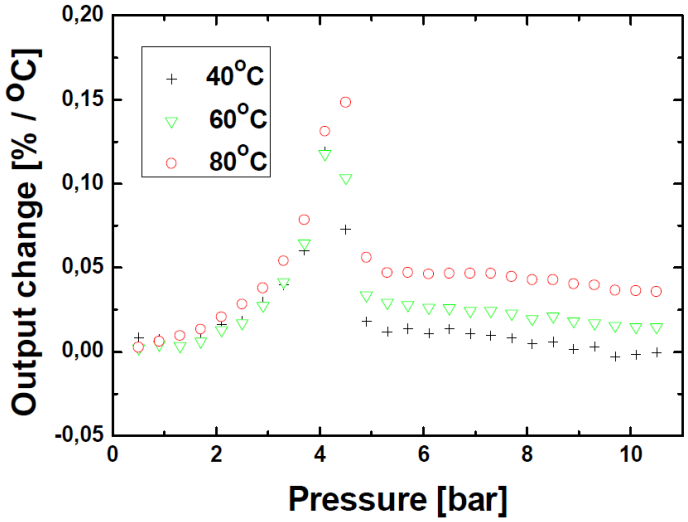

Figure 5.8: Relative output change as a function of the pressure at different temperatures. The output signal at 20 °C has been taken as reference.

Parameter	**DTU/Grundfos**	**Ko & Wang**	**VTI Technology**
Zero pressure capacitance	126 pF	17 pF	7.5 pF
Dimensions	4 mm x 4 mm	1.0 mm x 1.5 mm	1.4 mm x 1.4 mm
Maximum Sensitivity	79 fF/mbar	2 fF/mbar	5.5 fF/mbar
Radius of the membranes	75μm	200μm	N.A.
Gap distance	0.4-0.5μm	2.2μm	N.A.
Temperature coefficient (max)	0.044 %/°C	0.3 %/°C	N.A.
Pressure range	0-10 bar	0 - 8 bar	0.3-1.2 bar

Table 5.4: Characteristics of three capacitive pressure sensors. The sensor fabricated in this project presents higher specifications in most of the characteristics except for its size that was actually decided in advance in order to fit Grundfos existing packaging.

amount of parasitics, thus canceling their effect. To conclude this section a comparison between the TMCPS fabricated in this project and the state-of-the-art of capacitive sensors found in literature and on the market are compared in Table 5.4. The sensor fabricated in this project is much bigger in size than the other reported in this table, this is due to the fact that its dimensions are decided on the basis of the existing package solution (its active area is in fact around 4 mm^2). None the less, the new design proposed, where a parallel connection of capacitive elements is allowed to work in both normal and contact mode, results in much higher sensitivity, signal to noise ratio and pressure range. In the next section, the fabrication and characterization of the interfacing circuits for the TMCPS fabricated are described.

5.2 Electronic circuit fabrication and characterization

In this project three different conditioning circuits have been considered, their working principle and simulation have been described in Chapter 4 and their fabrication and characterization are

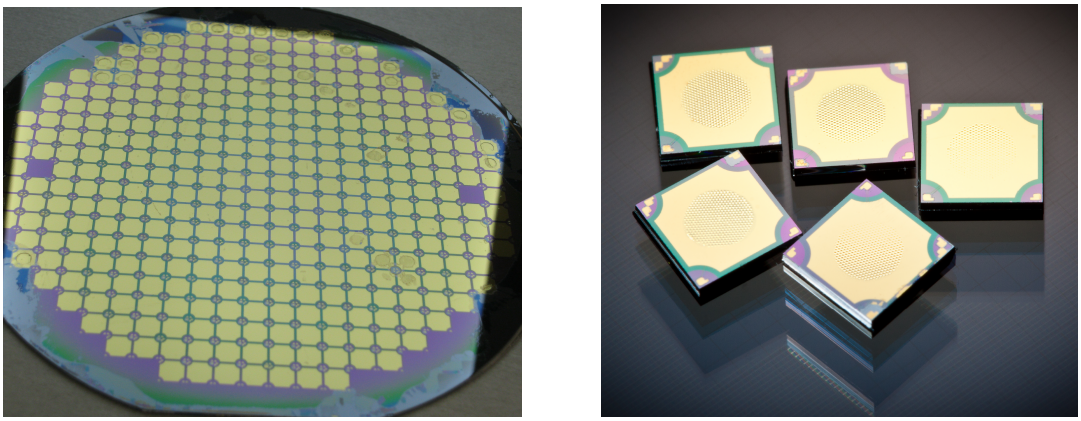

Figure 5.9: TMCPS wafer before dicing (on the left) and after the dies are diced out (on the right). It is possible to notice that only a few of the devices on the wafer have broken membranes suggesting a very high yield achievable.

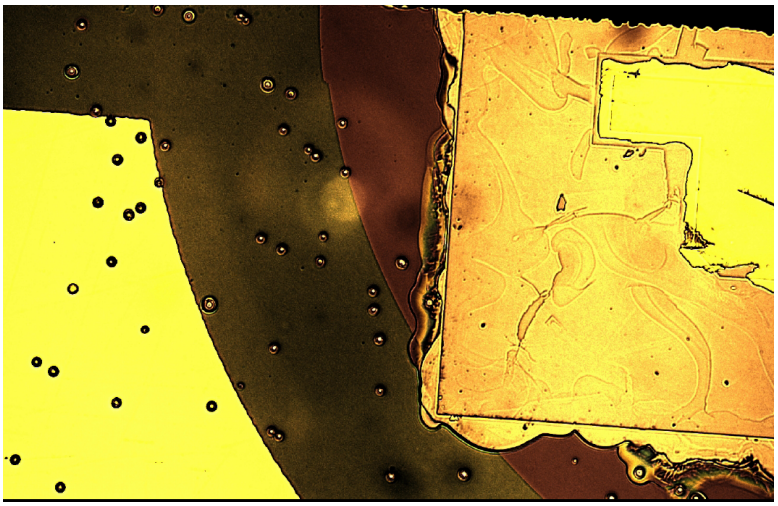

Figure 5.10: Close up image on the bottom contact region. A big amount of pinholes is found and the gold has probably contacted top and bottom plates through them.

presented here. While the AC bridge circuit was already been tested on a plug in breadboard, in a previous work done by the author and could therefore be realized on a printed circuit board (PCB) expecting limited debugging, the fabrication of the SCI and of the charge-discharge circuit is done on a commercial breadboarding system. There are many commercial breadboarding systems, but almost all of them are designed to facilitate the breadboarding of digital systems, where noise immunities are hundreds of millivolts or more. Matrix board (Veroboard, etc.), wire wrap, and plug in breadboard systems (Bimboard, etc.) are, without exception, unsuitable for high performance or high frequency analog breadboarding. They have too high resistance, inductance and capacitance. Even the use of IC sockets is inadvisable. None the less, two systems known as “bird’s nest construction” and Mini-Mount (called Solder Mount in the USA) are suited for analog or mixed signals prototyping. The first of them uses a copper clad board as a ground plane. The ground pins of the components are soldered directly to the plane and the

other components are wired together above it. This allows HF decoupling paths to be very short indeed but there is always the risk of the circuitry being crushed and resulting short circuits, also if the circuitry rises high above the ground plane the screening effect of the ground plane is diminished and interaction between different parts of the circuit is more likely. The Mini-Mount consists of small pieces of PCB with etched patterns on one side and contact adhesive on the other. They are stuck to the ground plane and components are soldered to them. They are available in a wide variety of patterns, including ready made pads for IC packages of all sizes from 8 pin SOICs (small-outline integrated circuits) to 64 pin DILs (dual in-line). This solution has most of the advantages of "bird's nest" (robust ground, screening, ease of circuit alteration, low capacitance and low inductance) and several additional advantages: it is rigid, components are close to the ground plane, and where necessary node capacitances and line impedances can be calculated easily. Nevertheless it is important to configure systems so that sensitive circuitry is separated from noise sources and so that the cross talking mechanisms described (common resistance/inductance, stray capacitance, and mutual inductance) have minimal opportunity to degrade system performance. The general rule, followed when designing all the circuits in this work, is to have a signal path which is roughly linear, so that outputs are physically separated from inputs and logic and high level control signals not too close to this path. Moreover, the negative and positive power rails are made run as close as possible to each other, all the operational amplifiers have been decoupled from the power supply with 100 nF capacitors and voltage regulators have been used, together with high values capacitors and signal diodes, to provide a stable, precise and spike free power signal. The SCI is divided onto three different copper clad boards because of the complexity of the system and to ease the debugging process (Fig 5.11, top). The power regulation and control signals on the first board, the S/H stage on the second PCB and the DI and Comparator on the third PCB. Only one board is instead needed for the charge-discharge circuit (Fig 5.11, bottom) while the AC-bridge is implemented on two PCBs using SMDs (surface mount devices), the first for the oscillator and the bridge, the second for the AC-DC converter. The layout has been designed with a commercial software (CADint PCB) and implemented exposing with UV light and etching with caustic soda a photosensitive copper board. While the first two circuits have been characterized with a capacitor of 120 pF (roughly the same value of the offset capacitance of the sensors) as reference and a capacitor decade box was used as the sensor, the AC bridge uses two TMCPS as reference and pressure sensor (see Fig.5.12).

5.2.1 SCI performances

As mentioned in the previous section, the SCI has been built onto three different copper board, on the first the digital control signals for the switches are implemented. The clock, inverted clock and the sample signal are measured with an Agilent MSO7104A oscilloscope and shown in Fig. 5.13. The result shows that the clocks (green and yellow) are non-overlapping, and that the delay between the clocks is approximately 100 ns. The amplitude of the signals is almost 6 V. This amplification happens in the delay line. The measurement shows that the frequency of the clock is effectively 11.8 kHz. The 700Hz deviation from the theoretical frequency is caused by the tolerance of the passive components in the 555 Timer. Furthermore it shows that the sample signal is the 64 clock periods as expected. Then the S/H circuit is tested, it shows an output signal (V_o), of -475mV for a 60 pF sensor capacitance; this value is not equal to the theoretical and simulated value. This is possibly due to tolerance in the capacitor C_s and parasitics. None the less, for a 10 pF chance in capacitance, the change in output voltage

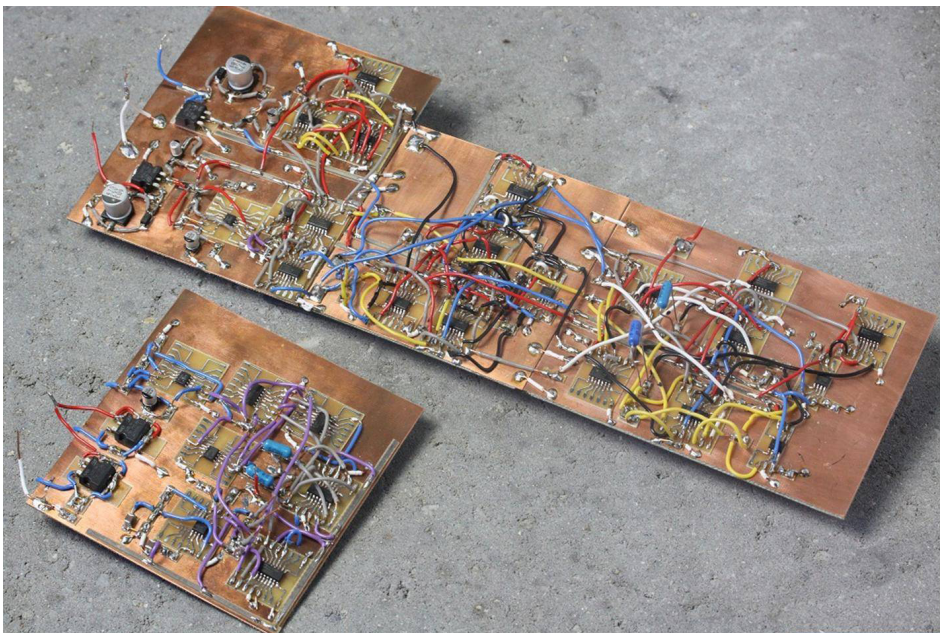

Figure 5.11: Picture of the full system described in Section 4.5. A TMCPS is place in the pressure chamber while another is used as reference sensor in order to achieve the best possible balance condition for the bridge.

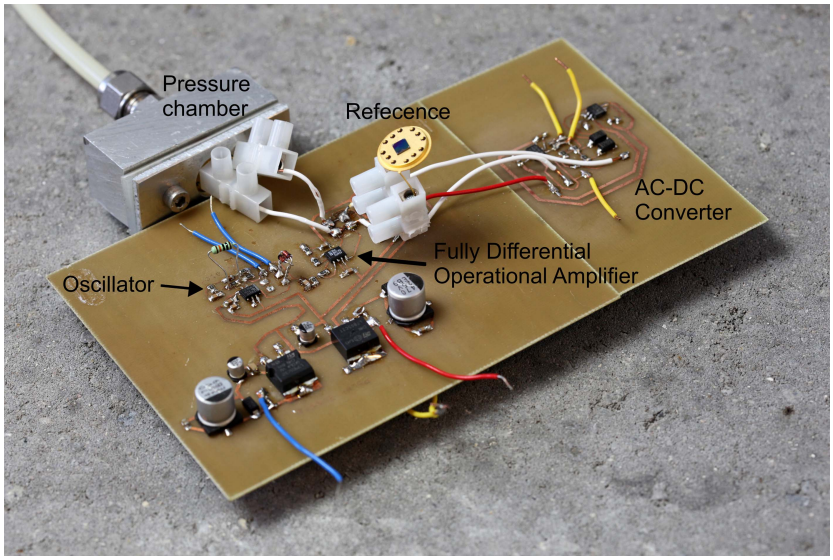

Figure 5.12: Picture of the AC-bridge system. A TMCPS is place in the pressure chamber while another is used as reference sensor in order to achieve the best possible balance condition for the bridge.

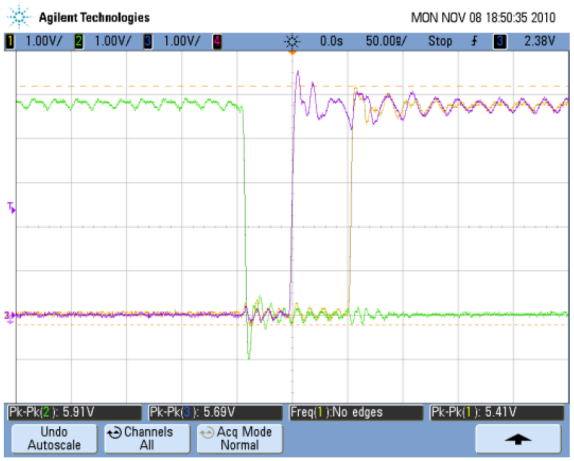

Figure 5.13: Close up test of digital control signals for switches with oscilloscope. Green denotes inverted clock, yellow denotes clock, and pink denotes sample.

is 50 mV, exactly as predicted in Chapter 4 from theory and simulations. Finally the DI is characterized checking the output signal (number of output impulses, m) as the function of the capacitance change. The reference capacitor C_r is set to 100 pF, the sensor is set to 120 pF and C_c is set to 120 pF. The output was expected to be zero, but because of tolerance in components, and quantization errors, the output signal is m = 20. Thou, to minimize the quantization error and increase the measurement range, C_r is increased to 220 pF and the output offset signal therefore becomes, as expected, 9 counts. Fig 5.14 shows two measurements performed on the full system. The first measurement is done with a difference of 20 pF between the sensor and reference, and the second with an increase in C(x) of 50 pF. In the first case, each quantization step (pink signal) has an amplitude of 172mV; as the capacitance is increased to 50 pF also the amplitude of the steps increases to 313 mV thus a larger number of impulses (purple signal) are found at the output. Table 5.5 summarizes all the results for the SCI circuit for a maximum capacitance change of 190 pF where an almost constant measurement error due to a non optimized value of C_r is reported. The input/output relation is almost linear, it is not however perfect because of the quantization error that is caused by the fact that m is given as an integer. From Eq. 4.6, for a 10pF change in capacitance, 64 clock cycles and a reference capacitance of 220pF, m is calculated to be 2.91, therefore not an integer. This means that the systems sensitivity is 2.91 per step of 10 pF with a high hold period of 64 clock periods and a quantization error is expected.

5.2.2 Charge-discharge circuit performances

The charge-discharge interface has been tested using a 120 pF capacitor as reference and a variable capacitance decade box ranging from 10 pF to 99 μF as sensor. The output voltage is measured compared to the difference in capacitance between sensor and reference. The value of the feedback resistor, R_f, is changed to measure the span and sensitivity of the system. Four different values of R_f are used and the results are shown in Fig. 5.15. Depending on the needed pressure span and resolution in the application, the feedback resistor can be adjusted. If the application needs a system which can measure a huge pressure span, then a low value

Figure 5.14: Measurement of the SCI. Pink denotes the input of comparator minus the negative input on the operational amplifier A_2. Purple denotes the output,Φ_c and red denotes the clock. In the first measurement the capacitance signal is 20pF while in the second it is 50 pF therefore the quantization step increases as well as the output.

Capacitance change (ΔC) pF	**Output** (m)	**Output/Cycle** ($m/2^n$)	**Capacitance Change/Reference** ($\Delta C/C_r$)	**Measurement Error** ($m/2^n$-$\Delta C/C_r$)
0	9	0.1406	0	0.1406
10	12	0.1875	0.0454	0.1420
20	15	0.2343	0.0909	0.1434
30	17	0.2656	0.1363	0.1292
40	22	0.3437	0.1818	0.1619
50	24	0.375	0.2273	0.1477
...	...	...	...	...
190	64	1	0.8636	0.1364

Table 5.5: SCI performances. Ideally the measurement error should be 0 but it would require a reference capacitance with sub pF precision which of course is not commercially available.

should be used. On the other hand, if the application needs a system with more precision in a smaller span, a higher value of R_f should be used. Moreover, all the tests performed show good linearity. Thermal tests have been done on the Mini-Mount setup. This was done on DTU Elektro in a thermic chamber from Gallenkamp at six different temperatures: 0 °C, 25 °C, 45 °C, 65 °C, 85 °C and 100 °C. T The reference capacitance is chosen to be a 120 pF with a 1% tolerance. R_f is chosen to be 50 kΩ, and C_f is selected to be 120 pF because of desired measurement span of 120 pF. The graph in Fig. 5.16 shows the output with temperature change. A temperature sensitivity of 0.013% of the full scale/°C has been measured. The output varies linearly with temperature change and the resolution is around 5 mV/pF and there is no change in the offset voltage due to temperature.

5.2.3 AC-bridge circuit performances

In order to measure the linearity of the system a capacitor of 120 pF (roughly the same value of the offset capacitance of the sensors which will be discuss here after) was used as reference and a capacitor decade box was used as the sensor.

The entire measurement setup (see figure 5.17) consists therefore of a nitrogen tank which is hooked up to a pressure controller in order to provide the pressure needed for the measurement, a PC which is connected to the pressure controller and a multimeter so that, for each pressure step, the output voltage of the system is recorded.

In order to characterize the performances of the two circuits fabricated, tests at four different temperatures, $0°C$, $25°C$, $50°C$ and $75°C$, have been carried out using the Gallenkamp environmental chamber. The curves obtained by varying the capacitance decade box from 120 pF to 240 pF in steps of 10 pF (smallest value possible), are presented in Fig. 5.18 for the transformer arm-ratio bridge and figure 5.19 for the electronic-arm ratio bridge. From these two figures it can be noticed that the linearity of the circuits is maintained even though the sensitivity is reduced noticeably when the temperature rises over ambient temperature. Furthermore, for temperatures between room temperature and $0°C$, the sensitivity increases as temperature rises for the transformer arm-ratio bridge while it is almost constant for the other circuit. With the aid of a commercial simulation software (B2spice), the theoretical sensitivity of the system has been evaluated, at room temperature, for the same capacitance range; table 5.6 shows the expected values given by the software and the actual value measured with the multimeter. After

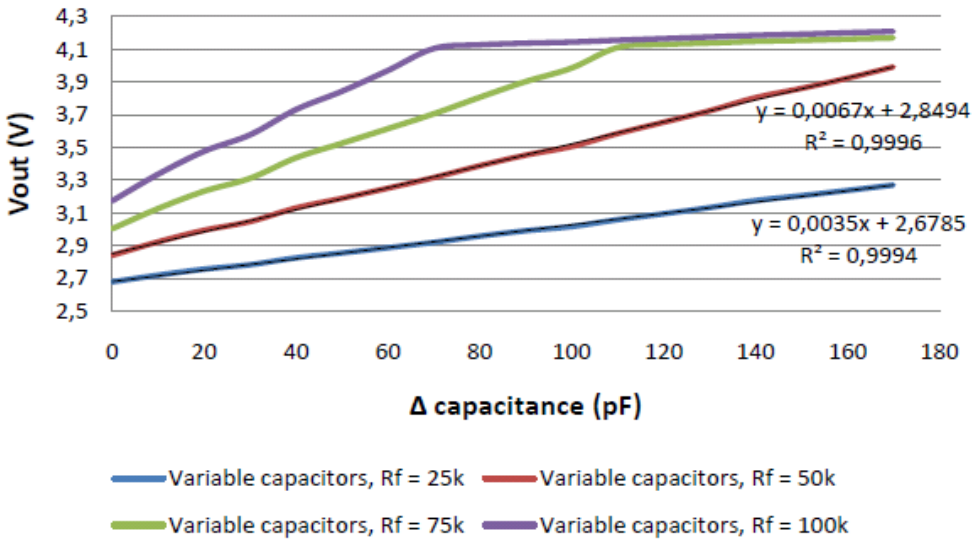

Figure 5.15: Test of the Charge Transfer System, using variable capacitor. Measurements done for four different values of Rf are shown.

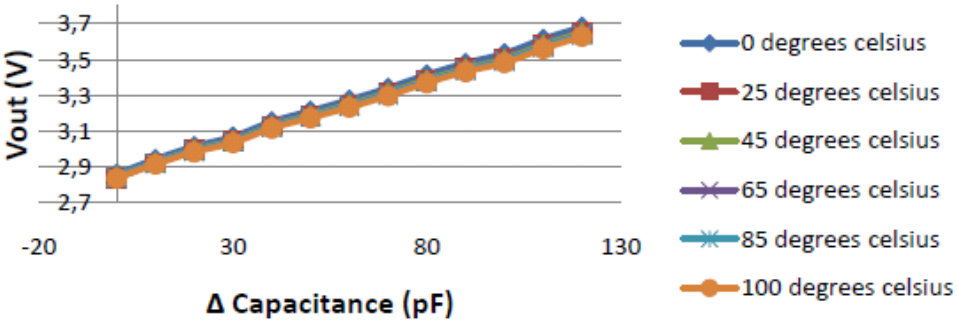

Figure 5.16: Thermic test of Charge Transfer System. The output voltage as a function of change in capacitive pressure is shown with varying temperature from 0 to 100 °C.

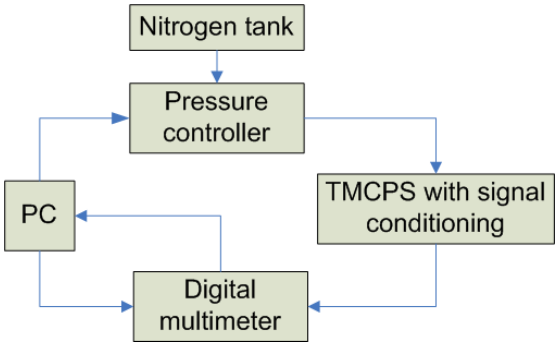

Figure 5.17: Block diagram of the measurement setup. This setup is used to obtain the capacitance-voltage curves.

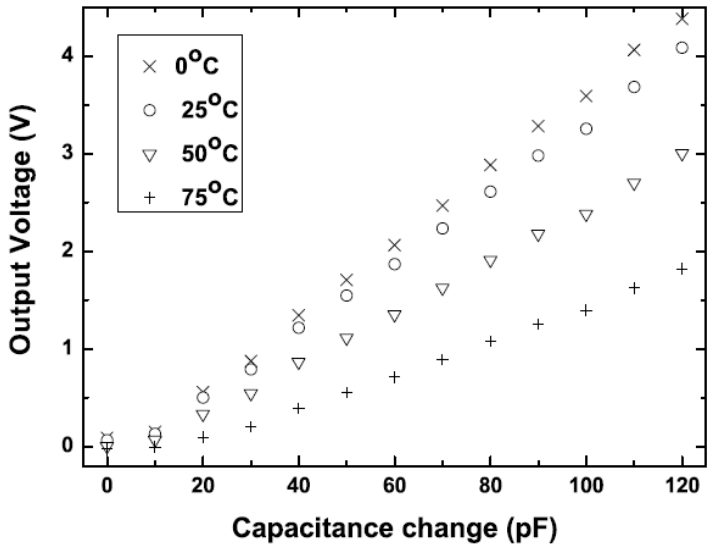

Figure 5.18: Voltage output of the transformer arm-ratio bridge. The dynamic range and therefore the sensitivity is reduced as temperature increases.

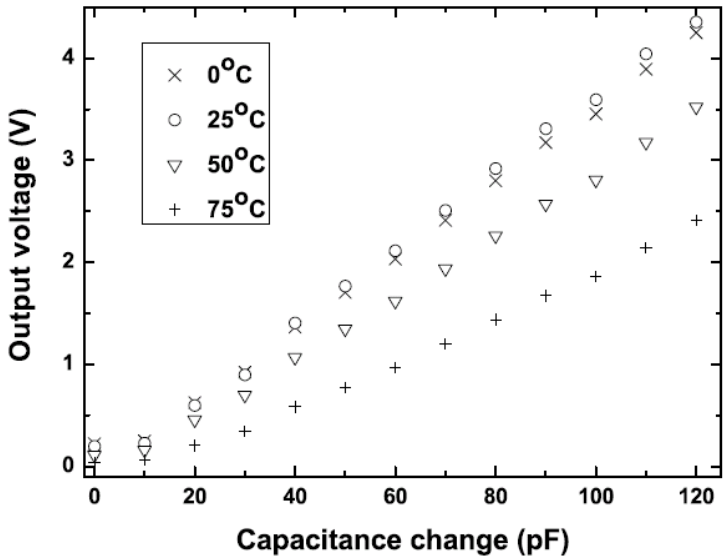

Figure 5.19: Voltage output of the electronic arm-ratio bridge. The dynamic range and therefore the sensitivity is maximum at room temperature.

	Sensitivity at 0°C (mV/pF)	Sensitivity at 25°C (mV/pF)	Sensitivity at 50°C (mV/pF)	Sensitivity at 75°C (mV/pF)
Transformer arm-ratio	39	36 35 (B2Spice)	27	17
Electronic arm-ratio	36	38 38 (B2Spice)	30	22

Table 5.6: Sensitivity at different temperatures of the two circuits developed. The value at room temperature can be compared to the theoretical value given by the B2Spice simulation

	Transformer arm-ratio	Electronic arm-ratio
Sensitivity (1 to 1.4 bar)	3.5 mV/mbar	3.0 mV/mbar
Linearity (1 to 1.4 bar)	7.4 % of full scale	6.5 % of full scale
Sensitivity (2 to 5 bar)	1.2 mV/mbar	1.0 mV/mbar
Linearity (2 to 5 bar)	1.6 % of full scale	1.5 % of full scale
Current consumption	15 mA	36 mA
Temperature coefficient	0.4 mV/mbar°C	0.3 mV/mbar°C

Table 5.7: Comparison of the two systems developed. The sensitivity and linearity in the two different working modes, the current consumption and the temperature coefficient have been evaluated

the temperature tests, a TMCPS have been attached to the transformer arm-ratio bridge circuit and the setup shown in Fig. 5.17 has been used to obtain the graph presented in Fig. 5.20. Here the pressure has been varied from 1 to 7 bar in steps of 100 mbar; it is clear that touch point is reached around 1.7 bar where the sensor output starts to be linear. Given the highly non-linear behavior of the sensor, two different sensitivities must be defined, one refers to the normal region (well below touch point) and the other refers to the touch mode region. To evaluate the performance in the normal mode region, the feedback capacitance in the current detector has been set to 100 pF. In order to measure the sensitivity and linearity in touch mode the feedback capacitance has been set to 350 pF while the reference capacitance has been raised from 140 pF (reference sensor) to 220 pF, which is above the touch point capacitance. Furthermore, the variable resistor in the AC-DC has been adjusted to use the full dynamic range (0 to 4.5 V) in all the measurements. In the two inlets of figure 5.20 the linear fit performed in the two regimes is shown, from 1 to 1.4 bars the system has a linearity of 3.5 % of the full scale while from 2 to 5 bars the linearity is 1.6 % of the full scale. Finally the same TMCPS and reference have been used to evaluate the performances of the electronic-arm ratio bridge. It is clear from figure 5.21 that, if the same components are used, the output of the electronic arm-ratio bridge is around 10 % lower than the output of the transformer arm-ratio bridge. Furthermore the sensitivity is reduced and the dynamic range is lower.

In the following section a final comparison of the all the circuits implemented is described and the conclusions regarding the interfacing solution are drawn.

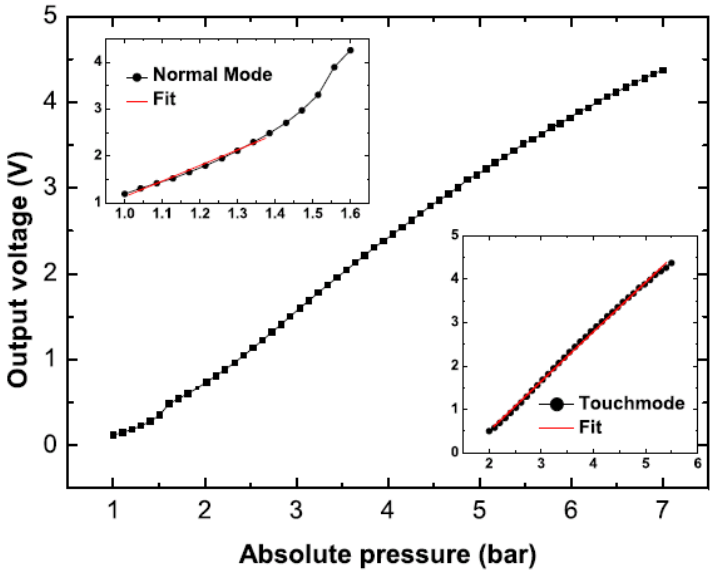

Figure 5.20: Output voltage of the system given by the transformer arm-ratio bridge. The top inlet show the normal mode region where only a part of it has a good linearity while in the touch mode region (bottom inlet) the system is linear for a large pressure range.

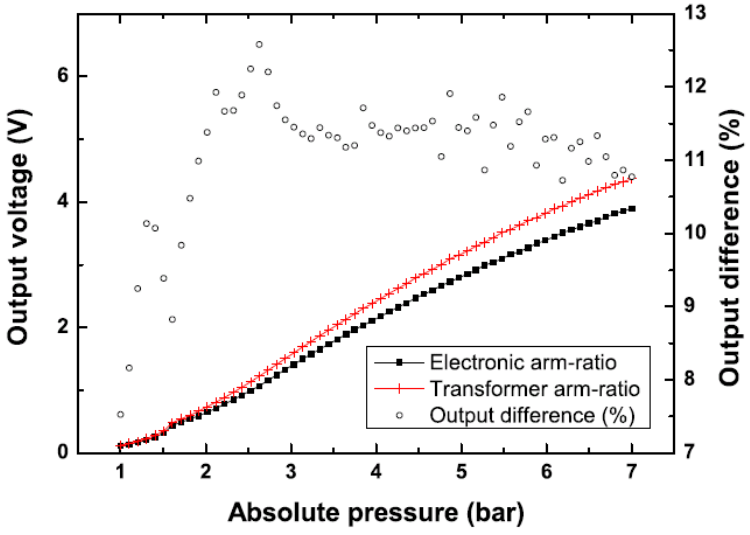

Figure 5.21: Comparison of the transformer arm-ratio bridge (red crosses) and the electronic arm-ratio bridge (black squares). The second system has a lower dynamic and therefore a lower sensitivity, its output is around 11 % lower than the transformer arm-ratio bridge when working in touch mode.

	Switch capacitor interface	**Charge-discharge circuit**	**Electronic arm-ratio bridge**	**Transformer arm-ratio bridge**
Power supply	Dual (+/-5V)	Single (7.5V)	Dual (+/-5V)	Dual (+/-5V)
Current consumption	65 mA	38 mA	36 mA	15 mA
Sensitivity	0.33 count/pF	10 mV/pF	38 mV/pF	36 mV/pF
Complexity	20 ICs	7 ICs	5 ICs	4 ICs, 1 transformer
Temperature coefficient	N.A.	0.013%FS/°C	1.2%FS/°C	0.8%FS/°C
Output	digital	analogue	analogue	analogue

Table 5.8: Comparison of all the circuits realized in this project. The bridge circuits can in principle be realized on single power supply with a reduced dynamic range. The maximum resolution of the switch capacitor interface is around 3 pF (one count) on a 190 pF range, while for the other circuits the sensitivity is measured over 120 pF range.

5.2.4 Interfacing circuits comparison

A big effort to analyze different possibilities of signal conditioning solutions for capacitive sensors has been done during this project. Four different solutions have been presented and discussed with abundance of details. Table 5.8 shows all the main results achieved with the chosen circuits.

The AC bridge solution has a limited number of ICs but also a large temperature dependence. Furthermore, the charge-discharge circuit has been implemented with a PIC12F609 microcontroller for the control signals generation. This design resulted in the same sensitivity, as expected, but achieved with only 4 ICs and a current consumption of 10 mA. Even though, in the opinion of the author, the charge-transfer circuit is the best possible option in many respect such as low complexity (and therefore costs), thermal stability and size, the AC-bridge is the circuit that was selected for the demonstrator being the one that was more thoroughly analyzed and tested. In the following section the full system is presented and this chapter is concluded.

5.3 Final design and conclusion

This dissertation is concluded presenting the biggest achievement of this Ph.D. project namely, the demonstrator of a TMCPS with signal conditioning electronics built on Grundfos OEM PCB and encapsulated in Grundfos case (see Fig. 5.22). The PBC layout has been done at Grundfos headquarter where around 20 boards have been produced and manually soldered. The PCBs had to be debugged and slightly modified after production because the chosen diodes did not behave as the one tested before, a missing ground path was found and some components were badly soldered. A first set of measurements on one the demonstrator are shown in Fig. 5.23 where the system was tested up to 10 bar gage. Even though the gain has not been optimized sensitivities of 140 mV/bar and 150 mV/bar and are achieved in normal and touch mode respectively. Adjusting the gain will almost double these values which already are comparable to Motorola tire pressure sensor (with a sensitivity of 120 mV/bar) that have only 2 bar dynamic

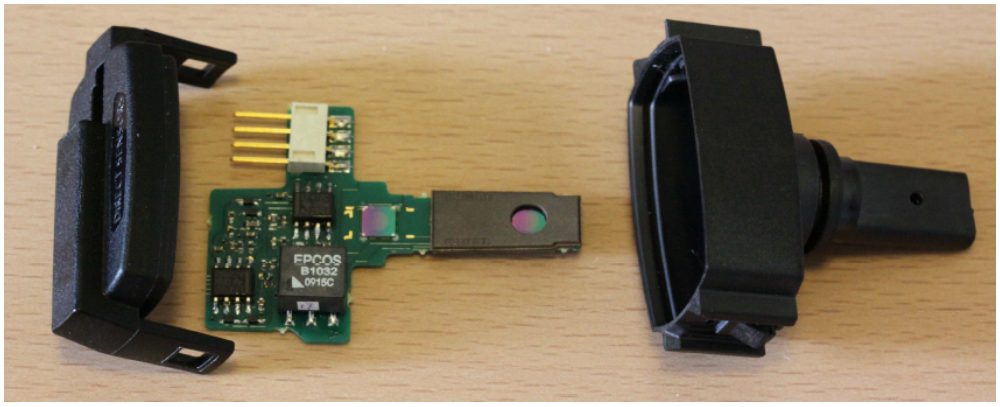

Figure 5.22: TMCPS with transformer-arm-ratio bridge. On the left end of the PCB it is possible to notice the dies which are the sensor and the reference elements, on the right,the larger component of the circuit namely the EPCOS transformer.

range.

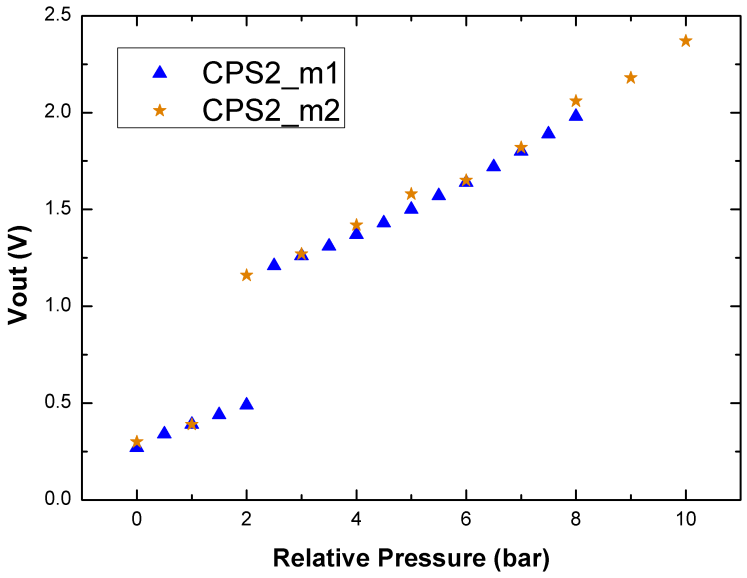

Figure 5.23: Capacitance-voltage curves measured for the prototype in Fig. 5.22. Two measurements are reported, one covers a smaller pressure range but with a finer step, the other spans from 0 to 10 bar gage in steps of 1 bar.

This result suggest the possibility of producing highly competitive pressure sensors of different pressure ranges and sensitivities and with low cost conditioning circuit. In the next chapter all the achievement met in this work are summarized and the project outlooks are stated.

Chapter 6

Conclusion

The purpose of this project has been to design and fabricate capacitive pressure sensors with signal conditioning electronics. The devices fabricated are intended to be the first step done in order to include in Grundfos portfolio a new product with higher pressure range and sensitivity as well as lower power consumption and still designed for harsh environment. The conclusion presents the main results achieved during this project and the outlooks that, in the opinion of the author, can bring the demonstrator produced a step closer to commercialization. The author has strongly contributed to all the publications cited in this chapter.

- **Analytical model for TMCPS**. An analytical model for TMCPS has been described. It has been shown that, in the linear elastic regime, there is a closed form solution to the integral defining the capacitance of a device driven into touch mode. Combining this with the solution found for a device working in normal mode a fitting function for the entire C-P curve has been found. The fitting function has been tested using a device working in the linear elastic regime and an excellent match between fitted and measured parameters has been shown. In "*Analysis of small deflection touch mode behavior in capacitive pressure sensors*" a maximum deviation of the model from the data points of only 3.7% was reported. With the derived analytical model a TMCPS can be designed to have the desired capacitance and sensitivity by fixing a set of fabrication parameters.

- **Model validation** The analytical model has been validated through FEA of the mechanical problem. The FEM hes also been used to compute the capacitance of the pressure sensor in both normal mode and touch mode and good agreement, within 14% has been reported in "*Validation of an analytical model for contact mode plate deflection of touch mode capacitive pressure sensors*". The deviation is largest at the transition region, for which the mechanics is accurately captured by the FEM. In conclusion the analytical model for a touch mode capacitive pressure sensor has been shown to agree well with FEM. This provides a clear picture of the physics underlying the pressure sensor operation and provides equations for design in terms of key parameters such as sensitivity, touch point pressure etc.

- **Pressure sensor fabrication and characterization** In "*Highly sensitive micromachined capacitive pressure sensor with reduced hysteresis and low parasitic capacitance*" the design of the capacitive pressure sensor developed in this project is presented. Due to the membrane structure this device offers a high capacitance signal and a low parasitic capacitance which is important in order to achieve a high sensitivity. At a pressure above

2 bar the sensor operates in touch mode and has an average sensitivity from 2 to 6 bar of 76 pF/bar. The hysteresis observed for these types of sensors is nearly eliminated applying a DC bias of 9 volt or confined to less than 1% in the entire pressure range with the nanopillar structure described in "*Intrinsic Low Hysteresis Touch Mode Capacitive Pressure Sensor*". Furthermore, the exposed surface of the sensor is completely flat such that corrosion resistant thin films may be deposited on it. Finally the technology transfer problem between Danchip and Grundfos has been addressed.

- **Interfacing electronics for TMCPS** Three different solutions for signal conditioning of capacitive sensors have been studied. The switch capacitor interface has a sensitivity of 0.33 count/pF, digital output and offset capacitance compensation. The charge-discharge circuit has an excellent thermal coefficient (less than 0.02% of the full scale/°C), etremely low circuit complexity (only 4 ICs) and a sensitivity of 10 mV/pF. Finally the AC-Bridge solution has a very high sensitivity, more than 30 mV/pF, a low circuit complexity (only 4 ICs and one transformer) and can be relized using a single power supply. All the solution proposed do not need any calibration/adjustment and have a good linearity (less than 1% of the full scale).

- **Full system**. A demonstrator of a TMCPS with signal conditioning electronics and packaging solution has been developed. Sensor and electronics are placed onto a Grundfos OEM PCB which is sealed into Grundfos case. The sensing element is clamped with an O-ring to guarantee good sealing. Test performed on the full system showed a sensitivity of around 150 mV/bar on a 10 bar pressure range, a current consumption of 10 mA and low production costs (the most expensive component, the transformer, costs around 3 kr).

Even though a great deal of research on micromachined capacitive sensors has been done in DTU Nanotech since 2006, there are still some aspects that should be investigated. On the other side, for the development of a commercial product many issues have not been jet addressed. Therefore a list of outlooks for this project results necessary.

- **Deeper study of the coating solution**. The most important parameter that has been taken into account only from a theoretical point of view in this project is the deposition of a coating layer onto the TMCPS. With the aid of the electro-mechanical models developed a prediction of the behavior of TMCPS with coating can be done but it must still be verified experimentally.

- **Mixed signal electronics**. The fabrication of a signal conditioning circuit that with the aid of a microcontroller performs the linearization of the C-P curve as well as temperature compensation is highly desirable.

- **Integrated electrics**. Depending on the production volume expected a TMCPS with integrated signal conditioning electronics should be considered. Capacitive sensing gain a lot from this kind of solution which reduces parasitics therefore improving the signal to noise ratio.

- **Different fabrication solutions**. Fusion bonding is not one of the most developed cleanroom process and may result in extra costs and lower yield. Trying other techniques, such as anodic bonding or the use of a sacrificial layer, may be woth investigation.

- **Business case and market research**. At this point an evaluation of the cost, that the technology transfer and production of a new product based on TMCPS will involve, must be done. These have to be compared with an estimation of the profit achievable with the new pressure sensor solution.

Bibliography

[1] CalibrationDynamics, *Dead-weight gage*. www.sensorland.com/HowPage079.html.

[2] Efunda, *Manometer Pressure*. http://www.efunda.com/formulae/fluids/manometer.cfm.

[3] EngineeringOperations, *Inclined Manometer*. http://engineeringoperations.blogspot.com.

[4] A. V. Beckerath, A. Eberlein, H. Julien, P. Kersten, and J. Kreutzer, *WIKA Handbook: Pressure & Temperature Measurement*. WIKA Instrument Corporation, u.s. ed., 1998.

[5] H. E. Darling and D. H. Newhall, "A high-pressure wire gage using gold-chrome wire," *Transactions of the ASME*, vol. 75, no. 3, pp. 311–314, 1953.

[6] K. J. Lesker, *Hot Filament Gauges*. http://www.lesker.com.

[7] E. Mounier, *MEMS Market forecast 2007-2012*. Yole Development.

[8] P. Venkatesh, *MEMS Pressure Sensors in the Automotive Industry*. Forst and Sullivan.

[9] CiS, *Piezoresistive pressure sensor catalog*. CiS Forschungsinstitut für Mikrosensorik und Photovoltaik GmbH.

[10] Motorola-Freescale, *MPXY8000 Series Tire Pressure Monitoring Sensors (TMPS)*. www.freescale.com/files/abstract/misc/PKMPXY8000TPM.html.

[11] M. Yamada, T. Takashi, S. I. Notoyama, and K. Watanabe, "A switched-capacitor interface for capacitive pressure sensors," *IEEE Transactions on Instrumentation and Measurement*, vol. 41, pp. 81–86, 1992.

[12] E. O. Doebelin, *Measurement Systems Application and Design*. McGraw-Hill, 5th ed., 2003.

[13] S. Timoshenko and S. Woinowsky-Krieger, *Theory of Plates and Shells*. McGraw-Hill, 2 ed., 1959.

[14] R. Gao and L. Zhang, "Micromachined microsensors for manufacturing," *Ieee Instrumentation and Measurement Magazine*, vol. 23, pp. 142–149, 2008.

[15] W. Eaton and J. Smith, "Micromachined pressure sensors: Review and recent developments.," *Smart Materials and Structures*, vol. 6, pp. 530–539, 1997.

[16] K. Petersen and F. Pourahmadi, "Resonant beam pressure sensor fabricated with silicon fusion bonding," *Solid-State Sensor and Actuator*, pp. 664–667, 1991.

[17] X. Wang, B. Li, O. L. Russo, H. T. Roman, K. K. Chin, and K. R. Farmer, "Diaphragm design guidelines and an optical pressure sensor based on mems technique," *Microelectronics Journal*, vol. 37, pp. 50–56, 2006.

[18] C. Yeh and K. Najafi, "Bulk silicon tunneling based pressure sensors," *Solid-State Sensor and Actuator Workshop*, 1994.

[19] D. S. Greywall, "Micromechanical light modulators, pressure gauges, and thermometers attached on optical fibers.," *J. Micromech. Microeng.*, vol. 7, pp. 343–352, 1997.

[20] R. Maron, "High sensitivity fiber optic pressure sensor for use in harsh environments," *U.S. Patent 6,016,702*, 2000.

[21] J. B. Lasky, S. R. Stiffler, F. R. White, and J. R. Abernathy, "Silicon-on-insulator (soi) by bonding and etch-back," *IEEE Int. Electron Device Meeting*, vol. 85, pp. 684–687, 1985.

[22] W. Heerens, "Application of capacitance techniques in sensor design," *Journal of Physics E: Scientific Instruments*, vol. 19, no. 11, pp. 897–906, 1986.

[23] R. Jones and J. Richards, "Design and some applications of sensitive capacitance micrometers," *Journal of Physics E: Scientific Instruments*, vol. 6, pp. 589–600, 1973.

[24] A. Hugill, "Displacement transducers based on reactive sensors in transformer ratio bridge circuits," *Journal of Physics E: Scientific Instruments*, vol. 15, pp. 597–606, 1982.

[25] S. Huang, A. Stott, R. Green, and M. Beck, "Electronic transducers for industrial measurement of low value capacitance," *Journal of Physics E: Scientific Instruments*, vol. 21, pp. 242–250, 1988.

[26] J. Kung, H. Lee, and R. Howe, "A digital readout technique for capacitive sensor application," *Ieee Journal of Solid-State Circuits*, vol. 23, pp. 972–977, 1988.

[27] A. Cichocki and R. Unbehauen, "Switched-capacitor tansducers with digital or duty-cycle output based on pulase-width modulation technique," *International Journal of Electronics*, vol. 71, pp. 265–278, 1991.

[28] W. Frobenius, A. Sanderson, and H. Nathanson, "Microminiature solid-state capacitive blood-pressure transducer with improved sensitivity," *Ieee Transactions on Biomedical Engineering*, vol. BM20, pp. 312–314, 1973.

[29] W. H. Ko and Q. Wang, "Touch mode capacitive pressure sensor," *Sensors and Actuators*, vol. 75, pp. 242–251, 1999.

[30] B. Puers, E. Peters, A. V. den Bossche, and W. Sansen, "A Capacitive Pressure Sensor with Low Impedance Output and Active Suppresion of Parasitic Effects," *Sensors and Actuators*, vol. 21, pp. 108–114, 1990.

[31] L. K. Baxter, *Capacitive Sensors: Design and Applications*. IEEE Press, 1 ed., 1997.

[32] J. Isaac, R. M. D. L. Rue, and K. K. Wong, "An optical pressure sensor in iii-v semiconductor material.," *Institute of Physics Short Meeting: Proceedings of Fiber Optic Sensors*, pp. 105–108, 1987.

[33] N. A. Hall, M. Okandan, R. Littrell, B. Bicen, and F. Degertekin, "Micromachined optical microphone structures with low thermal-mechanical noise levels," *Journal of the acoustical society of america*, vol. 122, pp. 2031–2037, 2007.

[34] M. .Li, M. Wang, and H. Li, "Optical mems pressure sensor based on fabry-perot interferometry," *Optics Express*.

[35] G. N. D. Brabander, G. Beheim, and J. T. Boyd, "Integrated optical micromachined pressure sensor with spectrally encoded output and temperature compensation," *Applied Optics*, vol. 37, pp. 3264–3266, 1998.

[36] H. Porte, V. Gorel, S. Kiryenko, J. Goedgebuer, W. Daniau, and P. Blind, "Imbalanced mach-zehnder interferometer integrated in micromachined siliconsubstrate for pressure sensor," *Journal of lightwave technology*, vol. 17, pp. 229–233, 1999.

[37] C. R. Dennison and P. M. Wild, "Enhanced sensitivity of an in-fibre bragg grating pressure sensor achieved through fibre diameter reduction," *Measurement science and technology*, vol. 19, pp. 3264–3266, 2008.

[38] K. Reck, N. Almind, M. D. Mar, J. Hübner, O. Hansen, and E. Thomsen, "Design and modeling of an all-optical frequency modulated mems strain sensor using nanoscale bragg gratings," *IEEE Sensors 2010. Proceedings*, pp. 873–877, 2010.

[39] C. C. Collins, "Miniature passive pressure transensor for implanting in eye," *IEEE transactions on biomedical engineering*, vol. BM14, pp. 74–83, 1967.

[40] M. A.Fonseca, J. M. English, M. von Arx, and M. Allen, "Wireless micromachined ceramic pressure sensor for high-temperature applications," *Journal of microelectromechanical systems*, vol. 11, pp. 337–343, 2002.

[41] P. Wouters, R. Puers, R. Geers, and V. Goedseels, "Implantable biotelemetry devices for animal monitoring and identification," *Proceedings of the IEEE-EMBS*, vol. 14, pp. 2665–2666, 1992.

[42] K. Najafi and K. Wise, "An implatable multielectrode array with on-chip signal-processing.," *IEEE journal of solid-state circuits*, vol. 21, pp. 1035–1044, 1986.

[43] W. E. Bulst, G. Fischerauer, and L. Reindl, "State of the art in wireless sensing with surface acoustic waves," *IEEE transactions on industrial electronics*, vol. 48, pp. 265–271, 2001.

[44] E. C. Park, J. B. Yoon, and E. Yoon, "Hermetically sealed inductor-capacitor (lc) resonator for remote pressure monitoring," *Japanese journal of applied physics*, vol. 37, pp. 7124–7128, 1998.

[45] O. Akar, T. Akin, and K. Najafi, "A wireless batch sealed absolute capacitive pressure sensor," *Sensors and actuators A-physcial*, vol. 95, pp. 29–38, 2001.

[46] S. Kim, H. Kim, and J. Park, "A telemetry silicon pressure sensor of lc resonance type," *Design, test, integrations and packaging of MEMS/MOEMS 2001*, vol. 4408, pp. 452–462, 2001.

[47] C. Parsa, M. Daneshmand, and K. M. R. H. G. Lima, B; Balsara, "Utility of remote wireless pressure sensing for endovascular leak detection after endovascular thoracic aneurysm repair," *Annals of thoracic surgery*, vol. 89, pp. 446–452, 2010.

[48] K. D. Wise, "Integrated sensors, mems, and microsystems: Reflections on a fantastic voyage," *Sensors and Actuators A: Physical*, vol. 136, no. 1, pp. 39–50, 2007. 25th Anniversary of Sensors and Actuators A: Physical.

[49] R. Szilard, *Theories and Applications of Plate Analysis*. Wiley, 1st ed., 2004.

[50] G. Meng and W. H. Ko, "Modeling of circular diaphragm and spreadsheet solution programming for touch mode capacitive sensors," *Sensors and Actuators*, vol. 75, pp. 45–52, 1999.

[51] M. Daigle, J. Corcos, and K. Wu, "An analytical solution to circular touch mode capacitor," *IEEE Sensors Journal*, vol. 7, pp. 502–505, 2007.

[52] D. P. R. P. P. P. F. Pennec, H. Achkar and F. Courtarde, "Verification of contact modeling with comsol multiphysics software," *6th EuroSIM Congress on Modelling and Simulations*, 2009.

[53] X. Ding, L. Tong, W. He, J. Hsu, and W. Ko, "Touch mode silicon capacitive pressure sensors," in *Winter Annual Meeting of the American Society of Mechanical Engineers, Conference Dallas, TX*, pp. 111–117, 1990.

[54] H. Dudaicevs, M. Kandler, Y. Manoli, W. Mokwa, and E. Spiegel, "Surface micromachined pressure sensors with integrated cmos read-out electronics," *Sensors and Actuators A: Physical*, vol. 43, pp. 157–163, 1994.

[55] M. Madou, *Fundementals of Microfabrication*. CRC Press, 1 ed., 1997.

[56] T. Pedersen, *Corrosion resistant capacitive pressure sensor*. PhD thesis, M.Sc. Thesis, Technical University of Denmark, 2008.

[57] C. Christensen, *Advanced packaging technologies for differential pressure sensors exposed to agressive media*. PhD thesis, Technical University of Denmark - Mikroelektronik Centret, 1998.

[58] T. Pedersen, O. Hansen, and E. Thomsen, "Reduction of hysteresis in capacitive pressure sensors," in *Proceedings of EUROSENSOR XXII*, 2008.

[59] W. M. V. Spengen and T. H. Oosterkamp, "A sensitive electronic capacitance measurement system to measure the comb drive motion of surface micromachined mems devices," *JOURNAL OF MICROMECHANICS AND MICROENGINEERING*, vol. 17, pp. 828–834, 2007.

[60] A. Ashrafi and H. Golnabi, "A high precision method for measuring very small capacitance changes," *Review of Scientific Instruments*, vol. 70, pp. 3483–3487, 1999.

[61] A. P. SONGMING Huang, ROBERT G. Green and M. S. BECK, "A high frequency stray-immune capacitance transducer based on the charge transfer principle," *IEEE TRANSACTIONS ON INSTRUMENTATION AND MEASUREMENT*, vol. 37, pp. 368–373, 1988.

[62] B. Hague and T. Foord, *Alternating Current Bridge Methods*. Pitmann press, 1971.

[63] M. Kanno and T. Horikawa, "Stray-effect-free direct impedance-to-frequency converter," *IEEE TRANSACTIONS ON INSTRUMENTATION AND MEASUREMENT*, vol. 27, pp. 405–408, 1978.

[64] S. Franco, *Design with Operational Amplifiers and Analog Integrated Circuits*. New York: The McGraw-Hill Companies, 3rd ed., 2002.

[65] W. H. Ko and Q. Wang, "Modeling of touch mode capacitive sensors and diaphragms," *Sensors and Actuators*, vol. 75, pp. 230–241, 1999.

Appendix A

List of Publications

1. Fragiacomo, G.; Ansbæk, T. and Thomsen, E. V. *Validation of an analytical model for contact mode plate deflection of touch mode capacitive pressure sensors*, accepted for the proceedings of: Fifth International Conference on Sensing Technology (ICST2011), Nov. 2011.

2. Ambrosini, S.; Wagner, J. B.; Booth, T.; Savenko, A.; Fragiacomo, G. ; Bøggild, P.; Rubini, S. *In situ transmission electron microscopy analyses of thermally annealed self catalyzed GaAs nanowires grown by molecular beam epitaxy* Proceedings of: 18. International Symposium. Nanostructures: Physics and Technology, Feb. 2011, Ekaterinburg, Russia.

3. Fragiacomo, G.; Pedersen, T.; Hansen, O. and Thomsen, E. V. *Intrinsic Low Hysteresis Touch Mode Capacitive Pressure Sensor*, Proceedings of: IEEESensors Nov. 2010, pages: 2279-2282.

4. Fragiacomo, G.; Reck, K.; Lorenzen, L. V. and Thomsen, E. V. *Novel Designs for Application Specific MEMS Pressure Sensors* Sensors, vol: 10, issue: 11, pages: 9541-9563, 2010, MDPI.

5. Fragiacomo, G.; Ansbæk, T.; Pedersen, T.; Hansen, O. and Thomsen, E. V.*Analysis of small deflection touch mode behavior in capacitive pressure sensors*, Sensors and Actuators A: Physical, vol: 161, issue: 1-2, pages: 114-119, 2010, Elsevier S.A.

6. Fragiacomo, G.; Eriksen, G. F.; Christensen, C. and Thomsen, E. V. *Touch mode micromachined capacitive pressure sensor with signal conditioning electronics*, proceedings of: Micronano Systems Workshop 2010, May 2010, Stockholm, Sweden.

7. Pedersen, T. ; Fragiacomo, G.; Hansen, O. and Thomsen, E. V. *Highly sensitive micromachined capacitive pressure sensor with reduced hysteresis and low parasitic capacitance*, Sensors and Actuators A: Physical, vol: 154, issue: 1, pages: 35-41, 2009, Elsevier S.A.

8. Fragiacomo, G.; Bing, P. G.; Bjørnson, T; Thomsen, E. V. and Kjærgaard, C. *Signal conditioning circuit for MEMS capacitive pressure sensors*, in preparation.

Appendix B

Capacitive pressure sensor with gold coating process flow

This appendix describes the process flow developed in order to obtain touch mode capacitive pressure sensors (TMCPS) with gold coating. In the following tables all the different steps are numbered together with the process heading, the machine used and its parameters, the step time and some useful notes. To help the understanding, the process is also depicted in Fig. B.1 where cross sections of the chips after the main steps are illustrated. The TMCPS are fabricated with two wafers, a double side polished (DSP) wafer and a silicon on insulator (SOI) wafer bonded together at low vacuum so that absolute pressure sensors are fabricated. Firstly both wafers are doped (Fig. B.1a) to form the plates of the capacitor, then a series of steps such as wet oxide growth (Fig. B.1b), oxide etch (Fig. B.1c) and dry oxide growth (Fig. B.1d) are performed on the DSP wafer to create the cavities and the insulation layer necessary for the TMCPS. Two structure, namely the insulation groove and the bottom contact hole, are etched in the device layer of the SOI in the step shown in (Fig. B.1e). The two wafers are then ready for bonding (Fig. B.1f), SOI handle removal (Fig. B.1g), contact opening through the SOI box (Fig. B.1h) and finally the metalization (Fig. B.1i).

	Wafer	Process heading	Parameters	Time	Notes
1.0	DSP+SOI	Phosphorus predeposition	Phosphorus predepositon furnace. Recipe: POCL1000	60 min	This gives a junction depth of 1.5-2 μm.
1.1	DSP+SOI	Remove oxide from pre deposition	BHF	1 min	
2.1	DSP	Around 400 nm oxide growth	Phosphorus drive in furnace. Recipe: wet1100	25 min	Touch mode at 24 bar for 35μm radius, 5,9 bar for 50μm radius and 1,2 bar for 75μm radius. Test wafer 2 udtaget her. Take out 1 test wafer for the corrugation oxide before this step
3.0	DSP	Lithography. Positive process. First print	Mask M1 - Oxide etch of bottom wafer		
3.1	DSP	Apply HMDS	HMDS oven Program 4	35 min 10 min	
3.2	DSP	Spin on 1,5μm resist	Track 1 Recipe: PR1-5		
3.3	DSP	Alignment and exposure	6inch Aligner 30μm	3 s	
3.4	DSP	Development	AZ351B developer	65 s	
3.5	DSP	Hard bake	120°C oven	25 min	
3.6	DSP	Oxide etch	RIE Recipe: tpesio1	20 min	Test etchrate on dummy wafer. This is only done with 8 wafers + one test which got too much time.
3.6B	DSP	Oxide etch	BHF	10 min	This is done with the rest of the wafers.
3.7	DSP	Acetone strip of resist	Rough strip Fine strip	3 min 5 min	

	Wafer	Process heading	Parameters	Time	Notes
4.0	DSP	RCA clean			
4.1	DSP	Thin oxide layer	Phosphorus drive in furnace. Recipe: dry1000	15 min	
5.0	SOI	Lithography. Positive process. First print	Mask M2A - SOI groove etch v2		This is the modify M2 mask (it contains the old mask M4!!!)
5.1	SOI	Apply HMDS	HMDS oven Program 4	35 min 10 min	
5.2	SOI	Spin on $1,5\mu m$ resist	Track 1 Recipe: PR1-5		
5.3	SOI	Alignment and exposure	6inch Aligner	3 s	No aligning since it is the first print.
5.4	SOI	Development	AZ351B developer	60 s	
5.4b	SOI	Etch of oxide in groove.	RIE, Recipe: tpesio1	7 min	
5.5	SOI	Insulation groove etch	ASE Recipe: shallolr	57 s (5 cycles)	Test etchrate. Not done but checked that we went down to the box oxide.
5.6	SOI	Acetone strip of resist	Rough strip Fine strip	3 min 3 min	

	Wafer	Process heading	Parameters	Time	Notes
6.0		Clean IMEC tub			
6.1		Clean 7-up tub			
6.2		Prepare IMEC	4000 ml water 400 ml 5% HF 40 ml isopropanol		
6.3		Prepare Piranha	2500 ml H_2SO_4 625 ml H_2=$_2$		
6.4	DP and SOI	1st piranha dip		5 min	
6.5	DP and SOI	Rins in water		2 min	
6.6	DSP and SOI	IMEC dip		100 sek	
6.7	DSP and SOI	Rins in water		2 min	
6.8	DSP and SOI	2nd piranha dip		20 min	
6.9	DSP and SOI	Rins in water		5 min	
6.10	DSP and SOI	Spin dryer		5 min	Leave wafers in a new/clean wafer box
7.0	DSP and SOI	Alignment	EVG 610 Aligner Anodic bonding Transparent alignment Flags before WEC		SOI is top substrate
7.1	DSP and SOI	Fusion bonding	EVG 520HE bonder 1500 N 50°C 1^{-2} mbar	5 min	
7.2	Bonded	Annealing of bonded wafers	Anneal bond furnace Recipe: ANN1100	70 min	Wafer bottom er handle side now
8.0	Bonded	Etch of handle wafer	Pegasus Recipe: etchaway	27 min 30 sec	Handle thickness 300μm
8.1	Bonded	Remove the remaining Si layer	KOH tub in clean room 3	11 min	

	Wafer	Process heading	Parameters	Time	Notes
9.0	Bonded	Lithography. Positive process.	Mask M5 - etch back of the aluminum.		It must be inverted!
9.1	Bonded	Apply HMDS	HMDS oven Program 4	35 min 10 min	
9.2	Bonded	Spin $1,5\mu m$ resist	Track 1 Recipe: PR1-5		
9.3	Bonded	Alignment and exposure	Hard contact Light integration: On. Alignment gap: $30\mu m$	3.6 s	KS Aligner. Pay attention on how the alignments marks look like: 3 crosses!
9.4	Bonded	Bake	120 °C	120 s	
9.5	Bonded	Fload Exposure	No alignment required	30 s	KS Aligner
9.6	Bonded	Development	AZ351B developer	70 s	
9.7	Bonded	Remove oxide	BHF	5 min	$1\mu m$ box oxide + ca. 50nm of insulation oxide.Conductivity must be measured.
9.6	Bonded	Acetone strip of resist	Rough strip Fine strip	1 min 4 min	**NO ULTRASOUNDS!!!** Maybe plasma asher is needed.
10.0	Bonded	Clear contacts	BHF	30s	
10.1	Bonded	Adesion layer and gold deposition	Wordentec	N.A.	Deposition of 5nm of Ti and 100 nm Au
10.2	Bonded	Lithography. Positive process	Mask M5 - Gold etch		The mask must be cleaned before utilizing it.
10.3	Bonded	Apply HMDS	HMDS oven Program 4	35 min 10 min	
10.4	Bonded	Spin on $6.2\mu m$ resist	SSE spinner.		
10.5	Bonded	Alignment and exposure	6” Aligner	20 s	Exposure time must be cheked if KS aligner is used.
10.6	Bonded	Development	AZ351B developer	4 min	
10.7	Bonded	Gold etch	20°C Iodine based gold etch	2.5 min	Stop etching by visual etchstop
10.8	Bonded	Acetone strip		1 min	
10.7B	Bonded	Plasma Asher	O2: 300ml/min N2: 30ml/min Power: 1000W	30 min	Maybe needed.

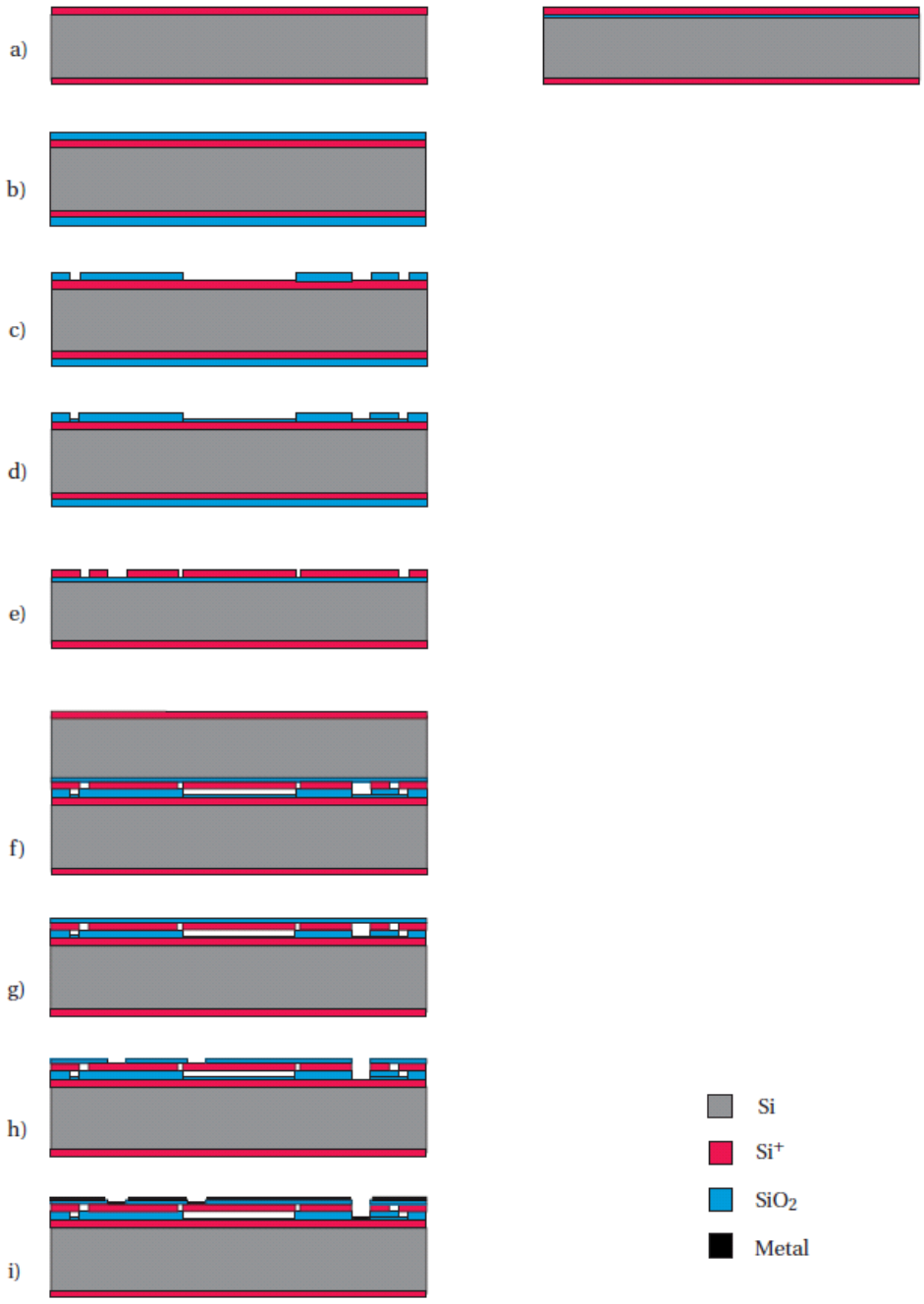

Figure B.1: Process sequence for CPS with gold coating and support structure etched with RIE.